JOINT INSTITUTE FOR NUCLEAR RESEARCH

Vera Shmakova

Study of the $pn \to \{pp\}_s\pi^-$ process near the threshold with formation of $^1S_0$ proton pairs in polarized experiments at ANKE-COSY

Ph.D. Thesis

Research supervisor:
Dr. S. Dymov
Scientific adviser:
Dr. Yu. Uzikov

Dubna - 2017

Abstract

Modern theory of strong interactions between nucleons is constructed within the framework of Chiral Perturbation Theory. In this case, chiral symmetry dictates the structure of the interaction operators, and its intensity is determined by the low-energy parameters of the theory, which must be extracted from experimental data. One of the key parameters of this theory is the contact $(NN)^2\pi$ term, which is included into the pion production $NN \to NN\pi$ near the threshold, hydrogen combustion $pp \to de^+\nu_e$, μ^--meson capture by deuteron $\mu^- d \to nn\nu_\mu$, and others. Among other processes of single-pion production, the reaction $pn \to \{pp\}_s\pi^-$ is the most preferable for determination of the contact interaction. Consequently, the main task of the thesis was to obtain new polarization data on this process.

In this regard, a program was proposed at the ANKE facility located on the COSY synchrotron (Jülich, Germany), including the measurement of the differential cross section and the vector analyzing power, as well as the spin-correlation coefficient $A_{x,x}$ for the process $np \to \{pp\}_s\pi^-$ at the energy of 353 MeV. The results of these experiments, as well as the joint partial-wave analysis of $pp \to \{pp\}_s\pi^0$ and $pn \to \{pp\}_s\pi^-$ data, make the basis of the thesis.

Contents

Chapter 1

Basic concepts of chiral perturbation theory of strong interactions

The modern elementary particles theory, commonly called the Standard Model of fundamental forces, is based on the principle of local gauge invariance under $SU_c(3) \times SU_L(2) \times U_Y(1)$ transformations, where the indices c, L and Y are color, left chirality and weak hypercharge, respectively. The Standard Model combines the theory of electroweak interactions, which describes the interactions between quarks and leptons through the exchange of photons and gauge bosons, and the quantum chromodynamics (QCD), which describes the strong interactions of quarks and gluons through the exchange of gluons. The predictions of the Standard Model for visible matter are reliably confirmed by experiment, except for a few cases, which are currently being analyzed.

While electroweak interactions can be described with this theory in a broad interval of energies, direct application of QCD as a theory of interaction between quarks and gluons is limited to high energies and high transferred momenta Q. QCD is based on the color gauge group $SU_c(3)$ and, therefore, is a nonlinear (non-Abelian) gauge field theory. The non-Abelian nature of the theory results in the asymptotic freedom of QCD, i. e., the coupling constant of strong interactions $\alpha_s(Q^2)$ decreases logarithmically as the square of the transferred momentum increases $Q^2 \to \infty$, $\alpha_s(Q^2) \sim /lnQ^2$, or, equivalently, decreases at small distances $r \sim 1/Q$ between interacting color ob-

jects, $\alpha_s(r) \sim 1/lnr$. However, this same property of the theory leads to an increase of the running coupling constant $\alpha_s(Q^2)$ at small transferred momentum, i. e., at large distances, which leads to quark confinement, and thus the formation of colorless objects, hadrons. In the perturbation theory framework, such an increase is unbounded. Consequently, the construction of the theory of strong interactions as a perturbation theory with expansion with respect to the coupling constant $\alpha_s(Q^2)$ is possible only at high energies. In the low-energy regions, QCD, as the theory of quarks and gluons, is applicable when using nonperturbative methods, such as lattice calculations. However, the applicability of these methods is rather limited by computer processing power. Therefore, instead of using QCD for calculations related to NN interactions, various phenomenological potentials based on meson exchange have long been used in practice [1–5]. At the same time, there is no connection between these phenomenological theories and QCD.

1.1 Chiral symmetry of QCD and its spontaneous breaking

A breakthrough in constructing the theory of nuclear interactions happened with the introduction of the concept of chiral effective field theory for low-energy QCD [17]. This effective theory is based on a phenomenon called spontaneous breaking of the chiral invariance of QCD [18].

If we confine ourselves to u and d quarks, i. e., exclude strange and heavy quarks from consideration, then the masses of the current quarks are small ($m_u = 4$ MeV, $m_d = 6$ MeV) as compared to the characteristic scale of QCD $M \sim 1$ GeV [18]. Therefore, the approximation by zero quark masses $m_q = 0$, i. e., chiral limit, is expected to be reasonable. Let us consider the QCD Lagrangian

$$L_{QCD} = L_{quarks} + L_{gluons} = \sum_f \overline{\psi_f}(i\gamma^\mu D_\mu - M)\psi_f + \frac{1}{4}G_{\mu\nu,a}G_a^{\mu\nu}, \tag{1.1}$$

where the summation is carried out over quark flavors f, Lorentz indices $\mu, \nu = 0, 1, 2, 3$ and color indices a; γ^μ are the Dirac matrices, $D_\mu = \partial_\mu - ig\frac{\lambda_a}{2}A_{\mu,a}$ is the gauge-covariant derivative, which includes the interaction of quarks with a gluon field

$A_{\mu,a}$, $G_{\mu\nu,a}$ is the gluon field tensor; M is the quark mass matrix. If we set $m_q = 0$ in the QCD Lagrangian (1.1) and use the well-known property of the matrix elements of the Dirac gamma-matrixes γ^μ: $\overline{\psi}\gamma^\mu\psi = \overline{\psi_L}\gamma^\mu\psi_L + \overline{\psi_R}\gamma^\mu\psi_R$, where $\psi_L = \frac{1}{2}(1-\gamma_5)\psi$ and $\psi_R = \frac{1}{2}(1+\gamma_5)\psi$ are the left and the right quark fields, then the quark term of the QCD Lagrangian (1.1) can be rewritten in the following form:

$$L^0_{QCD} = \sum_f (\overline{\psi_{fR}} i\gamma^\mu D_\mu \psi_{fR} + \overline{\psi_{fL}} i\gamma^\mu D_\mu \psi_{fL}). \tag{1.2}$$

This expression shows that in the chiral limit, the left and right components of massless quarks do not mix in the Lagrangian, but participate in it additively and equitably, and that the Lagrangian is the sum of the contributions of the left and right quarks $L_{QCD} = L_L + L_R$. The isospin symmetry $SU(2)$ is expanded to independent isospin symmetries separately for left and right quarks $SU_L(2) \times SU_R(2)$. This symmetry is called the chiral invariance of the strong interactions. Mathematically, this symmetry is equivalent to vector – axial vector symmetry $SU_V(2) \times SU_A(2)$.

Thus, according to the obtained Lagrangian, the hadronic world should be divided into the worlds of left and of right quarks. Or, according to the chiral symmetry of the QCD Lagrangian (1.1), (1.2), in the world of hadrons, along with the well-known isotopic multiplets ($SU_V(2)$-symmetry), there should also exist mirror multiplets ($SU_A(2)$-symmetry), which contain the same states with the same masses and angular momentum, but opposite spatial parity P. However, mirror multiplets in the hadron spectrum are not observed in nature. Such a situation, when the symmetry exists at the level of the Lagrangian, but is absent in the physical states resulting from this Lagrangian, is called spontaneous symmetry breaking.

According to Goldstone's theorem [19], each spontaneously broken continuous symmetry corresponds to appearance of massless bosons (called Nambu-Goldstone bosons) with quantum numbers of the broken-symmetry generators. In the case of the broken $SU_A(2)$ symmetry, these quantum numbers coincide with the quantum numbers of the isotriplet of pions $J^P = 0^-$, $T = 1$. Strictly massless strongly interacting particles do not exist in nature, at the same time pions have an unusually small mass, $135-140$ MeV, which is much smaller than the typical hadron mass ~ 1 GeV. According to Nambu's

conjecture [20], the pions are pseudo-Goldstone bosons. This hypothesis played a decisive role in describing the low-energy interactions of pions with pions and nucleons. Before the discovery of QCD, this approach was called the theory of partial conservation of the axial current [21].

1.2 Low energy effective field theory

Weinberg, in his fundamental works [6–8], formulated the principles of Chiral Perturbation Theory (χPT), which is a low-energy effective theory of QCD. Instead of the original QCD Lagrangian, written in terms of quark and gluon fields, an effective Lagrangian L_{eff} is introduced in terms of the hadron fields – mesons and nucleons. Thus, instead of the true degrees of freedom of quarks and gluons, at low energy, effective degrees of freedom – pions and nucleons – are introduced. The effective chiral Lagrangian is the Lagrangian of the most general form, which satisfies all the symmetries of the initial Lagrangian, including the (broken) chiral symmetry of QCD. As a result, the Lagrangian L_{eff} includes spatial derivatives of pion fields. The presence of these derivatives in the Lagrangian leads to the fact that the intensity of the interaction of pions with hadrons is proportional to the momentum of the π meson Q, and this interaction disappears in the limit of zero momenta $Q \longrightarrow 0$. Therefore, for small Q, the perturbation theory expansion in powers of the pion momenta becomes possible.

The separation of scales in hadron physics is decisive in the construction of χPT. In the hadron spectrum, there is a large gap between the masses of pseudoscalar mesons (pions) and vector mesons $\rho(770)$ and $\omega(782)$. Therefore, it is natural to assume that the pion mass determines a soft scale, $Q \sim m_\pi$, which goes to zero $m_\pi = 0$ in the chiral limit. The pion mass or the momentum of the particular hadronic process should be compared with the scale Λ_χ of the order of ~ 1 GeV. This scale is usually given in the form $\Lambda_\chi \sim 4\pi f_\pi$, where $f_\pi = 93$ MeV is the constant that characterizes the probability of a weak pion decay $\pi \to \mu + \nu$.

The radical difference of χPT from the phenomenological models of NN interactions is that χPT is closely related to QCD. This connection is due to the requirement of

preserving all the symmetries of the original basic theory in an effective theory. The perturbation theory expansion is performed with respect to positive powers ν of the ratio $(Q/\Lambda_\chi)^\nu$, where Q is the typical 3-momentum of a particular hadronic process, and Λ_χ is the typical hadronic scale. The minimum number $\nu = N_{min}$ is the leading order (LO), $\nu = N_{min} + 1$ is the next-to-leading order (NLO), and so on.

The order of the expansion ν corresponding to a particular Feynman diagram is related to the structure of this diagram as follows [22]:

$$\nu = -2 + 2A - 2C + 2L + \sum_i \Delta_i \,; \tag{1.3}$$

here $\Delta_i = d_i + \frac{1}{2}n_i - 2$ is the chiral dimension, d_i is the number of derivatives (pion masses) and n_i is the number of nucleon fields involved in vertex i; A is the number of nucleons, C is the number of separate connected components and L is the number of loops in the diagram. The leading order is the lowest order $\nu = 0$. The NLO occurs at $\nu = 2$, since all contributions for $\nu = 1$ disappear due to the conservation of parity and time reversal invariance.

Modern chiral effective theory of hadrons is formulated as a successive expansion of observables in terms of particle momenta and quark masses (or masses of Goldstone bosons), not only in the tree approximation but also with allowance for loop corrections. The physical basis of the theory is the fact that the spectrum of Goldstone bosons is separated by a gap from the spectrum of other hadrons in the limit of vanishing (or sufficiently small) quark masses. Chiral effective theory, which is applicable in the region $|\mathbf{p}|/\Lambda_{ch} << 1$, is a self-consistent theory rather than a phenomenological model. The theory ceases to work at sufficiently high momenta $|\mathbf{p}| \sim \Lambda_{ch}$.

Chiral symmetry dictates the structure of the operator of each term in the effective Lagrangian. Furthermore, the contributions of heavy mesons and nucleon resonances, which are not explicitly taken into account in chiral effective theory, are integrated into the parameters of the theory called low energy constants (LEC). The numerical values of these constants are not fixed by the chiral symmetry. Theoretical calculation of these coefficients would be equivalent to solving low-energy QCD problems. Recent lattice QCD calculations have made it possible to give a theoretical estimate of the LECs for

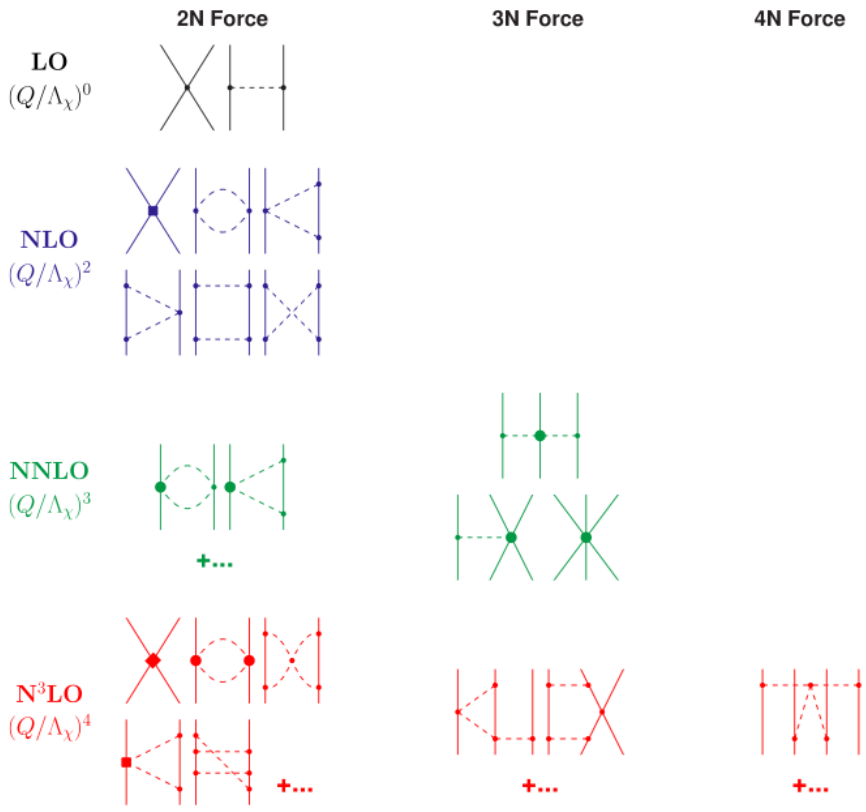

Figure 1.1: Hierarchy of nuclear forces in χPT. Solid lines represent nucleons, dashed lines represent pions. Small dots, large dots, squares and diamonds denote vertices of index $\Delta = 0, 1, 2, 4$, respectively [22].

single- and two-nucleon diagrams [23], while such calculations for diagrams involving more than two nucleons are beyond modern computing power. Since these LECs cannot be calculated in theory, they must be extracted from experimental data.

When performing calculations in χPT, the sum over the expansion powers ν is limited by a specific number $\nu = n$. By increasing n, it is possible to systematically reduce the calculation error. Thus, chiral effective theory makes it possible to perform calculations with accuracy control. This is a fundamental difference from phenomenological models of nucleon interactions. Another difference is that the two-nucleon and three-nucleon forces in χPT are mutually consistent since they are built on a unified basis. In the past two decades, significant progress has been made in the application of χPT to nuclear systems [24], [22].

1.3 Three-body forces

The study of three-body forces began more than half a century ago with the construction of the Fujita-Miyazawa model of forces in [25]. This model describes the process of two-pion exchange with the excitation of the Δ-isobar in the intermediate state (see Fig. 1.2).

The manifestation of three-body forces in elastic *pd*-scattering was found in [26], where it was shown that the Fadeev calculations of the differential cross section at large scattering angles ($\sim 100^\circ - 120^\circ$) based only on two-body forces differ significantly from the experimental data; however, the inclusion of three-body forces makes it possible to reach agreement with the experiment.

According to [27], within the framework of the Hamiltonian approach for the three-nucleon system, the following theorem is true under very broad assumptions about the two-body Hamiltonians H_{ij}. If a three-body Hamiltonian $H(V_{ij}) = \sum_{i=1}^{A=3} t_i + \sum_{i<j}^{A=3} V_{ij}$ contains only two-particle interaction potentials V_{ij} and no three-body forces, then the three-body potentials V_{ijk} can appear in another (unitarily equivalent) three-body Hamiltonian $\overline{H'} = \overline{H}(\overline{V_{ij}}) + \sum_{i<j<k}^{A=3} V_{ijk}$ that describes the same three-body system with different two-body interaction potentials $\overline{V_{ij}}$, which are related to V_{ij} via a unitary

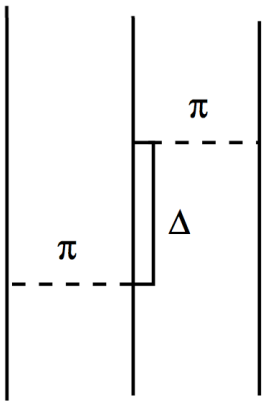

Figure 1.2: The Fujita-Miyazawa three-nucleon force.

transformation. The reason for this is that the unitary transformation connecting two two-body interaction potentials that are equivalent on-shell but different in the off-shell region generates three-body forces. Both three-body Hamiltonians, H and $\overline{H'}$, have the same discrete spectra and lead to identical scattering matrices.

The theorem [27] implies that three-body forces cannot be determined independently of two-body interactions. Thus, any models for three-nucleon forces must be consistent with the two-nucleon NN^- interaction potential, if both two- and three-body forces are used together. A similar requirement is also valid for pair electromagnetic meson exchange currents (MEC), which are analogous to three-body forces. Indeed, the MECs for a system of nucleons depend on the properties of the two-nucleon strong-interaction potential. This dependence occurs due to the conservation of the electromagnetic current $J^\mu(q)$, which can be written in momentum space as $q \cdot J = [H, J^0]$, where q is the transferred four-momentum, J^0 is the time component of the current, and H is the total Hamiltonian of the system. The relation shows that the electromagnetic current $J_\mu(q)$, which contains the MECs, is closely related to the NN interaction included in the Hamiltonian H. Within the framework of χPT for nuclear forces and currents, this requirement for the conservation of the electromagnetic current is satisfied in a natural way, but it presents a serious problem for phenomenological models.

1.4 Meson exchange currents and three-body forces in χPT

1.4.1 Goldberger-Treiman relation

There is a remarkable relation between the axial coupling constant $g_A = 1.276$ [28], which determines the neutron decay $n \to p + e^- + \overline{\nu}_e$, the pion decay constant $f_\pi = 92.4$ MeV, which gives the rate of the weak channel $\pi \to \mu + \nu_\mu$, and the strong πNN coupling constant $g_{\pi NN}$ ($\frac{g^2_{\pi NN}}{4\pi} = 13.8$)

$$g_A = \frac{g_{\pi NN} f_\pi}{M_N}\,, \tag{1.4}$$

where M_N is the mass of the nucleon. The relation (1.4) follows from the approximate conservation of the single-particle axial current A^a and is called the Goldberger-Treiman relation. The Goldberger-Treiman relation relates the strong and weak coupling constants and is actually a consequence of the spontaneous breaking of chiral symmetry. The relation (1.4) holds with an accuracy of $\sim 5\%$. This relation is exactly satisfied only in the chiral limit, i. e., when the masses of light quarks go to zero $m_u = m_d = 0$.

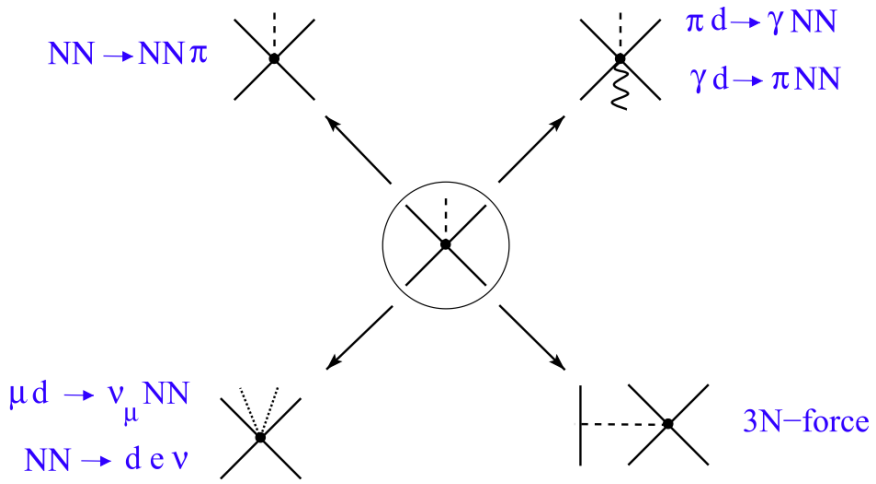

Figure 1.3: The few-nucleon reactions that involve the same LEC [29]

1.4.2 The contact term $(NN)^2\pi$

There is no Goldberger-Treiman-type relation for two-nucleon currents. However, there exists an analogous relationship between different processes - strong and weak - in a system of two nucleons and mesons [30]. Let us consider the term of chiral effective theory that associates the interaction of pions π^a, photons V^μ and axial fields A_μ with an s-state nucleon pair [30]:

$$L_{NN}^{int} = -2dN^+S \cdot u\, NN^+N\,. \tag{1.5}$$

Here, N is the nucleon field (projected onto states with positive energy), S_μ is the Pauli-Lubanski spin (axial) vector, and u_μ is the axial four-vector that contains the pion field π^a and the external vector V_μ and axial A_μ fields:

$$u_\mu = -\frac{\tau^a \partial_\mu \pi^a}{f_\pi} - \frac{\epsilon^{3ab} V_\mu \pi^b \tau^b}{f_\pi} + A_\mu + \dots\,, \tag{1.6}$$

where τ^a is the Pauli isospin matrix, ϵ^{3ab} is a completely antisymmetric tensor, and $a\,,\ b$ are isospin indices. In the two-nucleon sector that is under consideration, the constant d plays a role analogous to that of the constant g_A in single-nucleon systems. The pion field π^a is included in the Lagrangian (1.5) under the derivative sign, $\partial_\mu \pi^a$, which means that the pion is produced (or absorbed) in a p-wave. At the same time, nucleon fields N are included without derivatives and, consequently, correspond to the S-wave initial and final NN pairs.

Substituting the expression (1.6) into the Lagrangian (1.5) leads to a two-particle analogue of the Goldberger-Treiman relation [30]. The resulting Lagrangian describes the local interaction of two S-wave nucleons and an additional field (or a current) associated with the transition between the spin-triplet and spin-singlet states of the NN pair ${}^3S_1 \leftrightarrow {}^1S_1$. The LEC d in the Lagrangian (1.5) determines the strength of the contact term $(NN)^2\pi$. This constant appears in describing the reaction of a single pion production $NN \to NN\pi$ and is also important in a number of other few-nucleon processes. For example, it was shown in [31] that the same contact term $(NN)^2\pi$ is related to a short-distance three-body force arising in three-nucleon systems. At the same time, this constant d plays a key role in other few-nucleon processes, such as the

reaction $pp \to de^+\nu_e$, which is the primary process in stellar thermonuclear reactions, as well as in the deuteron breakup reactions, which were experimentally measured in order to determine the total neutrino flux from the sun. In addition, as follows from (1.5), (1.6), the LEC d is included in the matrix element of pion absorption on the deuteron with creation of a photon $\pi^- d \to nn\gamma$, as well as in weak reactions such as μ-meson capture by the deuteron $\mu^- d \to nn\nu_\mu$ (Fig. 1.3), tritium β-decay, etc. Once the LEC d has been determined from one process, it can be used to calculate observables for other processes.

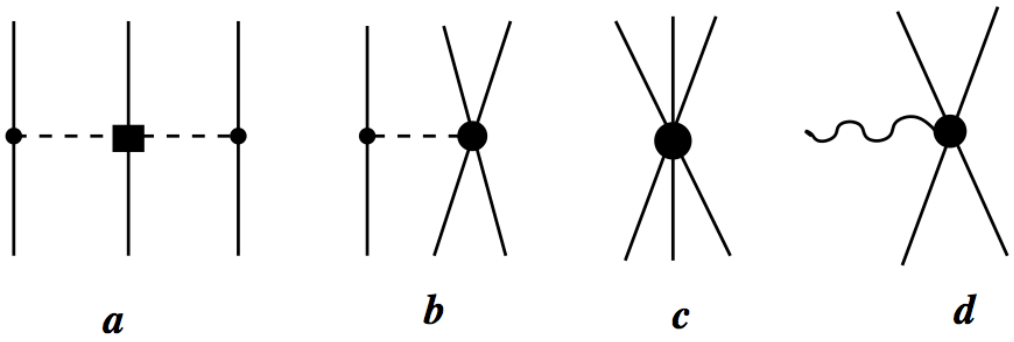

Figure 1.4: Three-nucleon forces (a, b, c) and contact MEC (d) appearing in χPT at N^2LO [17].

In χPT, along with the two-nucleon forces, three-nucleon forces appear in the second order N^2LO and four-nucleon forces appear in the third order N^3LO (see Figure 1.1). It should be noted that the two-body MECs discussed here also appear in the N^2LO order. Chiral theory contains the following three types of three-particle forces in the N^2LO order (Fig.1.4): two-pion exchange (a), one-pion exchange with a contact term $(NN)^2\pi$ (b), and three-nucleon contact interaction (c). The description of three-nucleon interactions and exchange currents up to N^3LO is mainly determined by parameters extracted from two-nucleon interactions. This is also true for the diagram in Fig. 1.4a. The exceptions are the interactions shown in Fig. 1.4b and Fig.1.4c, which are characterized by two additional LECs, c_D and c_E, respectively [32]. The LEC c_D is included in the contact term $(NN)^2\pi$, being linearly related to the parameter d [17] defined in (1.5). The same constant c_D is included in the contact term of the two-particle exchange current (Fig. 1.4d). Three-nucleon forces corresponding to the constant c_D

arise when the virtual pion is produced due to the interaction (1.5) and is then absorbed on the third nucleon. The resulting diagram is shown in Figure 1.4b. The three-nucleon interaction potential corresponding to this diagram has the form [22]

$$V_{1\pi}^{3NF} = -D\frac{g_A}{8f_\pi^2}\sum_{i\neq j}\frac{\vec{\sigma_j}\vec{q_i}}{\vec{q_j}^{\,2}+M_\pi^2}(\tau_i\cdot\tau_j)(\sigma_i\cdot\vec{q_j})\,, \tag{1.7}$$

where $\vec{q}\equiv\vec{p}\,'-\vec{p}$, $\vec{p}$ and $\vec{p}\,'$ are the momenta of the initial and final nucleons, respectively, σ and τ are the spin and isospin Pauli matrices. The parameter c_D is related to the LEC of one-pion exchange D, as $D=\frac{c_D}{f_\pi^2\Lambda_\chi}$. The second LEC c_E determines the strength of the three-nucleon contact term shown in Fig. 1.4c.

1.5 Obtaining LECs from experimental data

The three-body force (1.7) contains a new parameter c_D, which does not arise in the two-nucleon sector. There are several ways to measure this parameter, as well as parameter c_E, from data for few-nucleon systems.

1.5.1 Three-nucleon systems

The parameters c_D and c_E were first determined from the ^3H binding energy and the nd doublet scattering length [32]. However, due to the correlation between these two observables, known as the Phillips line, and a considerable experimental uncertainty in the scattering length, this method could hardly be used for accurate extraction of these constants. Subsequent studies, in addition to using the ^3H binding energy to determine the LECs, also used the ^4He ground state energy [33] or the radius of ^4He [34]. However, both these methods are not self-consistent, since the third order N^3LO was used for two-nucleon forces, whereas the three-nucleon potential was calculated up to the second order N^2LO.

Since the LEC c_D is also included in the two-nucleon current (Fig. 1.4d), one can use the tritium half-life as another observable in addition to the $A=3$ binding energy for determining the LECs c_D and c_E. This was done in [35], where a hybrid method was used: the standard ^3H wave functions with phenomenological NN potentials were

combined with a chiral expansion for the current operators. The next step towards accurately determining the LEC c_D was done in [36], which also used the binding energy and the half-life of ^3H. The N^3LO two-nucleon forces and N^2LO three-nucleon forces were used in [36] to calculate the wave function of the system $A = 3$. It should be noted that, strictly speaking, self-consistent calculations should use the same order of expansion. Constraints for the c_D and c_E constants were also obtained in [37] through a fit to the binding energy $A = 3$ and the ^3H Gamow-Teller matrix element. Thus, the c_D and c_E were extracted from the tritium β-decay and its binding energy in [35] and [36]. The value of the extracted d-constant was used to predict the S-factor of the reaction $pp \to de^+\nu_e$ in [35]. Using χPT, it was shown in [36] that both ^3H and ^3He binding energies and tritium β-decay can be described with the same contact term d. Nevertheless, some questions remain about the accuracy of determining these parameters from the data for three-nucleon systems [17]. Although there are reasons to believe that using χPT for the 3N system is reliable, general considerations make it clear that determining the constant d from the data for two-nucleon systems is necessary in order to provide an independent cross-check of the formalism.

1.5.2 Two-nucleon systems

$pp \to de^+\nu_e$ reaction

The contact term d is contained in the Gamow-Teller matrix element for the reaction $p+p \to d+e^+ +\nu_e$, which is of fundamental importance for understanding the evolution of stars and the physics of solar neutrinos. The modern theory of stellar evolution and the solar model require the accuracy of 1% in determining the $S(0)$-factor proportional to the cross section of the process [40]. The first calculations of this process were made by Bethe and Crichfield [41] more than 70 years ago. Their estimations were improved in [42]. Subsequently, fine effects (electromagnetic radioactive corrections and vacuum polarization in the Coulomb interaction) were taken into account in [43]. The most thorough calculations of the process $p + p \to d + e^+ + \nu_e$ within the framework of the potential model approach were made in [44]. Recently, high-precision models of

phenomenological potentials [44] and effective field theory [35] have been used to study this process.

The astrophysical S-factor of this reaction at zero energy is determined from the transition matrix element, the basic uncertainty of which arises mainly from the normalized Gamow-Teller matrix element $\overline{\Lambda}$, which binds the pp and the deuteron states [40]. In this paper, the authors show that the Gamow-Teller matrix elements for the pp fusion and the tritium β-decay are related by the same constant. According to this paper, the predictions using five high-precision phenomenological potentials lie in the narrow interval $7.05 \leq \overline{\Lambda}^2 \leq 7.06$.

The three-particle forces and currents included in the tritium β-decay are the source of uncertainty for $S(0)$. A hybrid approach was used in [35]: the transition operators for the tritium β-decay were determined from χPT but were sandwiched between phenomenological wave functions generated by a potential model. The calculations [35] were carried out up to N^3LO and, after fitting the MECs with the LEC $\widehat{d}^R$ obtained for the tritium β-decay, yielded $\overline{\Lambda}^2 = 7.03(1 \pm 0.008)$ [35]. The astrophysical factor was determined to be $S(0) = 3.94 \times (1 \pm 0.004) \cdot 10^{-25}$ MeV·b [35]. In [45], the S-factor in the framework of χPT was determined to be $S(0) = (4.030 \pm 0.006) \cdot 10^{-25}$ MeV·b. The theoretical uncertainty arises from the fitting of the LECs and the cutoff dependence found in [37].

$\pi^- d \to \gamma nn$ reaction

As noted above, the transition matrix element of the reaction $\pi^- d \to \gamma nn$ contains the contact d-term. In addition, this reaction contains information about another fundamental parameter, the nn scattering length a_{nn}. The a_{nn} values extracted from experimental data on this reaction in [46] were obtained with a large error: $a_{nn} = \pm 0.4$ fm. Furthermore, it was shown in [47], [39] that 0.3 fm out of the total uncertainty of ± 0.4 fm arises from the short-range part of the NN wave function. Taking into account the d-term from independent data on the reaction $pp \to de^+\nu_e$ in [30] made it possible to significantly reduce the error in determining a_{nn}. The correlation between the $pp \to de^+\nu_e$ and $\pi^- d \to \gamma nn$ reactions was studied in [30]. The value of the d-term

was fixed in [30] using the Gamow-Teller matrix element obtained with the potential approach for the $pp \to de^+\nu_e$ reaction in [44]. This constant was then used in [30] in calculating observables for the $\pi^- d \to \gamma nn$ reaction. Thus, it was found in [30] that, when using a fixed value for the d-term, the theoretical uncertainty for the nn-scattering length extracted from $\pi^- d \to \gamma nn$ is reduced by a factor greater than 3, to ≤ 0.05 fm.

$\mu^- d \to nn\nu_\mu$ reaction

The reaction of muon capture on the deuteron $\mu^- d \to nn\nu_\mu$, as well as the reaction $pp \to de^+\nu_e$, makes it possible to reduce the uncertainty in determining the LEC d. The process $\mu^- d \to nn\nu_\mu$ does not contain three-body effects and is therefore simpler for theoretical interpretation than $A = 3$ reactions. The doublet capture rate of muon on deuteron $\Lambda_{1/2}$ is known with a low accuracy $\sim 6 - 10\%$. The $\Lambda_{1/2}$ parameter was calculated theoretically in [48] within χPT using the constant c_D extracted in [36] from the tritium β-decay and its binding energy. The values obtained for $\Lambda_{1/2}$ show a large spread depending on the values of c_D that were used. It is important to emphasize that the MuSun collaboration [49] aimed to measure $\Lambda_{1/2}$ with an accuracy of 1.5%. Thus, if this effort is successful, the MuSun data will allow us to significantly constrain the uncertainties in determining c_D. Currently, the experiment is completed and the results are being analyzed [50].

1.6 Using the $pp \to \{pp\}_s\pi^0$ and $pn \to \{pp\}_s\pi^-$ reactions for extracting the contact d-term

The reactions of single-pion production in nucleon-nucleon collisions provide another possibility to extract the LEC d (or c_D). In this case, as follows from the form of the Lagrangian (1.5), (1.6), it is necessary to consider processes with the production of p-wave pions $NN \to NN\pi$, which connect S-wave pairs of initial and final nucleons.

1.6.1 Analysis of the allowed transitions

There are two reaction channels that satisfy this condition, differing by the spin of the NN pair, $S = 0$ and $S = 1$.

A. The final NN pair is forming in the spin-triplet S-state $^3S_1$, and the initial NN pair is in the spin-singlet S-state $^1S_0$. Such a transition $^1S_0 \to {}^3S_1p$, where p indicates the pion orbital momentum $l = 1$, takes place in the $pp \to pn\pi^+$ reaction. Other transitions with the formation of a final $^3S_1$ pair do not contain the d-term. Indeed, the final ^3S_1p state of the $NN\pi$ system can be formed in the $pp \to d\pi^+$ (or $pp \to pn\pi^+$) reaction from the initial $^1D_2$ state (or higher partial waves), which obviously excludes the d-term from this transition. Finally, in other channels of reactions with deuteron formation, $pp \to d\pi^+$ and $pn \to d\pi^0$, the final $^3S_1$ state of NN is accompanied by the s-wave pion production, while the initial nucleon pair is in the P-state [29], which is also incompatible with the condition of including the d-term.

B. Another allowed transition with the d-term contains a spin-singlet ($S = 0$) S-wave nucleon pair in the final $^1S_0$ state with a p-wave pion. Such a transition takes place in the isosinglet ($I = 0$) channel of the $pn \to \{pp\}_s\pi^-$ reaction. Here and below, $\{pp\}_s$ denotes the $^1S_0$ state of the pp-pair, which is implemented in the experiment by limiting the pp-pair excitation energy to $E_{pp} < 3$ MeV. It should be noted that, in the isosinglet channel of this reaction, a transition from the initial triplet D-wave to the final ^1S_0p state is also possible: $^3D_1 \to {}^1S_0p$. This transition does not contain a contact d-term, but there is a strong coupling of the channels $3S_1 - {}^3D_1$ because of the tensor interaction between the initial nucleons. The isotriplet channel ($I = 1$) of the $NN \to \{pp\}_s\pi$ reaction allows only transitions to states with even orbital angular momenta of the final pion, so it does not contain a contact d-term either.

It is necessary to choose the optimal alternative to determine the d-term from the single-pion production $NN \to NN\pi$. When choosing between the alternatives A and B, it should be noted that it is hardly possible to extract the LEC d with a high accuracy using channels with isovector initial states (for example, $pp \to pn\pi^+$ and $pp \to d\pi^+$), although they can be helpful in placing restrictions on d. Thus, for reactions with a

pp-pair in the initial state and p-wave mesons in the final state, two partial waves exist: ${}^1S_0 \to {}^3S_1p$ and ${}^1D_2 \to {}^3S_1p$. The contact term contributes only to the ${}^1S_0 \to {}^3S_1p$ transition and does not contribute to ${}^1D_2 \to {}^3S_1p$; at the same time, the amplitude of the ${}^1D_2 \to {}^3S_1p$ transition is much greater numerically due to the strong coupling of the initial NN channel with the Δ-isobar excitation channel ${}^5S_2$ $N\Delta(1232)$. In addition, the final nucleons in the $pp \to pn\pi^+$ reaction can contribute not only to the S-waves but also to higher partial waves, which makes it difficult to determine the LEC.

On the contrary, the $pn \to \{pp\}_s\pi^-$ reaction with the formation of a spin-singlet final diproton is more preferable for reliably extracting the d-term [51]. In this reaction, the LEC d is included only in the isoscalar amplitude ${}^3S_1 \to {}^1S_0p$, which, however, is strongly related to the ${}^3D_1 \to {}^1S_0p$ transition due to the tensor interaction in the $S = 1$ state of the initial nucleons. To separate the ${}^3D_1 \to {}^1S_0p$ transition from the ${}^3S_1 \to {}^1S_0p$ transition, it is necessary to carry out a partial-wave analysis of the spin amplitudes describing the reaction $pn \to \{pp\}_s\pi^-$. In order to separate the isovector channel ($I = 1$) from the isoscalar channel ($I = 0$) in the amplitude of the $pn \to \{pp\}_s\pi^-$ reaction, it is necessary to measure the same observables for the two reactions $pp \to \{pp\}_s\pi^0$ and $pn \to \{pp\}_s\pi^-$ in the same kinematics. Both these problems – extracting the isoscalar channel of the $pn \to \{pp\}_s\pi^-$ reaction and carrying out the partial-wave analysis of its spin amplitudes – are the main tasks of the thesis.

The possibility to determine the LEC d from the $pN \to NN\pi$ reaction was first indicated in [31]. However, it was shown that, in this case, the initial proton momentum in the center-of-mass system is $p \approx \sqrt{m_\pi M_N} \sim 360$ MeV, therefore, the perturbation-theory expansion parameter for the $NN \to NN\pi$ reaction should be of the order of $\chi \sim p/\Lambda_\chi \sim \sqrt{m_\pi/M_N} \sim 0.4$, which is noticeably larger than the typical order of this parameter in χPT, $\chi \sim m_\pi/\Lambda_\chi \sim 0.14$. This means that, when describing the $NN \to NN\pi$ reactions within chiral theory, one should expect a slower convergence of the perturbation theory series. The restrictions on the LEC d were obtained in [31] by studying the ${}^1S_0 \to {}^3S_1p$ transition in the $pp \to pn\pi^+$ reaction. Another attempt to extract the LEC d was made in [52], which led to a negative result. Later, the results and conclusions of [52] were criticized in [53]. It was shown in [53] within χPT that

a combined analysis of the p-wave amplitudes of pion production contributing to the reactions $pp \to d\pi^+$, $pp \to pn\pi^+$ and $pn \to pp\pi^-$ provides a good general description of the differential cross sections and analyzing powers A_y for different channels of $NN \to NN\pi$ with the same value of the LEC d, which turns out to be of the order of $d \sim 3/(f_\pi^2 M_N)$ for the NN interaction described in the coupled channel model [54]. In this case, from the three alternatives $d = 3, 0, -3$ (in the units of $f_\pi^2 M_N$), the value $d > 0$ was found to be the most preferable.

Finally, let us note that the interest in processes involving the formation of a ${}^1S_0$-diproton $\{pp\}_s$ in the final state of reactions in few-nucleon systems with large momentum transfer is related to [55]. In this work, in order to to solve the well-known T_{20} problem found in elastic pd backward scattering in the energy range $0.5 - 1$ GeV, it was proposed to investigate the process $pd \to \{pp\}_s n$ in the elastic pd backward scattering kinematics in the $\Delta(1232)$-isobar region, a theoretical model for this process was developed, and qualitative differences of this process from the analogous reaction with the deuteron in the final state were shown. The advantages of a channel with a final ${}^1S_0$ diproton are its isospin $I = 1$ and spin-parity $J^\pi = 0^+$. These quantum numbers differ from those of deuterons, so reactions with a diproton in the final state are described by different transition amplitudes as compared to analogous (in terms of kinematics) reactions with a final deuteron, which provides a new nontrivial test of the pd scattering dynamics [55]. In addition, since the spin of the diproton is zero, the spin structure of the reaction amplitude of $pN \to \{pp\}_s \pi$ is much simpler than for the deuteron channel. In particular, for some reactions with a final diproton and a pion, only a few spin observables are required to reconstruct all the independent spin amplitudes of the process. The deuteron breakup reaction with the formation of a diproton $pd \to \{pp\}_s n$ at large transferred momenta was studied in the ANKE@COSY experiment [56, 57]. The dominance of the ${}^1S_0$ state in the internal motion of the pp system at $E_{pp} < 3$ MeV was demonstrated by measuring the internal angular and energy dependencies for the proton pair in the final state. The developed experimental technique for detecting the $\{pp\}$ pair was later applied at ANKE@COSY to investigate a number of other reactions [58], [59], [60], [61].

1.6.2 Available experimental data

When limited to the s-, p-, and d-waves of π-mesons produced in the reaction $pn \to \{pp\}_s\pi^-$, this reaction is described by five partial amplitudes. Therefore, to carry out the partial-wave analysis, it is necessary to measure nine independent real parameters (observables), [1] which will allow us to extract the contact d-term $(NN)^2\pi$ in a model-independent manner. A part of the information needed was obtained by measuring the unpilarized differential cross section in the WASA-CELSIUS experiment for a beam energy of 350 MeV, which made it possible to obtain two expansion coefficients of the differential cross section in powers of $\cos\theta$ in 4.9 (see Chapter 4).

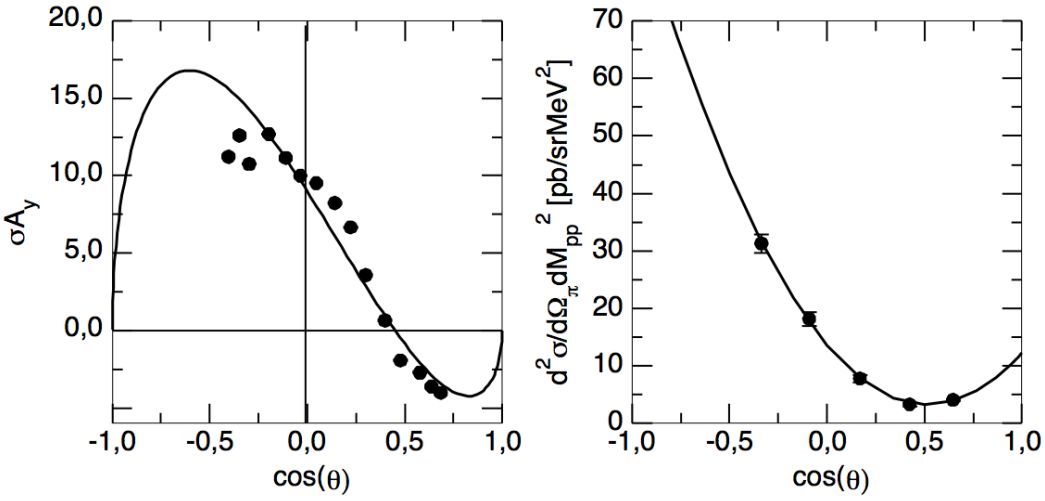

Figure 1.5: Analyzing power and differential cross section of the $np \to \{pp\}_s\pi^-$ reaction for the energy $T_n = 353$ MeV and with the proton pair excitation energy cut $E_{pp} < 1.5$ MeV. Experimental data are taken from [9] and [10]. The solid line shows the fit of a second-order polynomial function with respect to the pion momentum.

The A_y and $d\sigma/d\Omega$ measurement in the quasi-free process $np \to \{pp\}_s\pi^-$ potentially allows to find a larger number of coefficients in the expansion on $\cos\theta$. Based on the data of the TRIUMF experiment [9, 10] of measuring A_y and $d\sigma/d\Omega$ in the process $np \to \{pp\}_s\pi^-$ at 353-440 MeV, the authors of this experiment carried out a partial-wave analysis with consideration for five amplitudes.However, the angular range, as can

[1] The phase common for all amplitudes is immeasurable and therefore can be chosen arbitrarily.

be seen from the data given for the TRIUMF experiment in Fig.1.5, is much narrower than the full interval $[0, \pi]$. Therefore, the procedure for selection of the expansion coefficients by Legendre polynomials in this case is ambiguous in principle. And the authors of [9] actually found several solutions of the partial-wave analysis for all energies, finding it difficult to choose a physically meaningful solution. Particularly, the authors of [9] obtained a very small contribution of the π-meson d-wave at this energy of 353 MeV, which is in contradiction with the measurements of CELSIUS [63].

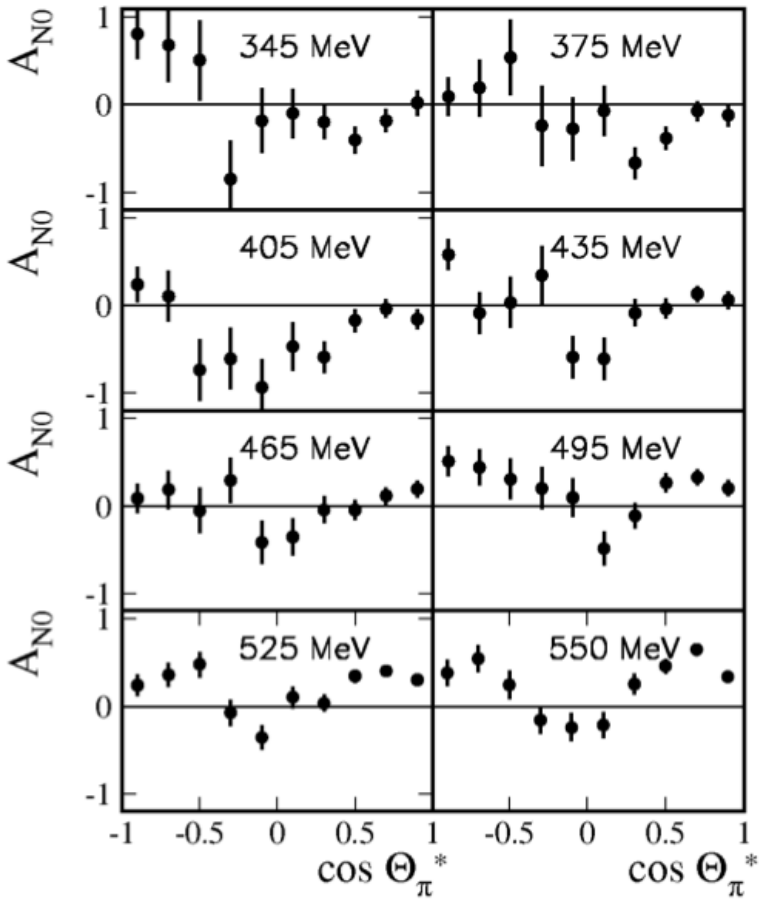

Figure 1.6: Analyzing power (A_{N0}) for a quasi-free reaction with a cut on the proton pair excitation energy $E_{pp} < 6$ MeV. The figure is taken from [11].

The data for the analyzing power from PSI [11] (see Fig. 1.6) were obtained with a cut on the excitation energy of $E_{pp} < 6$ MeV and therefore can not be used in the

partial-wave the analysis of the amplitudes of the $pn \to \{pp\}_s\pi^-$ reaction in which the proton pair $^1S_0$ selection is required. Nevertheless, even with this weaker restriction on energy, the results have significant errors in the region of backward pion emission for $T_n = 345$ MeV. The unpolarized cross section of the $dp \to p_{sp}pp\pi^-$ reaction for the considered energy region was also obtained by the collaboration $COSY - TOF$ [64]. In spite of the fact that the pp pair was singled out, insufficient statistics did not allow for a strong restriction on the excitation energy.

Thus, before the experiments discussed in this paper, only data on $d\sigma/d\Omega$ and A_y in an incomplete angular range were obtained at the beam energy of 353 MeV. The aim of the ANKE experiment [65] was to expand the angular range of $A_y(\theta)$ and to add the spin correlations $A_{x,x}$ and $A_{x,z}$ to the set of the observables, which would allow conducting a complete polarization experiment, i. e. finding values of both spin amplitudes (see Sec. 4.1) and their relative phase, and on this basis to carry out a partial-wave analysis and, as a result, determining the $^3S_1 \to {}^1S_0p$ transition amplitude containing the contact d-term.

Chapter 2

Experimental equipment

2.1 COSY accelerator and storage ring

The experiment was carried out at the ANKE setup [66] of the COSY ("COoler SYnchrotron") accelerator complex [67] located at the Forschungszentrum Jülich (Germany). The layout of COSY is shown in Fig. 2.1.

The COSY accelerator provides high precision polarised and unpolarised proton and deuteron beams. The total circumference of the storage ring is 184 m. The machine covers the momentum range of accelerated particles from 295 MeV/c up to 3.65 GeV/c, which corresponds to an energy range from 45 MeV to 2.83 GeV for protons.

COSY beams are being delivered to internal (ANKE, WASA, COSY–11, EDDA) and external experiments (TOF, BIG KARL), but the latter are not of importance for the current discussion.

In the case of polarized beams, H^- and D^- ions from the polarized ion source are pre-accelerated in the cyclotron JULIC, pass through the charge–exchanging carbon foil and then injected into the storage ring. After the injection process, the particles are accelerated up to desired energy by the electric field, and are focused and held in the storage ring by the magnetic field. The accelerated beam can both circulate in the ring and be output to an external target. The accelerator is equipped with electron and stochastic cooling systems which provide a monochromatic beam at the level of $\delta p/p \sim 10^{-4}$, whereas for an uncooled beam this parameter is 10^{-3}. In the measurements

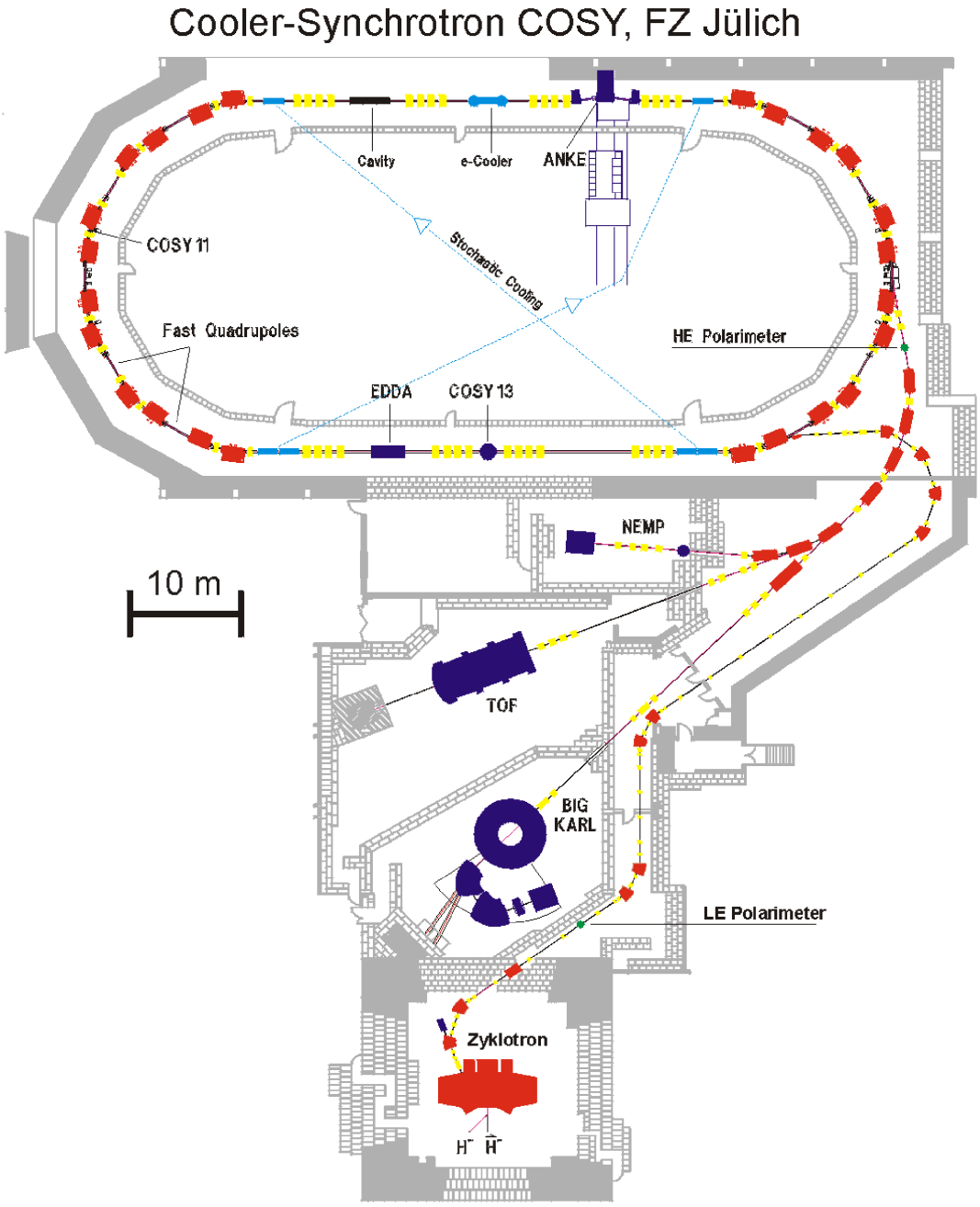

Figure 2.1: The COSY synchrotron.

considered, only electron beam cooling after injection and acceleration was used, which made it possible to accumulate particles in the ring from a set of consecutive injections for joint acceleration (the stacking process). This approach increased the intensity of the accelerated polarized beam up to 10 times.

The particle number accumulated in the ring for unpolarized beam is on the order of $\sim 10^{10}$, and the circulation frequency is $\sim 10^6$ Hz. The intensity in the case of polarized beam after a single injection was 5-10 times lower than for unpolarized beam which was partially compensated by the use of stacking.

2.1.1 Polarized ion source

The polarized ion source at COSY [68, 69] produces negatively charged hydrogen and deuterium ions, which then undergo a charge–exchange procedure and are injected into the storage ring. The source setup is shown in Fig. 2.2. The source consists of several components: an atomic beam source, a radio-frequency dissociator, a system of sextuples, a charge-exchange region, a deflector magnet, and a Wien filter.

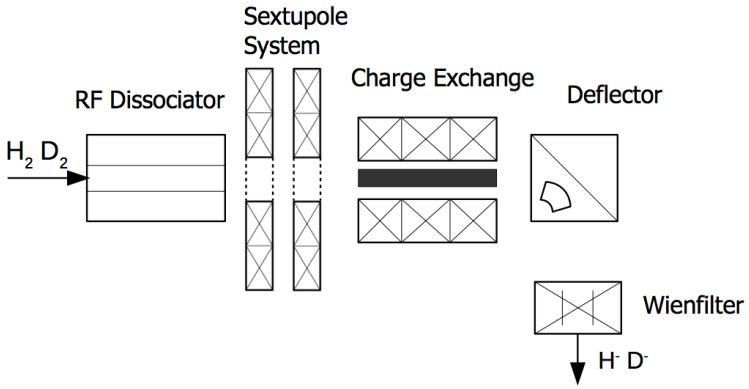

Figure 2.2: Setup of the polarized ion source.

First, neutral and unpolarized deuterium or hydrogen gas pass through a radio-frequency dissociator in which, under the action of the high frequency electromagnetic field, free electrons accelerate and excite vibrational levels of the molecules. As a result of excitation, the molecules break up into atoms, and the resulting atomic beam enters

a sextupole magnetic system. The first sextupole defocuses atoms with an electron spin state $m_j = -1/2$, while atoms with the spins $m_j = +1/2$ remain in the beam. The second sextupule plays the role of an achromatic lens, which focuses the beam into the charge-exchange ionization region. Here, the atomic beam interacts with neutral cesium atoms. Since electronegativity of hydrogen is much higher than of cesium, hydrogen receives an additional electron: $\overrightarrow{H^0} + Cs^0 \rightarrow \overrightarrow{H^-} + Cs^+$. Finally, the resulting ion beams H^- and D^- are turned with a toroidal deflector by 90^o and fall on the cyclotron injection line. Here, with the help of the Wien filter, electrons and other backgrounds are removed from the ion beam, then pre-accelerated in the JULIC cyclotron and injected into the storage COSY ring through the charge-exchange carbon foil.

2.2 ANKE spectrometer

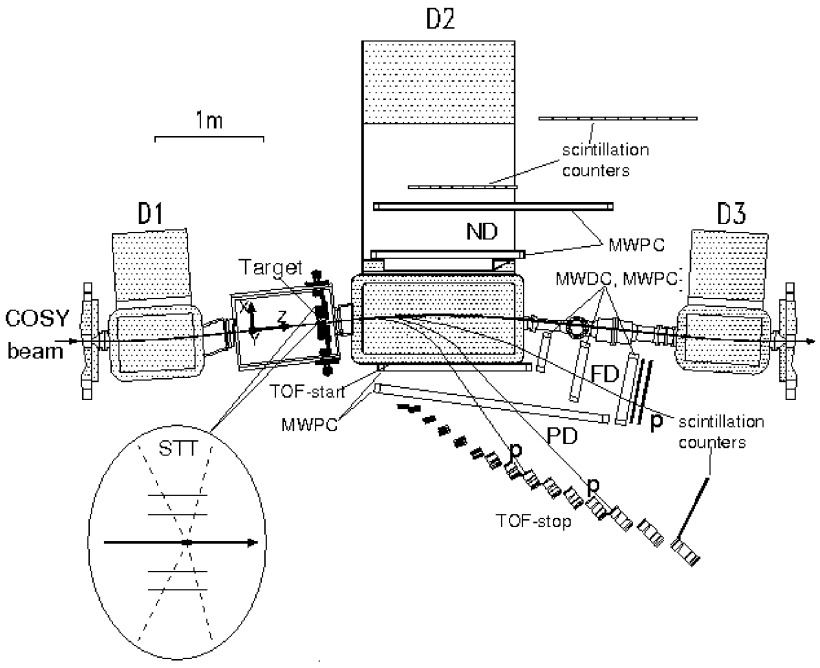

Figure 2.3: Scheme of the magnetic spectrometer ANKE.

A magnetic spectrometer of charged particles ANKE (Apparatus for Studies of Nucleon and Kaon Ejectiles) was located on one of the linear sections of the COSY accelerator ring [66]. The ANKE scheme is shown in Fig. 2.3.

The main components of the spectrometer are a magnetic system, an internal target, and several detector systems (side detectors of positive and negative particles, front and vertex detectors). The ANKE magnetic system consists of three dipole magnets. Two magnets, D1 and D3, change the trajectory of the accelerator beam, deflecting it by an angle α (varying from 0^0 to 10.6^0) from the inner orbit to the target in the target chamber and returning the beam to the nominal orbit after the interaction with the target. The main spectrometer dipole magnet D2 deflects the beam by an angle 2α.

2.2.1 Targets types

In the discussed experiments, two types of targets were used. A cluster target produces only unpolarized hydrogen or deuterium jets of high density, and a polarized target with a storage cell provides both polarized and unpolarized hydrogen or deuterium beams.

Unpolarized cluster target

The cluster target at ANKE consists of three main parts: a cluster source, an analyzing chamber, and a beam ejector [70]. Clusters of $10^3 - 10^4$ atoms are produced in the Laval nozzle, which is cooled to 20 K. The resulting cluster beam, surrounded by a gas beam, reaches a conical hole of 700 μm in diameter, which works as a skimmer. Thus, only a well-formed cluster passes the skimmer and enters the analyzing chamber, where the density of the cluster beam is measured. The density reached values up to 10^{14} atoms/cm^2.

Polarized target with storage cell

To implement the experiment with double polarization, one should use an internal polarized target with a storage cell (PIT - Polarised Internal Target) [71]. The components of the target are:

– an atomic beam source (ABS),
– a storage cell,

– a Lamb-shift polarimeter (LSP), which allows to quickly measure the polarization of the target gas.

The use of a storage cell allows to increase the target density by two orders of magnitude.

The atomic beam source produces a beam of polarized hydrogen or deuterium atoms with an intensity of $6 \cdot 10^{16}$ atoms/s for hydrogen atoms and $4 \cdot 10^{16}$ atoms/s for deuterium. ABS is located between the dipole magnets D1 and D2. The setup consists of a dissociator in which the hydrogen or deuterium molecules dissociate into H and D atoms, and a set of sextuple magnets and radio-frequency nodes where atomic beam was polarized. Atomic hydrogen or deuterium leaves the dissociator and then the beam is formed by a filter made of steel and a collimator whose geometry is chosen so that the beam deviates, falling into the acceptance of the sextuples magnetic system. The density of the polarized gas jet at the ABS exit was about $\sim 10^{11}$ atoms/cm^2.

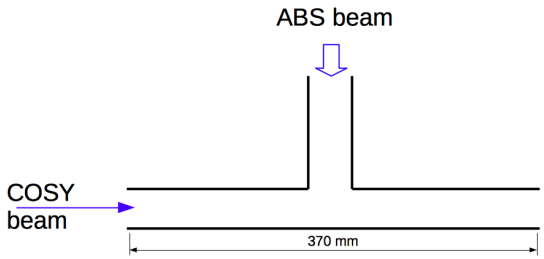

Figure 2.4: Storage cell.

The storage cell is a T-tube opened on both sides (Figure 2.4), into which gas is injected from the ABS source. The tube size is $20 \times 15 \times 370$ mm^3, the walls of the tube are made of aluminum foil of 20 μm thick, covered with a 5 μm Teflon layer, which prevents surface recombination of polarized atoms. The polarization of the gas in the cell is preserved due to the scattered field of the magnet D2. The main vertical field component exceeds the critical value necessary to preserve the polarization over the entire length of the cell and entrance tube. The resulting target density was $1.3 \cdot 10^{13}$ atoms/cm^2. The cell design allows not to destroy the beam and carry on measurements with a circulating (up to several hours during the use of cooling) accelerating beam.

2.2.2 Detection systems

The ANKE spectrometer is equipped with the following detection systems:

- a Front Detector (FD),
- a detector of positive particles (PD - Positive Detector),
- a detector of negative particles (ND - Negative Detector),
- a vertex detector - Silicon Tracking Telescope (STT).

Multiwire proportional cameras (MWPC) used for track reconstruction and scintillation counters for obtaining the information on time of flight and energy of particles are installed in the side detectors and FD. In the PD and ND, the time of flight is measured between the start and stop counters. In order for this time to be maximum the start detectors are located directly outside the D2 window. Information on energy loss is also used to identify particles. The momenta acceptance limits for the PD and ND were $(0.15 - 1.1)$ GeV/c, for the FD — $(0.4 - 3.7)$ GeV/c.

Front detector (FD)

The front detector, shown in Fig. 2.5, includes multiwire proportional cameras (indicated as MWPC on the diagram), a drift chamber (MWDC), and two layers of scintillation counters.

Parameters of the detector are given in articles [72,73], except for the camera system, which was replaced before the measurements considered in the thesis took place. With that the first proportional chamber was replaced with MWDC, which contains three planes of vertical wires and four planes of wires inclined by 30^o, with a pitch between the wires of 1 cm and the same distance between the planes. The chamber operates with gas mixture of $C_2H_6(20\%) + Ar$ and allows a resolution of $\sigma = 260$ μm to be achieved.

Two other cameras with a 1.05 mm wire pitch were replaced with proportional cameras with twin planes with a pitch of 2.06 mm (MWPC in Figure 2.5). Each MWPC contains a pair of wire planes with vertical wires (X), and a pair with horizontal wires (Y). The two planes of the pair are shifted relative to each other by half of a wire pitch with a distance between planes of 2 mm. This allows to achieve a spatial resolution

close to the cameras with 1.05 mm pitch, without the use of a supporting film, which simplifies the cameras design and operation. One of the cathodes from the pairs of X, Y planes is striped with a strip incline of $\pm 30^o$ and a pitch of 5 mm.

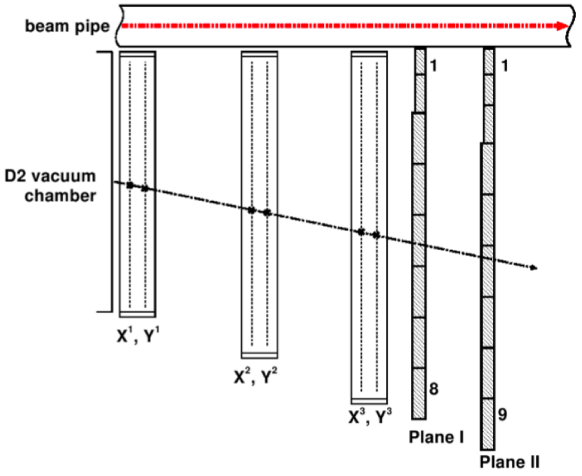

Figure 2.5: Scheme of the forward detector.

The detector is located between the dipole magnets D2 and D3 close to the beam channel. The space available is very limited. The distance between the magnets is about 1.6 m. Since the cameras are located close to the beam, the system operates at high loads. Moreover a good spatial resolution of the multiwire chambers (< 1 mm) is necessary in order for momentum resolution to be no worse than 1%, which in turn is necessary for selection of proton-proton pairs with low excitation energy.

The front scintillation hodoscope consists of two planes of separate counters. In the first plane there are 8 counters and 9 are in the second, the sizes of the counters vary from 4 to 8 cm in width and from 1.5 to 2 cm in thickness. The counters of one plane are shifted by a half the width of one counter relative to the other plane. The signal time and amplitude information is read using photomultipliers located at both ends of each scintillator. The scintillation counters provide a trigger signal, information on energy loss and allow to determine the time of flight difference for particle pairs passing through different counters. Information analysis from the hodoscope allows to determine energy loss with an accuracy of 10% and the time of flight difference for two-particle events with an accuracy of 0.2 ns.

The angular acceptance of the FD is about 12^0 horizontally and 3.5^0 vertically.

Positive detector (PD)

The positive detector is intended for detection of particles with momenta in the range of $150-1100$ MeV/c moving into the forward region. It consists of 23 starting counters, two multiwire proportional chambers, and 15 tracking telescopes, supplemented from the high momenta side with a hodoscope of 6 scintillation counters ("side wall"), as shown in Fig. 2.3.

The scintillation start counters are located next to the exit window of the spectrometer magnet D2. Each particle, detected by the PD, passes through one counter and then enters the multiwire proportional chambers for track reconstruction and then goes to one of the telescopes or the side wall. In each chamber there are three planes of anode wires (vertical, inclined by $+30^\circ$ and -30°). The cathode planes are located at a distance of 5 mm from the anode ones. Information from the proportional chambers about particle tracks makes it possible to determine particle momenta with an accuracy of $2-3\%$.

The telescopes are located in the focal plane of the spectrometer magnet D2, and each of them covers a momenta range of about 30 MeV/c. Each telescope consists of a scintillation stop counter working on coincidence with the start counters, an energy loss ΔE counter, a veto counter and two copper passive absorbers which stop the protons from the target. Only stop counters were used at the data analysis of the discussed experiments. The side wall closes the gap between the last telescope and the FD hodoscope and is located outside the focal plane D2.

Negative detector (ND)

The negative detector was used to register the π^- mesons. It is partially located inside the gap of the yoke (active cavity) of the spectrometer magnet D2 and consists of 20 scintillation start counters and 22 stop-counters divided into two groups, used for time-of-flight and energy loss identifications. The start counters are located next to the

exit window of the magnet D2. The first group of stop counters is located inside the yokes gap of the D2, and the second group is located outside the gap of the magnet.

Inside the D2 dipole magnet, two multiwire proportional chambers are installed, which are necessary for track reconstruction, with a momentum accuracy up to $\Delta p/p \approx 2-3\%$. The design of the ND multiwire proportional chambers is similar to that of the PD chambers.

Silicon Tracking Telescope

The silicon tracking telescope is designed to detect low-energy protons and deuterons emitted from the target and to reconstruct the tracks of the registered particles. The telescope consists of three silicon detectors having strip structure on two sides to determine the particle track coordinates. There are vertical and horizontal strips on each side of each detector.

The energy loss measurement in each individual layer allows to identify the stopped particle. A proton can be registered in the case when it passes at least one layer. Thus, the minimum energy of the detected proton is determined by the thickness of the inner layer. The maximum registered energy of a proton is determined by the total thickness of all layers. Therefore, the main goal in the STT construction was to provide minimum thickness of the inner layer and at the same time maximum thickness of the outer layer. The thickness of the tracking telescope layers in order from the inner to the outer are 60 μm, 300 μm and 5100 μm. The proton identification by $\Delta E/E$ is possible for energies from 2.5 to 40 MeV. The energy resolution of the STT is of 150-250 keV.

2.3 Data-taking

2.3.1 Trigger structure

During the measurement, the information was read from the detectors by signals of a trigger module. There were used several trigger sets the signals of which were fed to the trigger module inputs. While the data was being read (deadtime of the system), the system was blocked to receive new trigger actions, however, the number of such actions

(input triggers) was accumulated separately for each individual trigger, including the time when it was blocked. In addition, in each recorded event, there was information about all the trigger sets that triggered.

For some triggers a prescaling procedure was used, that is, only each n-th event (with a fixed n) was selected for registration. Such suppression changed the influence of the system deadtime on events with this trigger. In this case the individual count of the input and output triggering made it possible to evaluate the deadtime factors, that is, the efficiency of the data collection system, for each trigger.

The following trigger circuits were used in the discussed experiments:

— FdAnd: a single-particle FD trigger, requires the action of at least one counter in each of the hodoscope walls;

— FdDouble: a trigger for two particles in the FD, requires in each of the hodoscope wall either two counters triggering, or exceeding the threshold of double ionization energy loss for the proton;

— PdDirect: a single-particle PD trigger of coincidence of any PD start counter with any of the stop, including the sidewall;

— PdTripple: a trigger for two particles in the PD, which requires the action of a combination of counters, either (1 start + 2 stop), or (1 stop + 2 start);

— Fd&Pd: FdAnd coincides with the PD sidewall counter;

— HighThreshold: a trigger for high ionization loss in the first FD wall hodoscope and the PD sidewall, requiring a loss threshold exceeding in at least one counter;

— STT_Or: a trigger by signal from any of the first two STT layers.

FdDouble, PdTripple, and Fd&Pd were the main triggers for proton pairs registration in the FD and PD. The schemes of the FdAnd and FdDouble triggers are given in [74].

2.3.2 Measurement with a proton beam

In the experiment conducted in 2009 a vertically polarized proton beam with kinetic energy of 353 MeV circulated. The direction of polarizations varied each accelerator cy-

cle (6 minutes). In the $\vec{p}\,d \to \{pp\}_s\pi^- + p_{\text{spec}}$ reaction fast protons from the pair $\{pp\}_s$, obtained by interaction of the beam with a deuterium cluster target, were registered in the FD and PD. Pions produced at small angels in the center of mass system were registered in the ND, slow spectator protons p_{spec} in the STT.

In this measurement, all of the following triggers were used. FdAnd was prescaled 2 to 6 times (the factor varied depending on the load). It was used for calibration, normalization and also for evaluation of the FdDouble and HighThreshold triggers efficiency. For a small part of the data being taken for STT calibration, FdAnd was replaced by the STT_Or trigger. PdDirect was used at the beginning of the beam-time to configure and test the PdTripple trigger efficiency.

2.3.3 Measurement with a deuteron beam

The experiment with double polarization was carried out in 2011 using a vertically polarized deuteron beam (the polarization was switched every 10 minutes) and a polarized hydrogen target with a storage cell (the polarization direction changed every 5 seconds). The deuteron beam energy was 726 MeV.

At this measurement all the described triggers were used, except for the STT_Or. The FdAnd trigger was prescaled 20 times, PdDirect – 16 times, and HighThreshold – twice. All the proton pairs from the $\vec{d}\,\vec{p} \to \{pp\}_s\pi^- + p_{\text{spec}}$ process were registered in the PD with the PdTripple trigger. The spectator protons carried half of the beam momentum this time, and thus fell into the FD. The FdDouble trigger was used to the calibration process $dp \to d\pi^0 + p_{\text{spec}}$registration, in which both charged particles fell into the FD.

Chapter 3

Experimental data analysis

This chapter describes the procedures for the experimental data processing. They include methods of calibration, events reconstruction and efficiency determination common to all measurements on ANKE, as well as the procedures that were used in the study of the processes $\vec{p}n \to \{pp\}_s\pi^-$and $\vec{n}\,\vec{p} \to \{pp\}_s\pi^-$.

3.1 General analysis and calibrations procedures

3.1.1 Particle trajectories and momenta reconstruction

The information from the multiwire proportional (MWPC) and drift (MWDC) chambers is used for the particle track reconstruction in the FD, PD and ND. The chambers are located in the scattered field of the D2 magnet region which leads only to a slight deviation from a straight line for tracks. This allows us to use a simple straight track model in the detector area. Multiple Coulomb scattering also has no significant effect on the particle trajectory between the chambers and is taken into account by the corresponding differences in the tracks identification procedure.

In general, the tracks multiplicity in each detector in the experiments with a cluster and a polarized target is very small: one-track events rate to more than 99.5% except for the case of the FD in the deuteron beam measurements when two particles are recorded in about 5% cases of all events. However, in the processes $\vec{p}n \to \{pp\}_s\pi^-$and

$\vec{n}\,\vec{p} \to \{pp\}_s\pi^-$, proton pairs with low excitation energy E_{pp} most often fall into one detector and thus the special attention was paid to the effective reconstruction of such events.

The track reconstruction procedure in the FD is described in details in Ref. [73]. The presence of vertical, horizontal and inclined wires (strips) allows to reconstruct multiple track events in the chambers, that is necessary for the study of diproton reactions. The size of the wire cluster in MWPC is very small, one wire acts in more than 90% of cases, which allows to exclude the usage of the same cluster in several tracks. A significant efficiency loss in the reconstruction of proton pairs is observed only for $E_{pp} < 0.3$ MeV. It is connected mainly with the MWDC pitch as well as with the requirement of two particles to fall into different hodoscope counters in at least one of its walls, which is necessary for identifying particles by the time-of-flight (TOF) difference.

The task of the tracks search for one-track processes in the PD and ND is simple enough and is carried out by "standard" searching procedures that are used in all ANKE experiments. However, the "standard" procedure did not provide required efficiency of the two-track events reconstruction. Thus, a special search algorithm was created. The typical cluster size in the PD is 3-5 wires depending on a proton track angle and momentum and, as a wires pitch is 2.54 mm, it leads to a cluster width of $\sim$ 1 cm. Furthermore, proton momenta recorded in the PD is much lower than in the FD and, with an equal value of E_{pp}, the distance between tracks of a proton pair is larger in the case of registration in the PD. This allows to reconstruct the pairs with low excitation energy E_{pp} efficiently even with a large size of wire clusters. As in the case of FD, the main restriction on the minimum value of the E_{pp} here is also related to the requirement that two protons hit different counters of the start or stop counters groups.

The ND was used only for π^- detection in the measurement with a proton beam which did not require the development of a special search procedure aimed at multiple events.

Having obtained tracks coordinates one can estimate kinematic parameters of the particles. The magnetic field of the spectrometer magnet D2 is known on a three-

dimensional lattice, which makes it possible to determine the three-component momenta at the reaction vertex, fixing the latter.

Several methods of the momenta reconstruction were used: the box-field approximation, the polynomial approximation, the Runge-Kutta method.

The box–field approximation has been used for the fast preselection of raw data in the PD and ND. For this procedure the magnetic field of the magnet D2 is considered as a homogenous box-field with an effective field width and length. Inside the magnetic field the charged particle moves circular, outside the field a straight line is assumed. Then components of the particle momentum are calculated, taking into account the vertical and horizontal coordinates and angles derived from the chamber information.

In the polynomial method [73], each of the momentum component was approximated by a polynomial of the third degree of the four track parameters (track coordinates and angles in the horizontal and vertical planes). The polynomial coefficients are found from typical samples of events produced by GEANT-simulation. This method was used for the momenta reconstruction in the FD.

The fourth-order Runge-Kutta method was used for the final analysis of data from all detectors. Fit parameters, three-component momentum $\vec{P}$ and vertical coordinate of the vertex Y_{target} are varied to obtain coordinates of the measured chambers after tracking, while the target X and Y coordinates are fixed. The widely used method of inverse tracking from the track on the cameras to the target was not applied due to trajectory curvature in the camera area, which was of little importance when searching for a track, but valuable for the momentum reconstruction. The initial parameters for the Runge–Kutta are taken from the box–field approximation and the polynomial method. The Runge-Kutta method tracking was also used when a vertex Z-coordinate was reconstructed in the measurement with a storage cell (see Sec. 3.5.3).

3.1.2 Momenta scale calibration

The technique for the geometrical parameters calibration on ANKE is described in [73]. The accuracy of the particle momentum and emission angle reconstruction is directly related to the accuracy of the ANKE geometry determination. The location

and size of the main parts of the spectrometer are well defined and fixed, but some parameters, that necessary for track reconstruction, must be known with accuracy inaccessible in a direct measurement. Thus, the camera position is measured with accuracy of at least 0.5 mm which, however, exceeds the coordinate resolution (RMS) of the FD cameras which makes the main contribution to the momenta resolution $\delta p/p \approx 1\%$. This makes the X-coordinate of the cameras the most sensitive positional parameter. One more of these parameters is the X-coordinate of the intersection point of the beam with the target. Another important parameter is the beam deflection angle from the nominal COSY orbit which may differ from the expected one due to the shift of the synchrotron orbit. The uncertainties of these parameters influence the value of the reconstructed particle momentum, and hence the resulting missing mass in the reaction.

To ensure the correct momentum reconstruction, it is necessary to calibrate the geometry with kinematics of exclusively registered processes. In the case of a proton beam and a deuterium target, such processes, with all particles recorded or only one particle not recorded, are $pd \to pd$, $pd \to dn\pi^+$, $pd \to ppn$, $pd \to {}^3H\pi^+$. In the inverse dp-kinematics a process $dp \to dp\pi^0$ is added to them, and in the elastic dp-scattering both secondary particles in the FD can be detected.

During the calibration procedure the parameters are varied and tracks are reconstructed anew at each iteration . At the same time, the missing mass deviations from the nominal value for the reaction are minimized. The processes with all final particles recorded are included in the general χ^2-functional through the deviations of all 4-momentum components. They play a special role, since they are most sensitive to the particle transverse momentum shift.

The calibration procedure is especially important in the case of FD where the influence of track positions on reconstructed momenta is the greatest.

3.1.3 Scintillation counters delay adjustment

The difference in the particles TOF from the target to the counters serves as the main criteria for identification two or more particles in the FD, PD and ND. To determine this

difference it is necessary to know the relative delays between the scintillation counters. Such delays are determined for the counters of each detector separately, after that the total delay between the detectors is estimated.

FD delays

The hodoscope walls in the FD are close to each other (7 cm), so that the TOF for the particles can be assumed to be approximately the same, and the TOF difference between two walls for different particles can be neglected. Thus, the difference of signals from the counters located one after another, triggered by the same particle, directly yields a relative delay in this pair. The hodoscope walls are shifted by half a counter and each front wall counter corresponds to two on the back wall, and vice versa. This allows all counters to be linked through paired delays and, in the end, to determine delay for each counter with respect to the first one.

PD and ND delays

The start and stop counters in the PD are spread over a large distance and, for determining the relative delays, it is necessary to take into account the TOF between the counters for which it is necessary to reconstruct the momentum and identify the particle type. Pions and protons are in the majority of particles in the PD, and usually forming clearly separable peaks in the raw TOF spectra for each combination of start-stop counters, which is due to the limited momenta range of each stop counter with a width of ~ 30 MeV/c.

The delay between the i-th start and j-th stop counters is $\Delta_{ij} = \Delta_i^{Sa} - \Delta_j^{So}$, where the delays for each counter Δ_i^{Sa} and Δ_j^{So} are defined relative to the one of PD counters. By minimizing the following form:

$$\chi^2 = \sum \frac{(T_i - T_j + \Delta_i^{Sa} - \Delta_j^{So} - \tau_{ij})^2}{\sigma^2},$$

one can define the delays for all PD counters with respect to the selected one. Here T_j and T_j denotes the time measured in the i-th start and j-th stop counters, and τ_{ij} is the TOF between start and stop counters calculated using the reconstructed

momentum and with a certain type of particle assumed. Summation is carried out for all combinations of start and stop counters falling within the acceptance region of the PD detector. Since the χ^2 form is linear over the parameters Δ, the minimization process is equivalent to solving a system of linear equations with respect to the delays of all the counters considered.

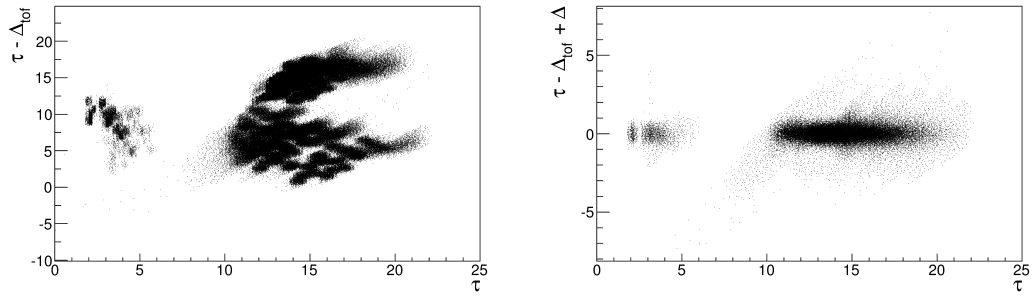

(a) Before delay corrections

(b) After delay corrections

Figure 3.1: The difference between the calculated TOF between the start and stop counters and the raw measured TOF without and with the delay corrections, as a function of the calculated TOF.

Pions or protons did not fall into some start-stop combinations acceptance, in addition, data obtained with a storage cell contained a significant background of scattered protons with momenta that did not correspond to their stop counters. In this case, for the particles identification, the energy loss spectra in the stop counters were built, depending on the difference in the TOFs for each counters combination, as shown in Fig.3.2. On these spectra one can see a compact group of the fastest particles, these are pions, and a continuous line of protons, which includes scattered protons, as well as protons coming from the target. Relative positions of the peaks could be found using model spectra from the GEANT simulation.

When solving the system of equations, the useful events were selected within 2σ region of identified peaks of pions and protons found in the TOF spectra. Fig. 3.1 shows the difference between the measured and calculated TOF before and after the delays correction was applied.

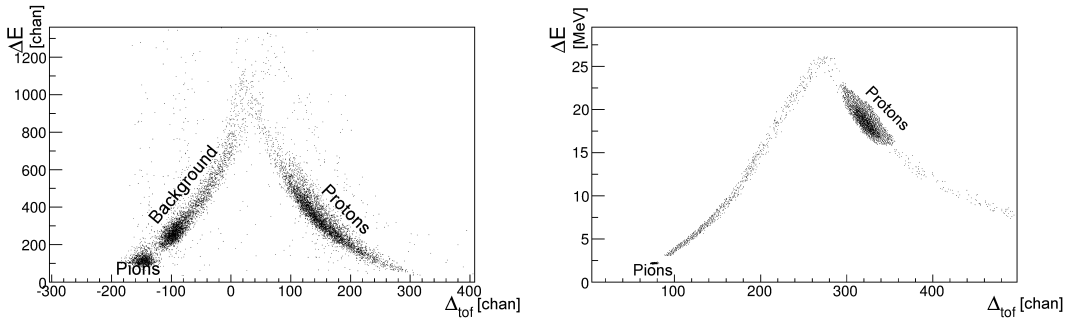

(a) Experimental spectrum

(b) Simulated spectrum

Figure 3.2: Energy losses in the stop counter versus the TOF between the #4 start counter and the #3 stop counter. The groups of pions and protons born in the target are labeled, as well as the group of background protons with large momenta.

3.2 Efficiency of events registration and reconstruction

3.2.1 Efficiency of multiwire chambers and scintillation counters

Counter efficiency

Scintillation counters were used for trigger generations, for the track search and particles identification. The main inefficiency originated from the amplitude drop at the upper (Q_{up}) or lower (Q_{down}) photomultiplier (PMT) below the time signal generation threshold. The possibility of this was checked by the distribution of the amplitudes Q_{up} and Q_{down} as a function of distance from tracks to PMTs (vertical track coordinates): the amplitudes are minimal at the maximum distance from the PMT. Events close to the sought secondary particles (protons from diproton pairs, or spectator protons in the FD and PD, π^- in the ND) were selected according to the particles types and momenta. Signs of inefficiency were detected only in the thin FD counters, nearest to the beam, which, however, were not used at this analysis.

In the case of FD, the gap between the counters of each of the hodoscope walls could also serve as a source of inefficiency. Chances of this were studied earlier in the report [75], where it was shown that the inefficiency of each hodoscope wall does not exceed $1,6\%$, and most of the failures occur in counter edges or gaps between them. In this report, the second wall studied did not participate in the trigger formation and the

track search, and its efficiency could be estimated. This estimate was used as a general factor for the correction of the hodoscope inefficiency.

Camera efficiency

The coordinate information excessiveness in the FD allows to determine the efficiency of the cameras, excluding certain cameras (planes) from the track search, and scanning these planes with the tracks reconstructed in such a manner. In practice, either all the first of the double (X, Y) MWPC planes were used, or all the second planes, and the drift chamber did not participate in the construction of the test tracks. Only events with one cluster on each of the track planes were used to build test tracks.

For each chamber plane, an efficiency map was constructed, and the correction factor was calculated for each event using the efficiency value at the map cell intersected with the track. The sensitive area of the plane was divided into 20×20 cells (2 to 3 cm each), and the efficiency was calculated for each of the cells.

The efficiency maps for each plane were calculated for all runs and were checked for stability over time. In the measurements described, all FD wire planes showed an efficiency $\varepsilon \geq 99\%$, while the strip efficiency was lower ($\varepsilon \geq 90\%$).

In the case of PD and ND the chambers scanning was carried out using passages, built by the start and stop counters tripped. The efficiency for proton events was higher than for pion ones. The total track efficiency with the requirement of triggering of two out of the three wire planes in each of the PD MWPC was 99% for protons and 95.4% for pions.

The cameras efficiencies were also determined in the real time during the data collection, which allowed choosing the optimum values of voltage and thresholds, as well as monitoring the correctness of the camera timing gate settings.

3.2.2 Trigger efficiency

A set of used triggers is given in Sec. 2.3. The efficiency of the single-particle triggers depends only on the counter efficiencies discussed above, and does not require special verification.

The efficiency of the two-particle FD trigger (FdDouble) was tested at events recorded with the single-particle FD trigger. From these events, proton pairs of the process $pn \to \{pp\}_s\pi^-$with low relative energies were selected in the presence of FdDouble. The efficiency of FdDouble was defined to be not less than 98% for both measurements, as with the proton, and with the deuteron beams.

The situation with the two-particle PD trigger (PdTripple) turned out to be more complicated. The efficiency of this trigger was defined from the events recorded with the single-particle PD trigger (PdDirect). Here events were searched with the combinations (1 stop + 2 starts) or (1 start + 2 stops) of triggering counters, which were included in the PdTripple circuit and with the difference of response times in the expected for diprotons range. For such events, triggering of PdTripple was checked. As it turned out, at the beginning of the measurement with the proton beam, PdTripple was almost completely ineffective. The trigger circuit was changed significantly, after which the efficiency estimation was $> 99\%$, and it remains at this level in the measurement with the deuteron beam.

A fortunate circumstance was that the thresholds of the high energy loss trigger in the PD side wall (HighThreshold) during the PdTripple inefficiency period turned out to be low enough to register 95% of the protons from the $pn \to \{pp\}_s\pi^-$process, which allowed not to lose statistics in this part of the beam time.

3.2.3 Deadtime of the DAQ correction

The loss of events due to the deadtime of the data acquisition system (DAQ) depends on the detector loads and, therefore, may change with time. Due to the asymmetric acceptance of the detectors, the load, and hence the deadtime factor, will also depend on the direction of the beam and target polarization vectors. The suppression usage, that is, the selection only each n-th event for recording, also changes the time distribution between the selected events from $P(1)$ to $P(n)$, where P is the Poisson distribution probability for the 1st and n-th events in this time interval, which also changes the deadtime factor. When using different factors of suppression for different triggers, it is necessary to determine its correction for each of them.

There is information about all triggers acted for each event in the ANKE data collection system, and the number of input triggers (T_{in}) is counted for each of these events. It is important to note that the input triggers are not blocked when reading information from "slow" cameras or a vertex detector, and the deadtime for the input triggers is negligible under our conditions. In such situation the deadtime correction can be defined as $R_{dt} = T_{out}/T_{in}$, where T_{out} is the number of events recorded by this trigger. This value is determined for each run, trigger, and beam and target polarization, and is used as the weight for a specific event.

3.2.4 Track search efficiency

The procedure for the track reconstruction efficiency estimation was developed for the FD when studying the process $pd \to \{pp\}_s n$ [57]. This procedure included the GEANT simulation of the facility, taking into account the non-point interaction between the beam and target and Coulomb scattering, as well as dispersion of the hits in the wire chambers according to the experimental clusters distribution. Additionally, the efficiency maps of sensitive planes of the cameras obtained from the data were used (see Sec. 3.2.1). Camera noise events were also copied into model hits from randomly selected experimental events. The resulting set of hits was sent on the input of the same tracks search procedure, which was used in the experimental data analysis.

Since the efficiency of the search of pairs with low E_{pp} depends on the kinematic parameters, firstly on the E_{pp} value itself, the efficiency evaluation was included in the general procedure for calculating the acceptance, thus, providing a complete simulation of the detection and reconstruction processes for each event. This procedure was also used to calculate the acceptance of the $pn \to \{pp\}_s \pi^-$process. Considered separately from the other factors, the average value of the track search efficiency for two-track events was $\sim 90\%$. A similar procedure was applied to events with one track in the FD, and showed the search efficiency of 99.5%.

3.2.5 Vertex detector STT efficiency

The main sources of STT inefficiency are non-working strips and low energy loss of particles in one of the STT layers. The first reason is related to the operation of reading electronics and can be taken into account when calculating the geometrical acceptance, while the second one affects the choice of the particle energy range used. The energy loss thresholds, used for the track reconstruction, were determined at the level $\Delta E = 0.3$ MeV for reasons of cutting of electronic noises and soft background particles, and they exceeded the electronic thresholds used.

The vertex detector was used in the measurement with the proton beam to detect slow spectator protons. The proton energy had the upper-limit with the region of applicability of the spectator mechanism $T_{\rm spec} < 6$ MeV ($P_{\rm spec} < 106$ MeV/c), and the lower-limit was built upon the requirement of the first layer passing $T_{\rm spec} > 2.5$ MeV, which was necessary for the $\delta E/E$ particle identification. If a particle was registered in the three layers of STT, it would be possible to determine the efficiency of each layer directly by excluding it from the track construction and checking for presence of trips in the corresponding strips. In our case all the protons of the required energies were stopped in the second layer of the STT (the minimum energy of the protons passing to the third layer was ~ 7 MeV) and there was no such opportunity, the third STT layer was disconnected during the measurement. However, the energy loss of the protons of our interest in the first layer was in the range of $\Delta E_1 = (0.8-2.5)$ MeV, which exceeded the required threshold significantly. In the second layer the range was of $\Delta E_2 = (0.6-5)$ MeV, and the presence of the lower-limit is due the Bragg peak of energy release for the protons stopped in the first layer. Thus, small energy release could not be a source of inefficiency in this experiment.

A direct study of the STT efficiency using particles falling into the third layer was performed on the other ANKE data and showed a high detector efficiency of $\varepsilon \geq 99\%$.

3.3 Particle type identification

3.3.1 Particle identification by the TOF

When two or more particles are detected in the FD, PD and ND, the difference in their measured arrival times in the scintillator counter can be used to determine a particle type. In the case of the production of these particles in the same interaction and from the one vertex, this difference is equal to the difference of particle TOF from the target to the counters Δ_{tof}.

On the other hand, assuming certain masses of particles from the pair, the difference of the TOF $\Delta\tau(p_1, p_2)$ can be calculated taking into account the reconstructed momenta and trajectory lengths. Then, on the plot, pictured the measured versus calculated TOF differences, the events for which the assumed masses turned out to be correct are located on the diagonal.

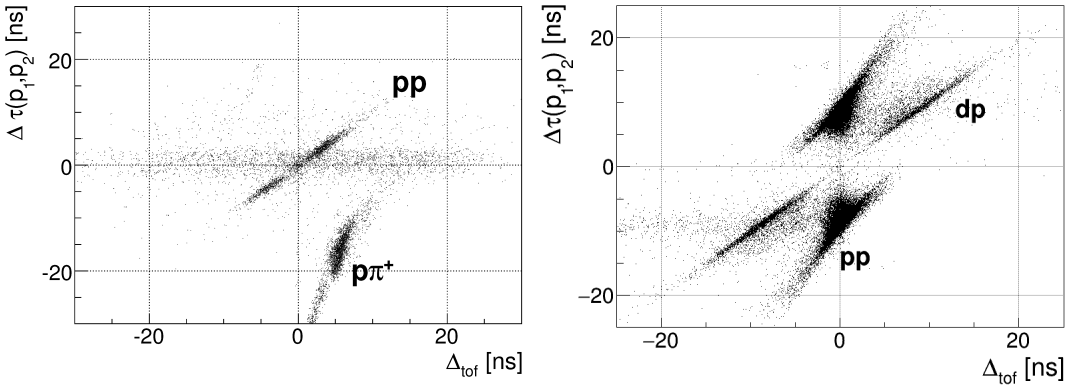

(a) Two protons in the PD.

(b) A proton and a deuteron in the FD.

Figure 3.3: Measured TOF difference for two particles Δ_{tof} versus calculated TOF $\Delta\tau(p_1, p_2)$.

Fig. 3.3a shows the proton beam experiment events, for which the tracks are reconstructed in the PD and $\Delta\tau(p_1, p_2)$ is calculated under assumption that both detected particles are protons. Proton pairs form a diagonal on the figure. The resolution for the pairs registered in both FD and PD was $\sigma(\Delta\tau(p_1, p_2) - \Delta_{tof}) = 0.6$ ns and is determined mainly by the momenta resolution.

The identification of the process $dp \to d\pi^0 + p_{\text{spec}}$in the experiment with a deuteron beam was carried out in a similar way. The distributions were constructed for events

with two tracks in the FD, assuming that the detected particles are a proton and a deuteron, as shown in Fig. 3.3b. The resolution in this case was $\sigma(\Delta\tau(p_1, p_2) - \Delta_{tof}) = 0.33$ ns.

3.3.2 Particles identification by the energy losses in the scintillator counters

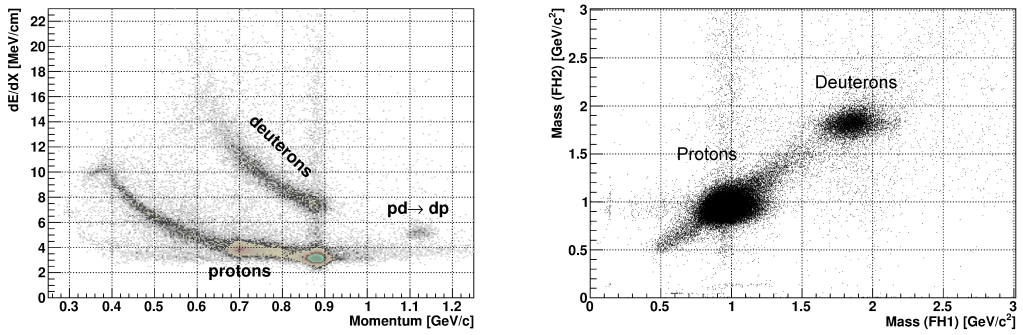

(a) Energy losses as a function of momentum.

(b) Particle mass reconstructed by energy loss in the first wall of the hodoscope versus the mass obtained from energy loss in the second wall.

Figure 3.4: Particles identification by ionization losses in the FD hodoscope.

In the proton beam experiment only the secondary deuteron from the normalizing process $pd \to d\pi^0 + p_{\text{spec}}$ was detected in the FD, which means that the TOF identification method was inapplicable. In this case, the particle type was defined from the ionization losses in the FD hodoscope. The calibration procedure of the energy losses is described in Ref. [72]. Fig. 3.4a shows the dependence of the measured energy losses versus the particle momentum. The lines of protons and deuterons are clearly distinguishable, the latter also includes deuterons from elastic backward pd scattering.

With the momentum and energy loss known, it is possible to calculate the particle mass, as shown in Fig. 3.4b, where the masses obtained from the energy losses in the first and second walls are compared. The protons and deuteron groups are clearly separated.

3.3.3 Particles identification in STT

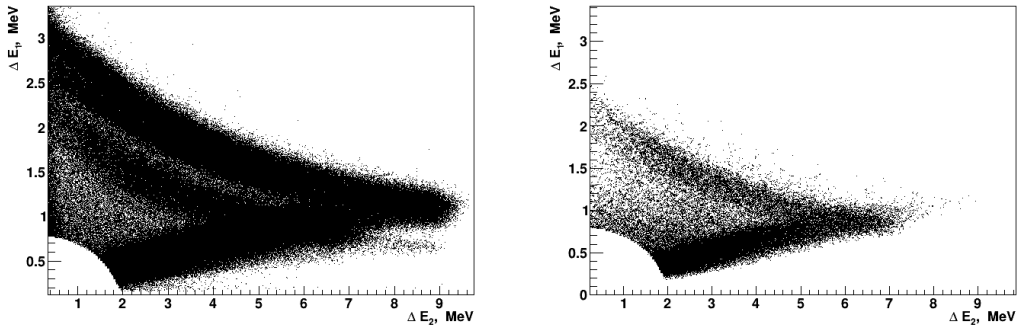

(a) Left telescope. (b) Right telescope.

Figure 3.5: Energy losses in the first and second STT layers.

The determination of a particle type in the vertex detector is possible on the basis of ionization energy losses for the particles stopped in the second or third layer. Fig. 3.5 shows the energy losses for protons and deuterons in the first and second STT layers in the measurement with the proton beam and the deuterium target. The two upper downward lines correspond to the protons and deuterons stopped in the second layer, and the lower upward line to the particles that passed through the second layer. As can be seen, identification is possible only in a limited energy interval. Deuterons are observed only in the left telescope in this measurement, since events were obtained with the FD trigger, and most deuterons belong to the elastic *pd* scattering, which does not fall into the right telescope in coincidence with the FD trigger. In the case of proton pairs in the FD or PD selection, the deuteron branch in the left telescope also turns out to be suppressed significantly.

3.4 Analysis of the proton beam data

For this experiment a vertically polarized proton beam and a deuterium cluster target were used. The beam ($\sigma = 3 - 5$ mm) and the deuterium jet ($\oslash = 1$ cm) dimensions did not bring in significant uncertainty into the reconstructed kinematical

parameters and the interaction region was considered as pointlike in the horizontal projection.

The task of the experiment was to obtain the differential cross section and the vector analyzing power of the process $\vec{p}n \to \{pp\}_s\pi^-$, which required the absolute luminosity as well as beam polarization determination. In order to do this, it was necessary to determine the ratio of the luminosities obtained with the different directions of the beam polarization vectors.

3.4.1 Processes identification and kinematical cuts

The process $pn \to \{pp\}_s\pi^-$

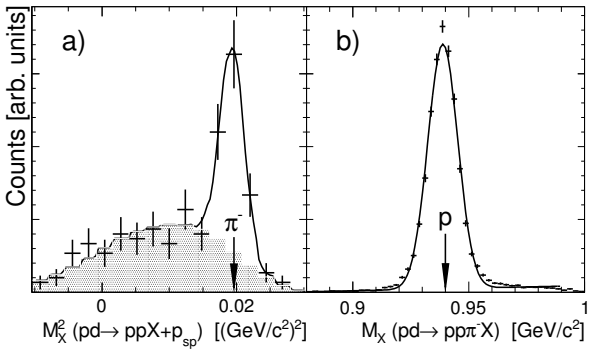

Figure 3.6: Kinematical identification of the process $pd \to \{pp\}_s\pi^- + p_{\rm spec}$. (a) The case of the registration of a spectator proton in the STT. The experimental spectrum (histogram with error bars), the background histogram (shaded area) and the sum of the background with the Gaussian describing the π^- peak (solid line) are shown. (B) The case of π^- in the ND registration. The curve is the result of the fit with the Gaussian and linear background.

For the selection of the $pd \to \{pp\}_s\pi^- + p_{\rm spec}$process proton pairs $\{pp\}_s$ were detected in the front and side detectors, in addition to that it was necessary to detect either $\pi-$ in the ND or spectator proton $p_{\rm spec}$ in the STT. Thus, the complete kinematics of each event was reconstructed. The types of the detected particles were determined by the TOF difference or by the energy losses in the STT.

As shown in Fig. 3.3a, the proton pairs are reliably separated from other pairs of particles and the only background source for the diproton selection is accidental

coincidences which contribution does not exceed 7%. The excitation energy of the proton pairs (diproton) was constrained to $E_{pp} < 3$ MeV, which was possible due to a good resolution $\sigma(E_{pp}) < 0.6$ MeV in this range of the E_{pp}.

The process $pd \to \{pp\}_s\pi^- + p_{\rm spec}$ identification was based on the missing mass of the reaction. Typical missing mass spectra for two cases are shown in Fig. 3.6, such spectra were built for each angle θ_π^{cm} and ϕ_π^{cm} bin and for both beam polarization vector directions. The background level in the case of π^- detection was low $(5-8\%)$, which allowed to use a simple linear description for it. The significant level and complex shape, that is changing with an angle, in the case of the spectator proton detection, required a special procedure for this shape determination, described below in Sec. 3.4.2.

The energy of the spectator proton was limited to $T_{\rm spec} < 6$ MeV ($P_{\rm spec} < 106$ MeV/s) in order to select the quasi-free reaction $pn \to \{pp\}_s\pi^-$from missing mass peaks. In addition, the first layer of the STT was required when registering $p_{\rm spec}$, which led to the selection of events with $T_{\rm spec} > 2.5$ MeV, and in the case of the π^- registration the lower limit for the $T_{\rm spec}$ was not set.

The quasi-free pn-interaction energy depends on the energy and exit angle of the spectator proton, and an available range of the effective "free" beam energy in the experiment was $T_{\rm free} = (310-390)$ MeV. Here $T_{\rm free}$ is the beam energy of the free pn-interaction with the same total energy in the center of mass system as in the quasi-free one. This value was measured with accuracy of $\sigma(T_{\rm free}) = 2-4$ MeV, and only data in the range of $T_{\rm free} = 353 \pm 20$ MeV were used in the analysis .

The process $pn \to d\pi^0$

In the $pd \to d\pi^0 + p_{\rm spec}$ reaction, the final deuteron was detected in the FD and was identified by energy losses in the hodoscope, while the proton background admixture did not exceed 10%. The spectator proton was detected in the STT similar to the case of the $pd \to \{pp\}_s\pi^- + p_{\rm spec}$, and here the limit $T_{\rm spec} = (2.5-6)$ MeV was also applied. The process was identified by the missing mass equal to the π^0 mass. As in the case of the $pd \to \{pp\}_s\pi^- + p_{\rm spec}$, the background description for the missing mass spectra was a certain problem, and a procedure common to both reactions was used, see Sec. 3.4.2.

Additional constraints were applied on the proton exit angles to reduce the background of accidental coincidences: the azimuthal angle was chosen to be $\varphi = \pm 20^o$ in the left and $\varphi = 180 \pm 20^o$ in the right STT telescope. The process $pd \to d\pi^0 + p_{\text{spec}}$ was observed in the range of polar angles $\theta = 50 - 130^o$ in the left, and $\theta = 56 - 72^o$ in the right telescope, but in the latter case the range was narrowed to $\theta = 60 - 68^o$ to reduce the contribution of the elastic *pd*-scattering that gives a peak at $\sim 70^o$. The T_{free} distributions for the p_{spec} registration differ for the two telescopes, and the $T_{\text{free}} = 353 \pm 10$ MeV in the left telescope and $T_{\text{free}} = 370 \pm 10$ MeV in the right one were chosen for the analysis.

3.4.2 Background shape in the missing mass spectra

The time information from the STT was not used in the initial analysis, which led to fact that the main source of the background when registering the spectator proton in the processes $pd \to \{pp\}_s\pi^- + p_{\text{spec}}$ and $pd \to d\pi^0 + p_{\text{spec}}$was the accidental coincidences. To obtain the shape of this background, artificially constructed events were used in the missing mass spectra. For this, diprotons (or deuterons in the case of $pd \to d\pi^0 + p_{\text{spec}}$) were identified in the main part of the data, but without the requirement of coincidence with spectator protons. In this case, the signal in the STT was also not required in the trigger (see the list of triggers in Sec. 2.3). Information about the spectator proton was obtained from a random event taken from another part of the data with the STT trigger, and the other detectors were excluded (data for the STT calibration). The same restrictions as in the main analysis were applied on the particle in the STT, as well as on the designed "complete" event. The missing mass spectra obtained from such events described the background in the real mass spectra well, as demonstrated in Fig. 3.6a where the shaded area is formed by the constructed background events. This procedure was carried out for each missing mass spectrum.

3.4.3 Relative and absolute luminosities, beam polarization

The luminosity and beam polarization were determined by the data of the quasi-free process $\vec{p}n \to d\pi^0$. It follows from isotopic invariance that the cross section for this

process should be equal to the half of the cross section $pp \to d\pi^+$, and all the spin observables of these reactions coincide. The differential cross section and the analyzing power of the $pp \to d\pi^+$ at 353 MeV are described with good accuracy by the SAID phase analysis [76], which predictions coincide near 353 MeV with the available experimental data with an accuracy of 5% for the cross section and 6% for A_y^p.

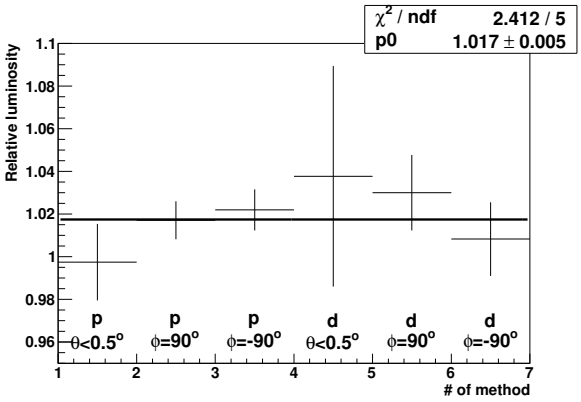

Figure 3.7: Relative luminosity determined for each group of normalizing events.

In order to determine luminosity and polarization one should find a ratio of the integral luminosities for different orientations of the beam polarization vector (relative luminosity). For this purpose, particles emitted at angles $\theta = 0$ and $\phi = \pm 90^0$ can be used, since for these angles the part of the cross section depending on the polarization is equal to 0. Protons and deuterons emitted at such angles were selected from the the single-particle FD trigger data (FdAnd) and the relative luminosity was calculated for each group of events, as shown in Fig. 3.7. The results for the groups coincide within the statistical errors, and the average result is $RL = L \downarrow / L \uparrow = 1.017 \pm 0.005$. This value also includes the DAQ deadtime correction for the FdAnd trigger.

In order to estimate detector acceptance, a complete GEANT-simulation of the ANKE was carried out. The acceptance of the reaction $pn \to \{pp\}_s\pi^-$ was calculated as a function of the pion exit angle θ_π^{cm} in the pn center of mass system, both for the cases of the spectator proton and the π^- detection. An isotropic distribution of the spectator exit angles was used and its energy was played out over the Fermi distribution [77]. A fast proton pair $\{pp\}_s$ was generated in the $^1S_0$ state with the excitation energy distribution in accordance with the Migdal-Watson factor for the S-wave interaction in

the final state taking into account the Coulomb interaction [59]. The efficiency for the two-track events search was also taken into account when calculating the acceptance.

To obtain luminosity, the number of events for the process $pn \to d\pi^0$ was determined in each bin over the polar angle of the deuteron emission θ_d^{cm} in the pn center of mass system, and the results with opposite directions of the beam polarization were summed taking into account the relative luminosity RL and the deadtime. Using the SAID calibration data [76], the integral luminosity was determined to be $L = (2312 \pm 110)\,\text{нб}^{-1}$, as shown in Fig. 3.8a. In this procedure, no correction for the shadowing in the deuteron was made since there is a similar effect in the process $pn \to \{pp\}_s\pi^-$.

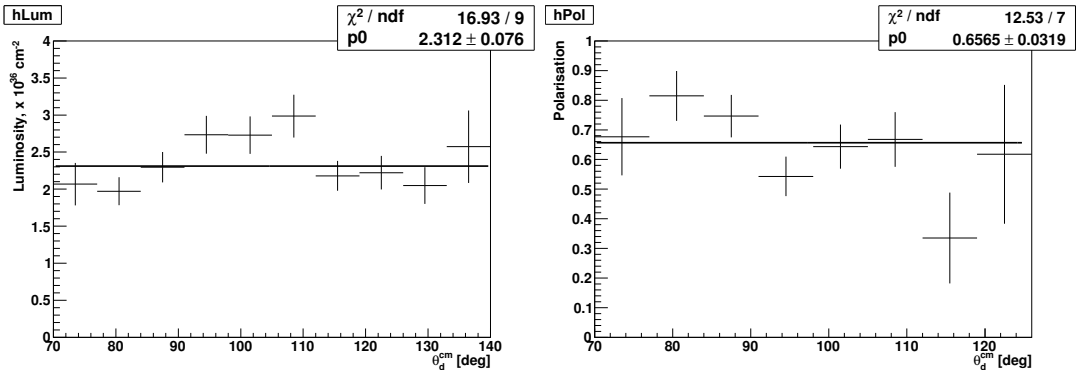

(a) Integral luminosity (b) Polarisation

Figure 3.8: Estimation of beam polarization and luminosity for different angles of deuteron emission. Only statistical errors are given.

An estimation of the beam polarization was obtained in each θ_d^{cm} bin as $P = \frac{\xi}{A_y^p \cdot <cos\phi>}$, where $\xi = \frac{N\uparrow \cdot RL - N\downarrow}{N\uparrow \cdot RL + N\downarrow}$ is the observed asymmetry corrected for the relative luminosity, and the value of A_y^p is taken from the SAID analysis. The values of $< \cos\phi >$ were calculated by filling the missing mass spectra with weights $\cos\phi_d$ and by carrying out the same procedure of the background subtraction. The angular distribution of the polarization is shown in Fig. 3.8b. It can be seen that the average value is determined by the angles close to 90^o, where the A_y^p is maximal. The resulting average value, taking into account the normalization error, was $P = 0.66 \pm 0.06$.

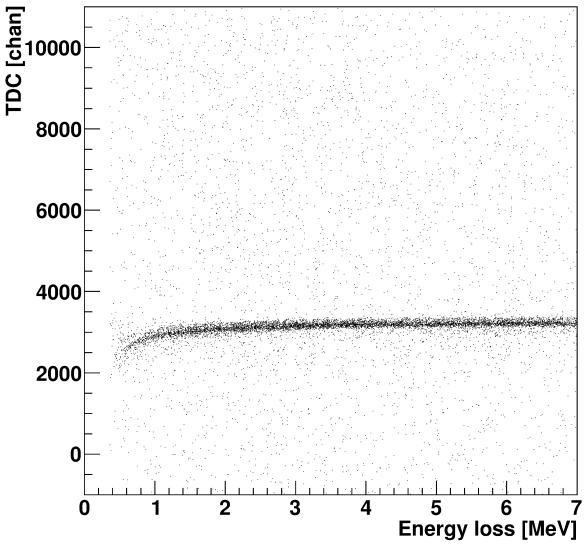

Figure 3.9: Time (in channels), measured in the second layer of the vertex detector STT, depending on energy release in this layer.

3.4.4 Reanalysis of the data using time STT information

The primal data analysis, described in Sec. 3.4.1-3.4.3 was carried out without using the time information from the vertex detector. The results of this analysis were included in Ref. [12] and were used for the first partial-wave analysis described in Sec. 4.3. Meanwhile, the main source of background in these data were accidental coincidences between fast proton pairs, or a deuteron recorded in the FD or PD and a spectator proton in the STT born in another pd collision. At the same time, the background level for the pion peak for the process $pd \to \{pp\}_s\pi^-$ reaches 50%.

Subsequently, a method to access the time information from the STT, obtained from vertical strips of each of the first two layers of each of the telescopes, was found. Fig. 3.9 shows the time measured in the second layer of the STT versus the energy release in this layer. Since the trigger and the time mark were obtained from the front or side detectors, the time in the STT reflects the time difference in the registration of fast particles in the FD or PD and slow spectator protons. Although the time resolution of the STT did not allow the refinement of the process kinematics, or even the particles identification, the time STT signal served as a powerful criterion for suppressing the

background of accidental coincidences. The time dependence versus the energy in the STT, shown in Fig. 3.9, is due to the use of a fixed threshold for the TDC signal.

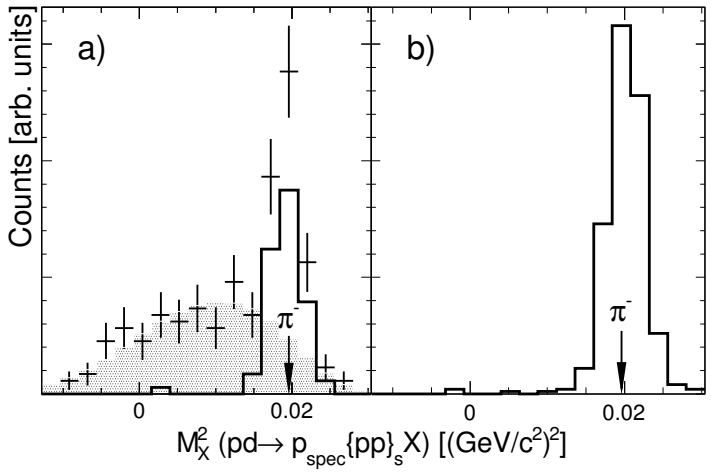

Figure 3.10: Missing mass squared for the $pd \to p_{spec}\{pp\}_s X$ reaction. (a) The spectrum measured using the first two layers of the STT, without selection by the time (points with error bars); constructed background (shaded area). The line marks the data obtained using the time information from the STT. (b) The spectrum for the same angular bin and the same detector combination obtained using the time information for protons stopped in the first STT layer.

A radical decrease in the background level of accidental coincidences by means of the time information from the STT is shown in Fig. 3.10. Such background suppression also allowed one to increase the statistics by considering also slower spectator protons $T_{\rm spec} < 2.5$ MeV that stopped in the first layer of the STT. This was possible since, at the beam energy of 353 MeV, the reaction $pd \to ppp\pi^-$ is the only process with three positively charged particles in the final state. Therefore, one can identify the reaction simply by making a missing-mass selection, without identifying explicitly the spectator proton from its energy loss. For such events, a second layer of the STT was used as a veto. The center of beam with target interaction region was considered as a starting point of the track, which defined the momentum direction. The accuracy of the measurement of the spectator three-momentum was poorer than in the case of a track construction using two layers of the STT, but still sufficient to identify the $pn \to \{pp\}_s\pi^-$ reaction from the pion missing mass. The background level makes

the events without the time information from the STT unusable. After applying this selection criterion, the background reduced to the few-percent level, as shown in Fig. 3.10b.

The expansion of the registered spectator proton energy range also led to an almost double refinement of the beam polarization, a new value of the beam polarization is $P = 63,3 \pm 3,6\%$. The reanalyzed results were used in the second partial-wave analysis described in Sec. 4.5.

3.5 Analysis of the deuteron beam data

In this measurement a vertically vector-polarized deuteron beam and an ANKE polarized hydrogen target, equipped with a storage cell (see Sec. 2.2.1) were used. The cell usage required a separate measurement of the background created by the cell, as described in Sec. 3.5.2. In addition, the cell length affected the reconstruction accuracy of the kinematic parameters. Therefore, the procedure for the interaction vertex reconstruction was developed (Sec. 3.5.3).

The purpose of the experiment was to measure the transverse spin-correlation coefficients $A_{x,x}$ and $A_{y,y}$ in the $\vec{n}\,\vec{p} \to \{pp\}_s\pi^-$ process, so it was necessary to determine the beam and target polarizations and the relative luminosities for different directions of the polarization vectors.

3.5.1 Process identification and kinematical cuts

The $dp \to \{pp\}_s\pi^- + p_{\rm spec}$ reaction was separated by a spectator proton registered in the FD and two protons in the PD. The spectator $p_{\rm spec}$, in contrast to the case with a deuterium target, carried away about a half of the beam momentum and exited at angles of about 0^o in the laboratory system, and the momentum of the protons from the pair $\{pp\}_s$ was a half of the spectator momentum. The pion π^- was not registered in this measurement.

In order to determine the particle type, the time-of-flight method was used. In this case, the differences in the TOF of $p_{\rm spec}$ with each of the $\{pp\}_s$ protons were analyzed.

In addition, each proton in the pair was identified by the TOF between the PD start and stop counters. Since protons were the bulk of the load of both PD and FD, the level of false identification of particles was negligible. The background of accidental coincidences, under a small load of the detectors and after the application of the time selection, also did not exceed several percent.

Diprotons, being $^1S_0$ states, were chosen among the selected proton pairs by the cut appliance on the diproton excitation energy of $\sigma(E_{pp}) < 0.6$ MeV. The resolution of $\sigma(E_{pp}) < 0.6$ MeV was the same as in the experiment with the proton beam.

In a similar way, proton-deuteron pairs were selected for the normalization process $dp \to d\pi^0 + p_{\rm spec}$, in which both deuteron and $p_{\rm spec}$ were detected in the FD. The particles identification by the difference in the TOF for this case is illustrated in Fig. 3.3b.

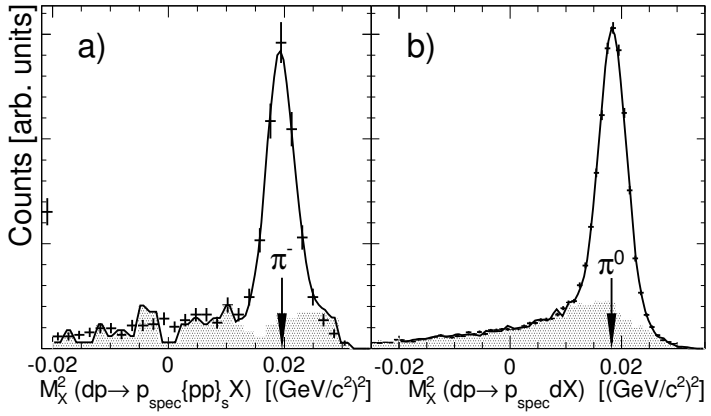

Figure 3.11: Missing mass squared for the processes (a) $\vec{d}\vec{p} \to p_{\rm spec}\{pp\}_s X$; (b) $\vec{d}\vec{p} \to dpX$.

Knowing the types of registered particles, the processes $dp \to \{pp\}_s\pi^- + p_{\rm spec}$ and $dp \to d\pi^0 + p_{\rm spec}$ can be selected by their missing mass, equal to the mass of pions m_{π^-}, m_{π^0}, respectively, as shown in Fig. 3.11. Here histograms with error bars represent the experimental data with a hydrogen target, the shaded histograms are the result of the background measurements described in Sec. 3.5.2, and the solid line is the fit of the hydrogen data with the sum of the background histogram and Gaussian.

As can be seen from the distribution of the kinetic energy of the spectator proton $T_{\rm spec}$ in the rest frame of the deuteron, the FD acceptance basically allows one to

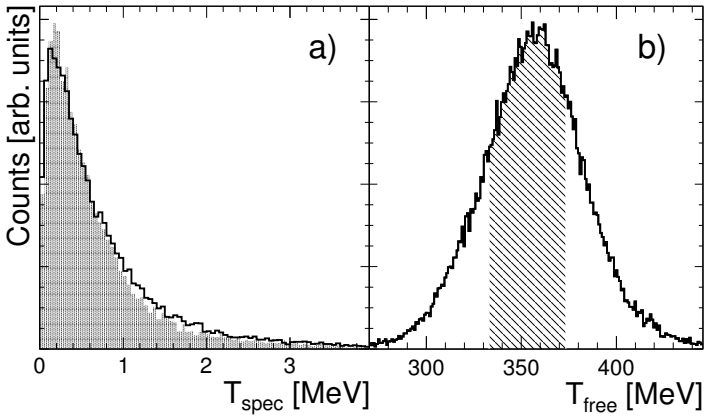

Figure 3.12: (a) Experimental (histogram) and simulated (shaded area) energy distribution of the spectator proton in the deuteron reference system from the reaction $\vec{d}\vec{p} \to \{pp\}_s\pi^- p_{\rm spec}$; (b) experimental distribution of the beam effective energy, the shaded area was chosen for the analysis.

detect protons with a small $T_{\rm spec}$ (Fig. 3.12a). To extract the quasi-free kinematics, the kinetic energy of the spectator protons was limited to $T_{\rm spec} < 6$ MeV. Knowing the spectator proton momentum, one can estimate the effective neutron energy in the reaction $np \to \{pp\}_s\pi^-$

$$T_{\rm free} = [s - (M_p + M_n)^2]/2M_p,$$

where $\sqrt{s}$ is the total energy in the center of mass system np, M_p and M_n are the proton and neutron masses, respectively. Fig. 3.12b shows the experimental energy distribution $T_{\rm free}$ and the limits $T_{\rm free} = 353 \pm 20$ MeV in which it was selected for the analysis. The cuts imposed on $T_{\rm spec}$ and $T_{\rm free}$ coincided with the limits in the experiment with the proton beam.

3.5.2 Shape of the background in the missing mass spectra

The reactions, similar to the dp-interaction processes under the consideration, also happened when the beam interacted with aluminum nuclei from the storage cell walls, which became the main source of an irremovable background in the experiment. The only visible difference between useful and background events was in the shape of the

missing mass spectra. To determine this shape, the separate measurements with an empty cell and also a cell filled with nitrogen were realized.

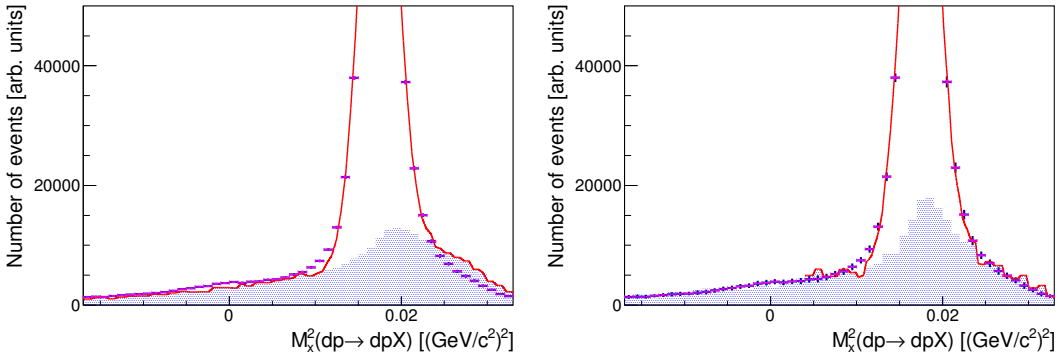

(a) Nitrogen target background (b) Empty cell background

Figure 3.13: Background subtraction in the case of the reaction $dp \rightarrow d\pi^0 + p_{\mathrm{spec}}$. The histogram with error bars represents the data from the hydrogen target, the shaded area is the scaled background, the red line shows the total fitted function.

In order to determine the amount and shape of the background under the peak from the hydrogen target, the studied processes were selected from the background data, and the missing mass spectra for each bin over polar θ and azimuth ϕ angles were put on the similar spectra for hydrogen events, as shown in Fig. 3.13. As can be seen from the figure, a more accurate description of the background was obtained with the empty cell data, so these data were used to subtract the background in the process $dp \rightarrow d\pi^0 + p_{\mathrm{spec}}$. However, the statistics obtained for the cell with nitrogen was significantly higher than the statistics on the empty cell, which turned out to be insufficient for the case of the process $dp \rightarrow \{pp\}_s\pi^- + p_{\mathrm{spec}}$. Here the difference in the distributions with the nitrogen and empty cell did not exceed the statistical errors, and the nitrogen data were used for the background subtraction.

When fitting the hydrogen data distribution, the sum of the scaled histogram of the background events and the Gaussian was used. The data error for each bin was determined from the squared sum of the statistical errors for the main and background data, taking into account the scaling.

The problem of the estimation of the background contribution could be substantially simplified by assuming that the angular distributions of the background events are the

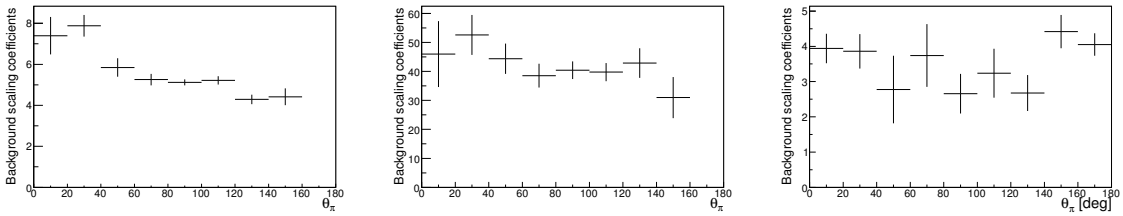

Figure 3.14: Background scaling factor depending on the θ angle for the $dp \to d\pi^0 + p_{\mathrm{spec}}$ reaction in (a) the nitrogen target, (b) the empty cell; (c) for the $dp \to \{pp\}_s\pi^- + p_{\mathrm{spec}}$ reaction in the nitrogen target.

same for the measurements with hydrogen, nitrogen and/or the empty cell. In this case, it would be possible to use a single background scaling factor. In order to test this assumptions, the independence of the fit parameter corresponding to the scale background factor from the scattering angle (Fig. 3.14) was investigated. As can be seen, this condition is not observed for the nitrogen coefficients of the reaction $dp \to d\pi^0 + p_{\mathrm{spec}}$. With regard to the remaining two spectra, it is hardly possible to make a definite conclusion because of too large statistical uncertainties. It should also be taken into account that such comparisons should be carried out separately for different ranges of the angle ϕ, which will additionally reduce the statistics. Therefore, in the further analysis, the individual values of the background level, that was determined for each angular bin, were used.

3.5.3 Vertex reconstruction

The measurements were carried out using the long storage cell with an asymmetric gas density distribution. Under these conditions, the determination of the interaction vertex allows: a) to reconstruct the kinematics of an event more accurately and reduce the width of the missing mass distribution; and b) to get rid of the data of the interactions of the beam with the gas in the target chamber but outside the storage cell.

The vertex reconstruction procedure involves the joint fit of the tracks and TOFs of all the registered particles. The reconstruction of the three-momentum of a particle

passing through the magnet D2 was based on the assumption that the (X, Z)-position of the interaction vertex is known. In the case of several tracks, along with the particle momenta, the longitudinal coordinate of the vertex Z can also become the fit parameter, while the transverse coordinate X is selected along the beam line according to the Z value. In addition, the reconstructed Y-coordinate of the interaction point becomes common for all tracks and is determined with better accuracy.

The accuracy of the Z-coordinate determination depends on the time measurement accuracy, the difference in the velocities of the particles included in the fit, and their momenta reconstruction accuracy. In our case, the limiting factor was the accuracy of the momenta measurement of the slowest particles — the protons from the final diproton in the reaction $dp \to \{pp\}_s\pi^- + p_{\rm spec}$ and the deuteron in the $dp \to d\pi^0 + p_{\rm spec}$.

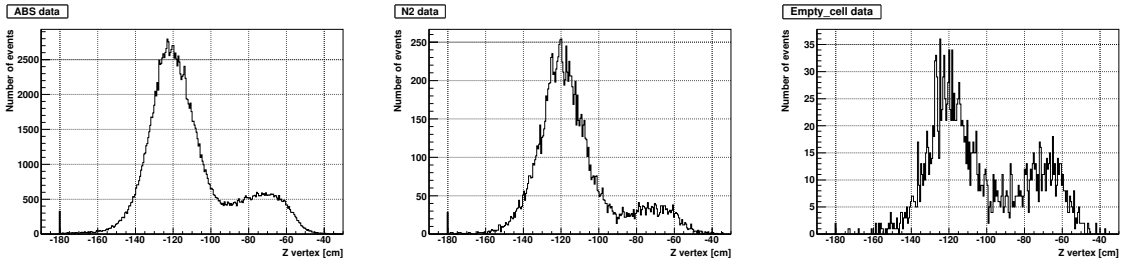

(a) Hydrogen target (b) N_2 in the target (c) Empty cell

Figure 3.15: Reconstructed vertex coordinate for the reaction $dp \to \{pp\}_s\pi^- + p_{\rm spec}$.

For the process $dp \to d\pi^0 + p_{\rm spec}$ with a deuteron registered in the FD, the simulation gives an error in the vertex determination of $\sigma(Z) \approx 12$ cm. This is too large to the vertex determination can improve significantly the reconstruction of the process kinematics, however, the procedure allows to get rid of the interactions with unpolarized gas outside the cell. For the process $dp \to \{pp\}_s\pi^- + p_{\rm spec}$, the simulation leads to the vertex coordinate accuracy equal to 5.6 cm, which significantly refines Z in comparison with the cell length of 37 cm.

The vertex reconstruction procedure was applied to the experimental data. The distribution of the obtained coordinate is shown in Fig. 3.15 for the data with a hydrogen target, a nitrogen target, and for an empty cell for the reaction $dp \to \{pp\}_s\pi^- + p_{\rm spec}$. The shape of all three distributions is similar, the peak is observed in the region of the

cell location $(-140; -100)$ cm, with a maximum near the entrance tube at $Z = -125$ cm. The events to the right of the peak ($Z > -100$ cm) are the result of the interaction of the beam with gas in the target chamber, and these events' number is explained, among other things, by increase of the acceptance of this reaction when approaching the magnet D2.

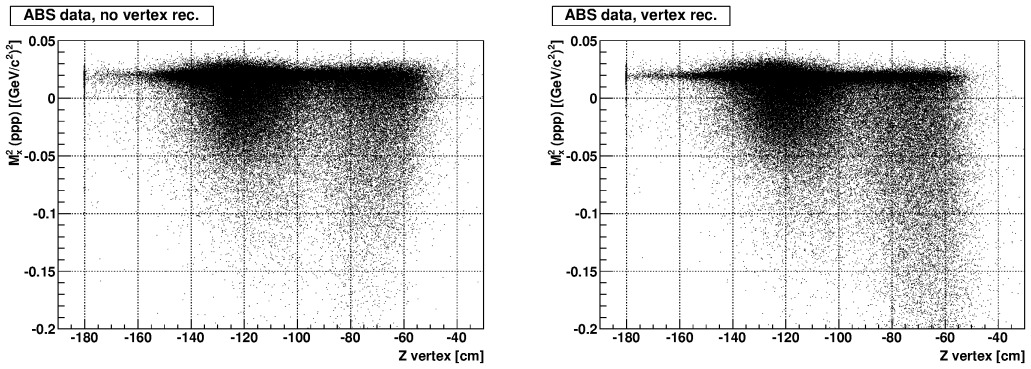

(a) Fixed interaction vertex

(b) With use of the reconstructed interaction vertex

Figure 3.16: Missing mass squared as a function of the Z-coordinate for the $dp \to \{pp\}_s\pi^- + p_{\text{spec}}$reaction.

One can follow up the influence of the interaction coordinate determination on the reconstruction of the reaction kinematics. Fig. 3.16 shows the results in the cases with the use the vertex reconstruction procedure and without it. Without reconstruction, the missing mass peak width increased as the vertex moved away the center of the cell ($Z = -125$ cm), used as the fixed coordinate of the vertex. In the case of the simultaneous reconstruction of the momentum and vertex, the width of the pion peak remains approximately constant along the entire region, including its part outside the cell.

The correct vertex coordinate implementation also affects the resolution in the TOF spectrum. In Fig. 3.17 the dependence of the discrepancy between the differences in the TOF, the calculated and measured $\Delta\tau - \Delta_{TOF}$, is shown for the cases with the fixed and reconstructed vertex.

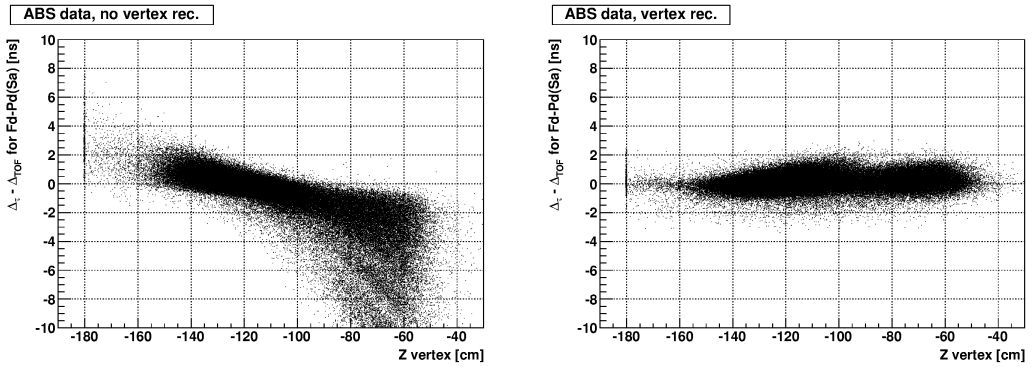

(a) Fixed interaction vertex

(b) With the use of the reconstructed interaction vertex

Figure 3.17: Discrepancy between the measured and calculated TOF differences as a function of Z-coordinates for the $dp \to \{pp\}_s\pi^- + p_{\rm spec}$ reaction.

3.5.4 Relative luminosity, beam and target polarization

As in the case of the proton beam (Sec. 3.4.3), the process $np \to d\pi^0$ was used for the polarimetry. Its analyzing power at 353 MeV is known from the SAID database [76].

The specificity of the measurement with a storage cell was the presence of the substantial background from its walls. For the exclusively selected processes this background could be subtracted from the hydrogen target signal in the missing mass spectrum. However, this was not possible for the particles emitted at the angles $\theta = 0$ and $\phi = \pm 90^0$ and selected without identification of the process, as was done for the cluster target data analyze. Therefore, the exclusive process $np \to d\pi^0$ was used, among other things, to determine relative luminosities. This was promoted with the large angular interval available for this process in the deuteron beam measurement $\theta_d^{cm} = 0 - 160^o$.

The bulk of the experimental statistics was obtained with the polarized beam and target. However, in order to study the polarization of the beam P and target Q separately, for a small part of the data an unpolarized beam or target were used. Also completely unpolarized data were obtained. Considering the acceptance of the reaction $np \to d\pi^0$ for these data sets to be the same, one could determine the polarizations for different directions of the beam and target polarization vectors independently.

Let's introduce the observed asymmetry, as

$$\xi = \frac{N\uparrow - N\downarrow}{N\uparrow + N\downarrow}$$

where $N\uparrow, N\downarrow$ are the rates with the beam polarization vector up and down, respectively. Then the polarization P is related to the observed asymmetry ξ as

$$\xi = PA_y^p\overline{\cos\phi},$$

where $\overline{\cos\phi}$ is the average of the acceptance in this bin over θ_d^{cm}. Asymmetries as regard to normalized unpolarized rates are equal

$$\begin{aligned}\xi_\uparrow &= \frac{N\uparrow - N_n}{2N_n} \\ \xi_\downarrow &= \frac{N_n - N\downarrow}{2N_n},\end{aligned}$$

where N_n are the rates for the unpolarized data set, corrected for the relative luminosity. The asymmetry associated with the target polarization is expressed by the similar formulas. The experimental asymmetries were constructed as the functions of the polar angle and fitted with the analyzing power function using the polarization and relative luminosity as parameters. The following results were obtained:
for the target (protons) $Q\uparrow = 59 \pm 7\%$ and $Q\downarrow = -70 \pm 11\%$,
for the beam (neutrons) $P\uparrow = 55 \pm 8\%$, $P\downarrow = -45 \pm 8\%$.

Within the error limits, the polarization values for the polarization vectors up and down are compatible and, as shown by the systematic error analysis in Appendix A.1, only a small additional error arises under the assumption of equal polarizations. The obtained neutron polarizations coincide with the accuracy of up to 10% with deuteron polarizations, which were measured at the injection at the beginning and end of the experiment (Chapter 2). It should be noted that the distribution of the gas density in the storage cell in the measurement with ABS was different from that for the unpolarized H_2 gas source, and the equality of the acceptances assumed here was not accurately observed.

However, the results obtained from the data part with the single polarization can not be considered final. It is necessary to extract time-averaged values for the polarizations

from the main set of the experimental data with the double polarization, since the polarization could vary during the course of the experiment, and, in addition, due to the difference in the acceptance of the process $np \to d\pi^0$ for polarized and unpolarized gas in the cell. The polarization determination directly from the data with the double polarization is also preferable because of much more statistics were obtained for this data.

In order to determine the beam and target polarization, one should know the integral luminosity ratios for each of the orientations of their polarizations. In our case, the polarized cross section is written as:

$$\frac{d\sigma}{d\Omega} = \left(\frac{d\sigma}{d\Omega}\right)_0 (1 + (PA_y^P + QA_y^Q)\cos\phi_\pi + PQ(A_{y,y}\cos^2\phi_\pi + A_{x,x}\sin^2\phi_\pi)),$$

where $\left(\frac{d\sigma}{d\Omega}\right)_0$ is the spin-averaged cross section, A_y^P and A_y^Q are the beam and target vector analyzing powers, and $A_{x,x}$ and $A_{y,y}$ are the spin-correlation coefficients of the process $np \to d\pi^0$. The polarizing effect in the cross section does not disappear at the forward direction, and in order to use such data to determine the relative luminosities, it is necessary to know not only the spin-correlation coefficients and the analyzing power for this reaction, but also the values of the still undetermined polarizations.

In order to separate the problems on the determination of the polarizations and relative luminosities, an iterative procedure was used. In the first approximation, the assumption was made that the integral luminosities are equal. Then, to determine the polarization of the beam (target), the states with different directions of the polarization vectors of the target (beam) could be averaged to obtain an unpolarized state. After using the transverse spin-correlation coefficients for the $pp \to d\pi^+$ reaction at 353 MeV and the defined polarization values, the following estimations were obtained for the luminosity ratios: $R\uparrow\downarrow = L\uparrow\downarrow / L\uparrow\uparrow = 0.97 \pm 0.02$, $R\downarrow\uparrow = L\downarrow\uparrow / L\uparrow\uparrow = 0.95 \pm 0.02$ and $R\downarrow\downarrow = L\downarrow\downarrow / L\uparrow\uparrow = 1.05 \pm 0.02$, $R\uparrow\uparrow = 1$.

Although the luminosity ratios, as expected, are close to one, the deviations from this are important in the extraction of the polarizations. After taking these deviations into account, for the average values of the beam and target polarizations one were obtained:

$| P | = 50 \pm 3\%(\text{stat}) \pm 3.5\%(\text{syst})$ and

$| Q | = 69 \pm 2\%(\text{stat}) \pm 3.5\%(\text{syst})$.

Chapter 4

Measurement results and partial-wave analysis

4.1 Relations for the observables and amplitudes of the process $pn \to \{pp\}_s\pi^-$

4.1.1 Polarization observables

In the reference frame, in which the beam is directed along the Z axis, and the Y axis is perpendicular to the reaction plane, the differential cross section for the considered reaction $pN \to \{pp\}_s\pi$ can be written as follows [78]:

$$\frac{d\sigma}{d\Omega} = \left(\frac{d\sigma}{d\Omega}\right)_0 [1 + P_y A_y^P + Q_y A_y^Q + P_y Q_y A_{y,y} + P_x Q_x A_{x,x} + P_z Q_z A_{z,z} + P_x Q_z A_{x,z} + P_z Q_x A_{z,x}], \quad (4.1)$$

where $\mathbf{P}$ and $\mathbf{Q}$ are the polarization vectors of the beam and target, and $(d\sigma/d\Omega)_0$ is the unpolarized cross section. The analyzing powers of the beam A_y^P and target A_y^Q, as well as the spin-correlation parameters A_{ij}, are the functions of the pion polar angle θ_π.

In the case when both the beam and the target are polarized perpendicular to the plane of the accelerator ring, with the polarization values P and Q, respectively, it is

convenient to rewrite the expression for this reference frame as follows:

$$\frac{d\sigma}{d\Omega} = \left(\frac{d\sigma}{d\Omega}\right)_0 [1 + (PA_y^P + QA_y^Q)\cos\phi_\pi + PQ(A_{y,y}\cos^2\phi_\pi + A_{x,x}\sin^2\phi_\pi)], \quad (4.2)$$

where ϕ_π is the azimuth angle of the pion emission in the laboratory reference frame.

However, in the quasi-free pn-collision, the direction of the incident particle momentum in the center of mass system of the reaction deviates from the accelerator beam axis. Similarly, the XY_{pn} plane does not coincide with the laboratory plane (see Appendix B.1). Then, the P and Q values in expression 4.2 correspond to the vector **P** and **Q** projections on the XY_{pn} plane of the quasi-free reaction (see Appendix B.1), and ϕ_π is the angle between the projection and the X_{pn} axis. We also neglect in 4.2 the small components P_z and Q_z, which arise in the quasi-free dimension. However, their contribution is included in the systematic errors in the analysis.

4.1.2 Spin and isospin amplitudes

The spin structures of the reactions $pp \to \{pp\}_s\pi^0$ and $pn \to \{pp\}_s\pi^-$ with the spin-singlet diproton in the final state are identical and in both cases is defined by the amplitude of the form $\frac{1}{2}^+\frac{1}{2}^+ \to 0^+0^-$. Because of the requirement of the parity and angular momentum conservation, the initial nucleon-nucleon pair must have a spin S = 1. Indeed, let L, S, respectively, to be the orbital angular momentum and the spin of the pair of nucleons in the initial state, and l_π is the orbital moment of the pion in the center of mass system of the reaction. Then, following from the P-parity conservation, L and l_π are opposite, and from the total angular momentum conservation one has $|l_\pi - S| \leq L \leq l_\pi + S$. These two requirements are compatible for $S = 1$ and are not compatible for $S = 0$.

In the considered reaction, there are only four possible transitions, which differ from each other by the spins projections of the initial nucleons, but because of the parity conservation, only two are the independent amplitudes. Regardless of the process dynamics, the transition operator can depend only on the momentum vectors of the initial proton **p** and final pion **k**, and the Pauli spin matrix σ, that is affecting the initial nucleon spin states. The Pauli matrix in the plates of the initial nucleons spin states

gives the polarization vector of the initial spin-triplet NN-state, which denoted here as **S**. Since the pion parity is negative, the transition amplitude of the considered reaction must be a pseudo-scalar, which is dictated by the requirement of parity conservation of the angular momentum. Using the three vectors **S**, **p** and **k**, one can construct, in the most general case, only one pseudo-scalar of the following form:

$$\mathcal{M} = \mathbf{S} \cdot (A\widehat{\mathbf{p}} + B\widehat{\mathbf{k}}) \,, \tag{4.3}$$

where A and B are the complex amplitudes (true scalars), determined by the process dynamics; $\widehat{\mathbf{p}}$ and $\widehat{\mathbf{k}}$ are the unit vectors in the center of mass system, directed along the momentum of the incident proton and the final pion, respectively. Note that a term of the form $[\widehat{\mathbf{p}} \times \widehat{\mathbf{k}}]\mathbf{S}$ is a true scalar and therefore is absent in (4.3) because of the requirement of the parity conservation.

The spin observables are expressed in terms of the scalar amplitudes A and B as follows [17]:

$$\begin{aligned}
\left(\frac{d\sigma}{d\Omega}\right)_0 &= \frac{k}{4p}(|A|^2 + |B|^2 + 2Re[AB^*]\cos\theta_\pi) \,, \\
A_{x,x}\left(\frac{d\sigma}{d\Omega}\right)_0 &= \frac{k}{4p}(|A|^2 + |B|^2\cos 2\theta_\pi + 2Re[AB^*]\cos\theta_\pi) \,, \\
A_{x,z}\left(\frac{d\sigma}{d\Omega}\right)_0 &= -\frac{k}{4p}(2|B|^2\sin\theta_\pi\cos\theta_\pi + 2Re[AB^*]\sin\theta_\pi) \,, \\
A_y^P\left(\frac{d\sigma}{d\Omega}\right)_0 &= \frac{k}{4p}(2Im[AB^*]\sin\theta_\pi) \,, \\
A_y^Q &= A_y^P \,, A_{y,y} = 1 \,, A_{z,z} = A_{x,x} \,, A_{z,x} = A_{x,z} \,.
\end{aligned} \tag{4.4}$$

These reactions are considered to be quasi-two-particle and, when estimating the kinematic factor k/p, a small range of the excitation energies of the diproton can be neglected. And, in case of the kinetic energy of 353 MeV, $p = 407$ MeV/c and $k \approx 94$ MeV/c.

Not all the observables 4.4 are independent. In particular, for any angles of the pion production, there is an equation [13]

$$(A_y)^2 + (A_{x,x})^2 + (A_{x,z})^2 = 1 \,. \tag{4.5}$$

This means that if two variables in this equation are measured, the third is determined within a sign of the given relation.

In addition to the total amplitude dependence on the spin, the amplitudes are subdivided into two isospins $M^{I=0}$ and $M^{I=1}$. At the same time, the amplitude $M(pp \to \{pp\}_s\pi^0)$ contains only the vector contribution $I = 1$, while the amplitude $M(np \to \{pp\}_s\pi^-)$ is a mixture of the isovector ($I = 1$) and isoscalar ($I = 0$) transitions: $M(pp \to \{pp\}_s\pi^0) = M^{I=1}$ and $M(np \to \{pp\}_s\pi^-) = (M^{I=1} + M^{I=0})/\sqrt{2}$. [1]

Since the initial nucleons are in epy spin-triplet state, the Pauli principle requires that $M^{I=1}$ to be antisymmetric with respect to the inversion operation $\mathbf{p} \to -\mathbf{p}$, and $M^{I=0}$ is symmetric. Taking into account the expression 4.3, these restrictions can be rewritten as follows:

$$\begin{aligned} A^{I=1}(\cos\theta_\pi) &= A^{I=1}(-cos\theta_\pi)\,, \\ B^{I=0}(\cos\theta_\pi) &= B^{I=0}(-cos\theta_\pi)\,, \\ B^{I=1}(\cos\theta_\pi) &= -B^{I=1}(-cos\theta_\pi)\,, \\ A^{I=0}(\cos\theta_\pi) &= -A^{I=0}(-cos\theta_\pi)\,. \end{aligned} \tag{4.6}$$

It follows from the equation 4.6 that both $B^{I=1}$ and $A^{I=0}$ turn to zero at $\theta_\pi = 90^0$, therefore one can write the following important relation for the angle $\theta_\pi = 90^0$:

$$(1 + A_{x,x})\frac{d\sigma}{d\Omega}(np \to pp_s\pi^-) = \frac{d\sigma}{d\Omega}(pp \to pp_s\pi^0)\,. \tag{4.7}$$

This relation is obtained if one adds the first and the third equation from (4.4) together, setting $\theta_\pi = 90^0$, and then takes into account that $A = A^{I=0} + A^{I=1}$, where $A^{I=0}(90^\circ) = 0$, and $B^{I=1}(90^\circ) \equiv 0$.

[1] Here it is necessary to emphasize that the isovector pp channel differs from the isovector pn channel by the total isospin projection, therefore in the general case one can expect that these amplitudes are different numerically, as, for example, the amplitudes of the processes $pp \to d\pi^+$ and $pn \to d\pi^0$ differ from each other. The dependence on the isospin projections is determined by the Wigner-Eckart theorem by the value of the corresponding Clebsch-Gordan coefficient. In the case under consideration, this coefficient is $(1110|11) = \frac{1}{\sqrt{2}}$ for $M(pp \to \{pp\}_s\pi^0)$ and $(111-1|10) = \frac{1}{\sqrt{2}}$ for the isovector part of the amplitude $M(pn \to \{pp\}_s\pi^-)$. Therefore, the Clebsch-Gordan coefficients for both reactions in the isovector channel are equal, so in the expressions above, the same amplitude $M^{I=1}$ is used.

It turns out that regardless of the process dynamics and the assumptions that are made in the analysis, the value of the spin-correlation coefficient $A_{x,x}$ in the reaction $np \to \{pp\}_s\pi^-$ at 90^0 is fixed by the values of the unpolarized differential cross sections for the reactions $np \to \{pp\}_s\pi^-$ and $pp \to \{pp\}_s\pi^0$. However, the quasi-free nature of the experiment with the π^- production, and the difference in the masses of both pions and nucleons leads to the fact that there is an uncertainty in the relative normalizations of these two unpolarized measurements, and therefore direct measurement of $A_{x,x}$ is preferable.

Another useful result follows from the symmetry relations 4.6 and the equations 4.4: for the reaction $pp \to \{pp\}_s\pi^0$ $A_{x,x} = 1$ at 90^0.

4.1.3 Partial wave decomposition

The experiment was carried out around the energy of 353 MeV, and for such low energies it can be assumed that only the few pion partial waves contribute. The first partial-wave analysis of the low-energy data for the pion capture on the diproton in the nucleus ^3He, $\pi^- pp_s \to np$, at $T_\pi = 85$ MeV, which corresponds to $T_n = 425$ MeV in the nd rest frame, was performed taking into account the s- and p-wave pions [?]. However, as was shown in [63], in the process under consideration the contribution of the pion d-waves is significant and can not be neglected. In our analysis, the terms of the expansion up to the pion d waves was kept, and, for this case, there are three possible transitions from the initial state $I = 1$: $^3P_0 \to {}^1S_0 s$, $^3P_2 \to {}^1S_0 d$ and $^3F_2 \to {}^1S_0 d$. Let's denote these amplitudes as M_s^P, M_d^P and M_d^F, respectively. In the case of the initial state $I = 0$, there are two p-wave transitions (with regard to the final pions): $^3S_1 \to {}^1S_0 p$ and $^3D_1 \to {}^1S_0 p$. Their amplitudes are denoted as M_p^S and M_p^D, respectively.

The scalar amplitudes can be decomposed in terms of these partial waves as [13]

$$\begin{aligned} A^{I=1} &= M_s^P - \frac{1}{3}M_d^P + M_d^F(\cos^2\theta_\pi - \frac{1}{5})\,, \\ B^{I=1} &= (M_d^P - \frac{2}{5}M_d^F)\cos\theta_\pi\,, \\ A^{I=0} &= M_p^D\cos\theta_\pi\,, \\ B^{I=0} &= M_p^S - \frac{1}{3}M_p^D\,. \end{aligned} \tag{4.8}$$

These relations satisfy, of course, the symmetry conditions 4.6. Thereat, for the amplitudes A and B in the expressions 4.3 and 4.4, the following relations are true:

$$\text{for the process} \quad pp \to \{pp\}_s \pi^0 : \quad A = A^{I=1},\ B = B^{I=1}$$
$$\text{for the process} \quad pn \to \{pp\}_s \pi^- : \quad A = \frac{1}{\sqrt{2}}(A^{I=0} + A^{I=1}),\ B = \frac{1}{\sqrt{2}}(B^{I=0} + B^{I=1})$$

The partial-wave amplitudes depend only on the energy and act at the threshold as k^l, where l is the pion angular moment. Thus, for small k (near the threshold), higher waves are suppressed by an angular momentum barrier. In 4.6 one should take into account the contribution of all waves up to the pion d-wave. But the contribution of the d-wave squared is not taken into account. One should note that the contribution of the $s-g$ interference, which has the same threshold behavior as the d-wave squared, is assumed to be negligibly small in comparison with the contribution of the pure d-wave and is not taken into account in our analysis.

Required assumptions for the partial wave analysis

As already was noted, the partial wave decomposition procedure leads to ambiguous solutions, even in case of the complete set of the measurements of the independent spin observables of the corresponding process [12,80]. In practice [?,84], the Watson theorem is applied to minimize the ambiguities [?, 81]. This theorem is a consequence of the S-matrix unitarity and the invariance over the time reversal, and impose restrictions on the phases of the individual partial amplitudes.

For the uncoupled partial waves, in the case of very small the inelasticity, the Watson theorem connects the phase of the interaction amplitude in the initial state of the process $NN \to NN\pi$ to the phase-shift of the elastic nucleon-nucleon scattering [?, 81]. These conditions apply for the ${}^3P_0$ partial wave and, therefore, the amplitude $M_s^P = |M_s^P| e^{i\delta_{^3P_0}}$ with $\delta_{^3P_0} = -14.8^0$ was taken [82]. The phase associated with the ${}^1S_0$ final pp state is not included because it is common for all partial waves and does not influence the observables.

For the coupled channels, such as ${}^3P_2 - {}^3F_2$, the terms of the Watson theorem, in general, do not strictly apply. However, the phase shift analysis of the pp data at 353

MeV shows that the mixing parameter, as well as the inelasticities, are very small [82]. Thus, for a good approximation, one may neglect the channel coupling and use the Watson theorem also to the individual $^3P_2$ and $^3F_2$ partial waves. Here the phases are $\delta_{^3P_2} = 17.9^0$ and $\delta_{^3F_2} \approx 0^0$ [82].

Two theoretical potential models also suggest that the $^3P_2 - ^3F_2$ channel coupling is weak [1, 54]. The quality of this approximation was also checked by the direct calculations of the d-wave production amplitudes within the chiral effective field theory up to the order of m_π/m_N (N^2LO) [83]. By these calculations, it was shown that the assumptions about the phases made here should be valid within $\pm 2^o$. It should, however, be noted that we do not neglect the channel coupling in the $^3S_1 - ^3D_1$ case, where the tensor interaction coupling can be very strong. The phases of the $I = 0$ amplitudes, M_p^S and M_p^D, are determined in the in the analysis procedure through their interference with the $I = 1$ amplitudes.

4.2 Differential cross section $d\sigma/d\Omega$ and analyzing power A_y of the process $pn \to \{pp\}_s\pi^-$

The procedures of the identification of the process events, the determination of the relative normalization of the beam polarization modes, and the determination of the luminosity and polarization for this measurement are described in Sec. 3.4.1-3.4.3.

Fig. 4.1 shows the results for the differential cross section $d\sigma/d\Omega$ of the quasi-free $pn \to \{pp\}_s\pi^-$ reaction, integrated over the excitation energy range $E_{pp} = (0 - 3)$ MeV and averaged over the effective beam energy $T_{\text{free}} = 353 \pm 20$ MeV (the cross section values are given in the table 4.2). The results were extracted within the impulse approximation model, and the spectator proton momentum distribution corresponded to the Bonn deuteron wave function [1]. It should be noted that the choice of a potential did not play an important role due to the use of the small spectator momentum range $P_{\text{spec}} < 106$ MeV/c, where the modern NN-potentials show complete agreement with each other. The cross section was estimated separately for the cases of the pion π^- and spectator proton detection. The results were found to be consistent, and Fig. 4.1 shows

the averaged values. Also the TRIUMF data for the quasi-free π^--production [10] are shown. In that experiment, however, a stronger restriction was imposed on $E_{pp} < 1.5$ MeV, and the results were converted to the $E_{pp} < 3$ MeV limit, used in our work, using the Migdal-Watson energy variation for the s-wave pp-interaction in the final state [?, 81].

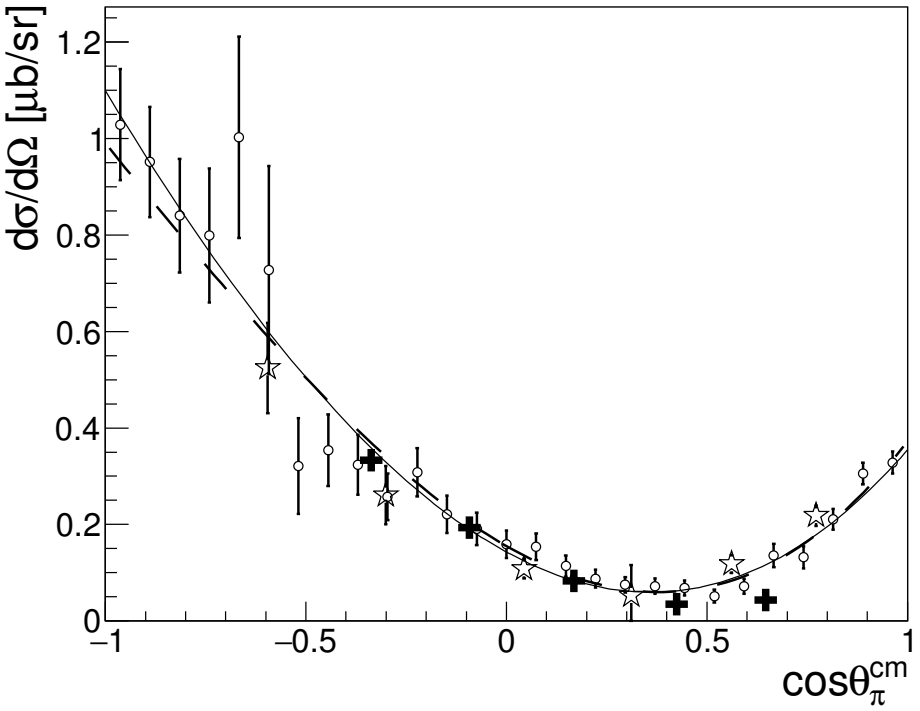

Figure 4.1: Unpolarised differential cross section for the $pn \to \{pp\}_s\pi^-$ reaction. The ANKE data with statistical errors are shown by empty circles. There is systematic error of 6%, arising from the uncertainties of the luminosity and acceptance determination. The statistical errors of the TRIUMF $pn \to \{pp\}_s\pi^-$ results are shown by the crosses [10], the statistical errors here are generally smaller than the symbol size and their normalisation uncertainty is 10%. The arbitrarily scaled TRIUMF cross sections extracted from $\pi^-{}^3He \to pnn_{spec}$ data [84] are shown with the stars. The dashed curve is a direct cubic fit of these ANKE data whereas the solid one corresponds to the result of the partial wave analysis from Sec. 4.3.

While the TRIUMF results cover only the central region of pion angles [10], the current data extend over the whole angular range. Both data sets are consistent in the pion backward emission region but the TRIUMF measurements do not show any rise

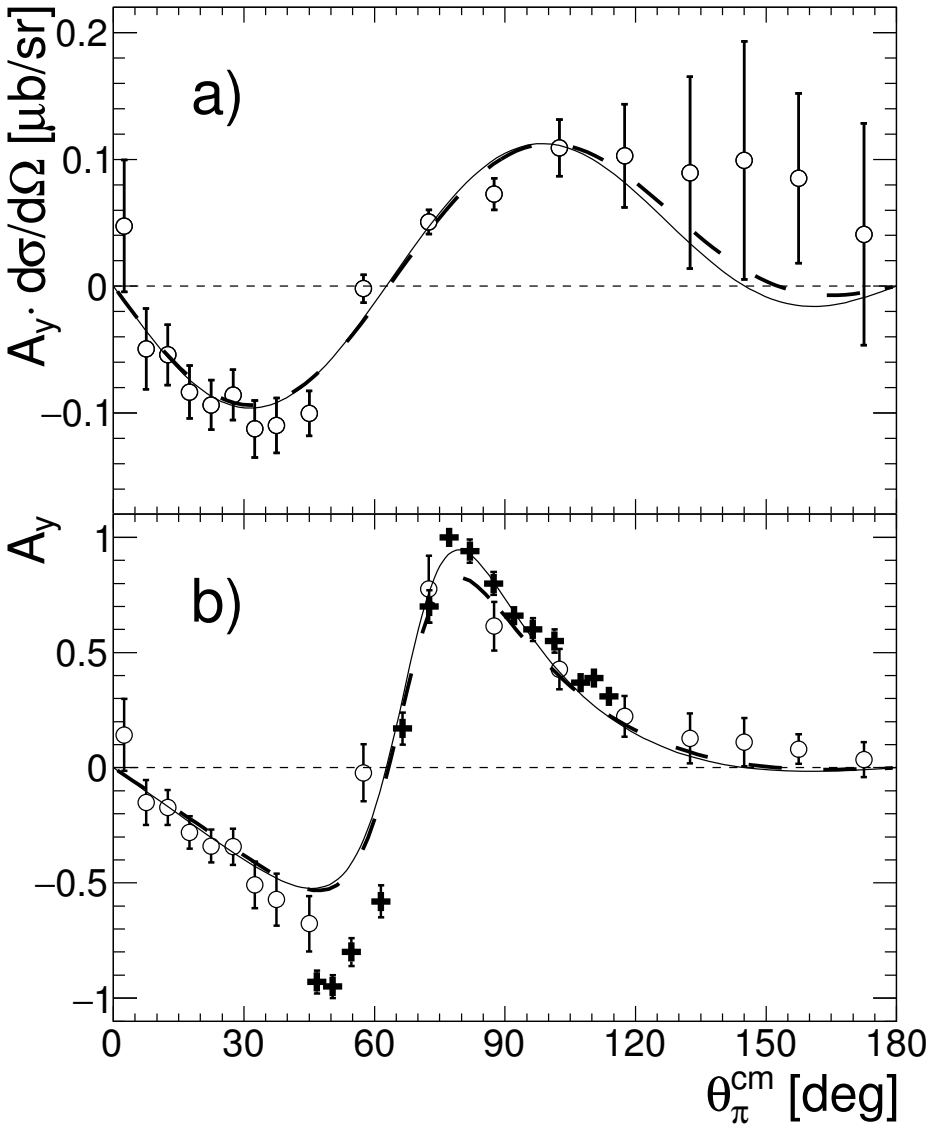

Figure 4.2: (a) The product of the measured analysing power A_y^p and differential cross section for the $pn \to \{pp\}_s\pi^-$ reaction at 353 MeV depending on the pion emission angle. Only statistical errors are shown, systematic uncertainty of 11% is not included. The dashed curve represents the best fit of Eq. 4.10 whereas the solid one corresponds to the result of the partial wave analysis from Sec. 4.3. (b) The measured values of A_y^p obtained on ANKE (empty circles) and on TRIUMF [9] (crosses). Systematic uncertainty in the ANKE data is 9%. The dashed and solid lines represent the division results of the fit from the panel (a) and the cross section from Fig 4.1.

at the forward angles, that is seen at ANKE. Some confirmation of the ANKE angular shape is offered by the pion absorption data, $\pi^- {}^3He \to pnn_{sp}$, where the unobserved slow neutron is assumed to be a spectator [84]. In this case, this reaction can be interpreted as $\pi^- \{pp\}_s \to pn$, though the internal structure of the diproton is very different to that in the production data. Over the range of angles covered, the ANKE data are consistent with the pion capture results. The forward/backward peaking is in contrast to the results found for π^0 production [63, 80] and is an indication of the dominance of the $I = 0$ p-wave amplitudes in the π^- production reaction.

The unpolarized cross section for the π^- production and the proton vector analyzing power A_y^p can be written in the form of:

$$\left(\frac{d\sigma}{d\Omega}\right)_0 = \frac{k}{4p}\sum_{n=0} a_n \cos^n\theta_\pi \,, \tag{4.9}$$

$$A_y\left(\frac{d\sigma}{d\Omega}\right)_0 = \frac{k}{4p}\sin\theta_\pi \sum_{n=0} b_{n+1}\cos^n\theta_\pi \,. \tag{4.10}$$

Table 4.1 shows the parameters for Equation 4.9 obtained with the ANKE data fit. As can be seen from Fig. 4.1, the cross section data are well described by a cubic parabola, and the inclusion of a fourth degree in the fit does not improve the value of $\chi^2/n.d.f.$.

$a_0(pn)$	$a_1(pn)$	$a_2(pn)$	$a_3(pn)$	$b_1(pn)$	$b_2(pn)$	$b_3(pn)$
2.69 ± 0.18	-8.24 ± 0.51	9.11 ± 0.70	2.89 ± 0.90	1.77 ± 0.14	-1.95 ± 0.50	-4.43 ± 0.70

Table 4.1: Parameter values in units of $\mu b/sr$ obtained by the direct fit of the experimental data of the reaction $pn \to \{pp\}_s\pi^-$ by the relations 4.9 and 4.10. Only statistical errors are given, systematic uncertainties were 6% in the cross section and 9% in the analyzing power.

The results for the analyzing power A_y^p, as well as A_y^p, weighted with the cross section, are shown in Fig. 4.2 (the corresponding values are given in Table 4.3). The agreement with the TRIUMF A_y^p data [9] is reasonable at large pion emission angles and both show the strong and rather asymmetric oscillation in the central region. However, there are clear discrepancies for $\theta_\pi \leq 60^\circ$ for both the analyzing power A_y^p as for the cross section $d\sigma/d\Omega$ shown in Fig. 4.1.

Fitting the weighted A_y^p distribution with the form of 4.10 requires at least three terms given in Table 4.1. Moreover, the inclusion of higher degrees does not change

significantly the results of the fit. The associated curve is shown in Fig. 4.2 and this divided by the parameterisation of the cross section in Fig. 4.2b.

Central value $\cos\theta_\pi^{cm}$ in the bin	Bin width	$d\sigma/d\Omega$ [μb/sr]
-0.963	0.074	1.03 ± 0.12
-0.889	0.074	0.95 ± 0.11
-0.815	0.074	0.84 ± 0.12
-0.741	0.074	0.80 ± 0.14
-0.667	0.074	1.00 ± 0.21
-0.593	0.074	0.73 ± 0.22
-0.519	0.074	0.32 ± 0.10
-0.444	0.074	0.354 ± 0.074
-0.370	0.074	0.324 ± 0.062
-0.296	0.074	0.257 ± 0.048
-0.222	0.074	0.308 ± 0.050
-0.148	0.074	0.221 ± 0.039
-0.074	0.074	0.191 ± 0.034
0.000	0.074	0.159 ± 0.029
0.074	0.074	0.154 ± 0.027
0.148	0.074	0.114 ± 0.022
0.222	0.074	0.088 ± 0.018
0.296	0.074	0.075 ± 0.016
0.370	0.074	0.072 ± 0.016
0.444	0.074	0.068 ± 0.016
0.519	0.074	0.051 ± 0.013
0.593	0.074	0.072 ± 0.016
0.667	0.074	0.136 ± 0.024
0.740	0.074	0.132 ± 0.023
0.815	0.074	0.211 ± 0.022
0.889	0.074	0.305 ± 0.022
0.963	0.074	0.328 ± 0.023

Table 4.2: Differential cross section for the reaction $pn \to \{pp\}_s\pi^-$ depending on the cosine of the pion emission angle (empty circles in Fig. 4.1). Only statistical errors are presented.

4.2.1 Reanalysis using the STT time information

As was said in Sec. 3.4.4 the use of the STT time information made it possible to suppress the background of random coincidences and increase statistics by including

events with $T_{\rm spec} < 2.5$ MeV. However, for some of these events, the STT efficiency is difficult to estimate, as well as the calculation of the full acceptance has the additional uncertainty. In this regard, the purpose of the reanalysis was only to improve the accuracy of the analyzing power determination. As a result of the reanalysis, the statistics of the process $pn \to \{pp\}_s\pi^-$for exit angles of $\theta_\pi^{cm} > 30^\circ$ increased approximately by two times. For smaller angles where the pions were detected directly in the ND, the statistics improvement was less significant.

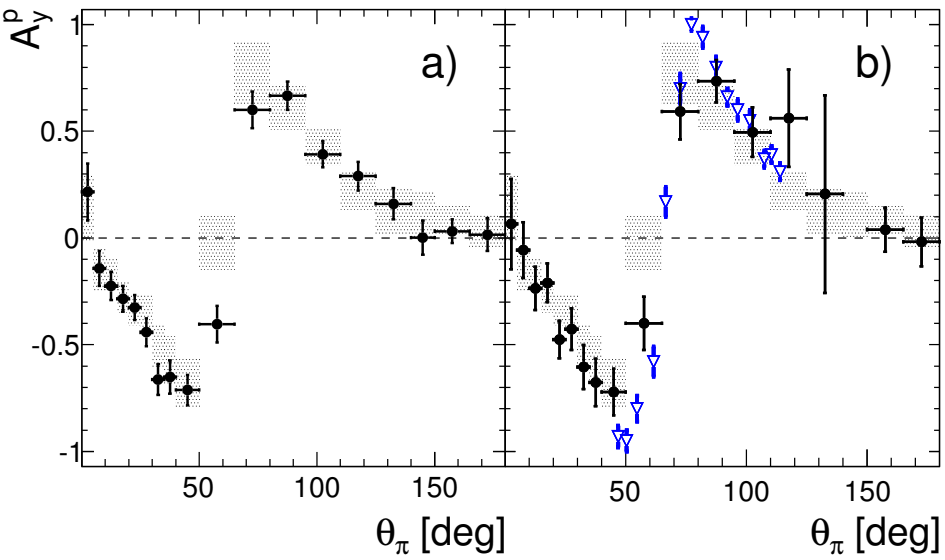

Figure 4.3: Analyzing power A_y^p of the reaction $\vec{p}n \to \{pp\}_s\pi^-$ at 353 MeV. The data obtained without the use of the STT time information and with the cut of $E_{pp} < 3$ MeV are shown by the shaded area. The black dots denote the results of the analysis with the use of the time information obtained with an energy cut of E_{pp} (a) 3 MeV and (b) 1.5 MeV. Triangles indicate the TRIUMF data [9]. Only statistical errors are shown.

The statistics increase allowed to impose a more tighter constraint on the diproton excitation energy $E_{pp} < 1.5$ MeV, similar to that used in the TRIUMF experiment [9]. Fig. 4.3 shows the data for A_y^p obtained by the new method for two cuts over the energy E_{pp} (in Table 4.3 the corresponding values are given), in comparison with the ANKE data obtained without the use of the STT time information, and with the TRIUMF data [9]. It can be seen that the analyzing power does not change with the introduction of a more tighter cut on the E_{pp}.

Centrer of bin θ_π^{cm} [grad]	Bin width [grad]	$A_y^p \cdot d\sigma/d\Omega$ [μb/sr]	A_y^p	A_y^p with the use of STT time information	
				$E_{pp} < 3$ MeV	$E_{pp} < 1.5$ MeV
2.5	5	0.05 ± 0.05	0.14 ± 0.16	0.22 ± 0.13	0.07 ± 0.21
7.5	5	-0.05 ± 0.03	-0.15 ± 0.10	-0.14 ± 0.08	-0.06 ± 0.13
12.5	5	-0.05 ± 0.02	-0.17 ± 0.08	-0.23 ± 0.07	-0.24 ± 0.10
17.5	5	-0.08 ± 0.02	-0.28 ± 0.07	-0.28 ± 0.06	-0.21 ± 0.09
22.5	5	-0.09 ± 0.02	-0.34 ± 0.07	-0.33 ± 0.06	-0.48 ± 0.09
27.5	5	-0.09 ± 0.02	-0.34 ± 0.07	-0.44 ± 0.07	-0.43 ± 0.10
32.5	5	-0.11 ± 0.02	-0.51 ± 0.10	-0.66 ± 0.07	-0.60 ± 0.10
37.5	5	-0.11 ± 0.02	-0.57 ± 0.11	-0.65 ± 0.08	-0.68 ± 0.11
45.0	10	-0.10 ± 0.02	-0.68 ± 0.12	-0.71 ± 0.07	-0.72 ± 0.11
57.5	15	-0.002 ± 0.011	-0.02 ± 0.12	-0.40 ± 0.09	-0.40 ± 0.13
72.5	15	0.051 ± 0.010	0.78 ± 0.15	0.60 ± 0.09	0.59 ± 0.13
87.5	15	0.073 ± 0.012	0.61 ± 0.11	0.67 ± 0.07	0.73 ± 0.10
102.5	15	0.11 ± 0.02	0.43 ± 0.09	0.39 ± 0.06	0.50 ± 0.12
117.5	15	0.10 ± 0.04	0.22 ± 0.09	0.29 ± 0.07	0.56 ± 0.23
132.5	15	0.09 ± 0.08	0.13 ± 0.11	0.16 ± 0.07	0.21 ± 0.46
145.0	10	0.10 ± 0.09	0.11 ± 0.11	0.00 ± 0.08	0.00 ± 0.00
157.5	15	0.09 ± 0.07	0.08 ± 0.06	0.03 ± 0.06	0.04 ± 0.10
172.5	15	0.04 ± 0.09	0.04 ± 0.08	0.02 ± 0.08	-0.02 ± 0.11

Table 4.3: Analyzing power A_y and that multiplied by the differential cross section for the reaction $pn \to \{pp\}_s\pi^-$ at 353 MeV, depending on the emission pion angle. Only statistical errors are given. The second and third columns show the results of the analysis without the use the STT time and with the cut on the $E_{pp} < 3$ MeV, the 4th and 5th show the result obtained with the time information and the cuts on the E_{pp} indicated in the table.

4.3 First partial-wave analysis of the ANKE data

The first approach to the data analysis described here relied on the ANKE data for the reactions $pp \to \{pp\}_s \pi^0$ [80] and $pn \to \{pp\}_s \pi^-$ [12] (the latter are presented in Sec. 4.2) which include the differential cross section and A_y^p for both processes. The amplitudes of the s- and d-pion waves could be determined from the π^0 production data taking into account the assumptions described in Sec. 4.1.3, and the results of such analysis are cited in Tables 4.5 and 4.4 in comparison with the combined analysis of both reactions. The results of the data $pn \to \{pp\}_s \pi^-$ reanalysis, given in Sec. 4.2.1, were not used in this analysis.

As described in Sec. 4.1.3, it is reasonable to limit the set with the s, p and d partial waves at 353 MeV, which requires the determination of 5 partial amplitudes: M_s^P, M_p^S, M_p^D, M_d^P and M_d^F, connected with the spin amplitudes and the observables by the relations 4.4 and 4.8

On the other hand, the number of parameters extracted from the data is determined by the fit with the empirical relations 4.9 and 4.10. The connection between the empirical parameters and the partial waves, with the expansion up to $p-d$ interference and the neglection of the d-wave squares, is given by the relations

$$\begin{aligned}
a_0 &= \tfrac{1}{2}|M_{\rm s}^P|^2 + \tfrac{1}{2}|M_{\rm p}^S - \tfrac{1}{3}M_{\rm p}^D|^2 - \tfrac{1}{3}\mathrm{Re}\left[M_{\rm s}^{P*}(M_{\rm d}^P + \tfrac{3}{5}M_{\rm d}^F)\right] \\
a_1 &= \mathrm{Re}\left[M_{\rm s}^{P*}(M_{\rm p}^S + \tfrac{1}{3}M_{\rm p}^D) + \tfrac{2}{3}M_{\rm d}^{P*}(M_{\rm p}^S - \tfrac{5}{6}M_{\rm p}^D)\right. \\
&\quad \left. -\tfrac{3}{5}M_{\rm d}^{F*}M_{\rm p}^S\right] \\
a_2 &= \tfrac{1}{6}|M_{\rm p}^D|^2 + \mathrm{Re}\left[M_{\rm s}^{P*}(M_{\rm d}^P + \tfrac{3}{5}M_{\rm d}^F) + M_{\rm p}^{S*}M_{\rm p}^D\right] \\
a_3 &= \mathrm{Re}\left[[M_{\rm p}^{D*}(M_{\rm d}^P + \tfrac{4}{15}M_{\rm d}^F) + M_{\rm p}^{S*}M_{\rm d}^F\right] \\
b_1 &= \mathrm{Im}\left[(M_{\rm p}^{S*} - \tfrac{1}{3}M_{\rm p}^{D*})(M_{\rm s}^P - \tfrac{1}{3}(M_{\rm d}^P + \tfrac{3}{5}M_{\rm d}^F))\right] \\
b_2 &= \mathrm{Im}\left[M_{\rm p}^{S*}M_{\rm p}^D - M_{\rm s}^{P*}(M_{\rm d}^P - \tfrac{2}{5}M_{\rm d}^F)\right] \\
b_3 &= \mathrm{Im}\left[M_{\rm d}^{P*}M_{\rm p}^D - M_{\rm d}^{F*}(M_{\rm p}^S + \tfrac{1}{15}M_{\rm p}^D)\right] \ . \qquad (4.11)
\end{aligned}$$

Since the spin of the initial NN-pair is 1, the sum of the pion orbital angular moment l and the initial nucleon-nucleon isospin $l+I$ is odd. Therefore, in the case of the $pp \to \{pp\}_s \pi^0$ reaction, only even pion partial waves are allowed. As shown

in [80], in order to describe the data of this process it is enough to take into account the coefficients a_0, a_2 and b_2 from the equations 4.9 and 4.10. In expressions 4.11, the contributions of the pion p-waves fall out for the π^0 production process, and the right side doubles.

By neglecting the small coupling between the ${}^3P_2$ and ${}^3F_2$ partial waves, and imposing the Watson theorem, one can fix the phases for the complex amplitudes M_s^P, M_d^P and M_d^F [80]. However, such an approach is not valid for the two p-waves due to the strong coupling between the initial ${}^3S_1$ and ${}^3D_1$ states. Thus, the total number of free fit parameters is seven, whereas the total number of observables in both reactions is 10 (three expansion coefficients for the $pp \to \{pp\}_s\pi^0$ and seven for the $pn \to \{pp\}_s\pi^-$). Despite the fact that there is a significant general relative uncertainty between the π^- and π^0 production data, related to luminosity and other systematic effects, it becomes obvious that the system is overdetermined. Therefore, if an acceptable solution is found, it would support the assumptions made in the analysis, such as the neglection higher partial waves, the $d-d$ interference, and the coupling effect between ${}^3P_2$ and ${}^3F_2$ partial waves.

The best agreement with the $pp \to \{pp\}_s\pi^0$ and $pn \to \{pp\}_s\pi^-$ data was obtained for the amplitudes given in Table 4.4 in comparison with the results of a separate fit of the $pp \to \{pp\}_s\pi^0$ data [80]. As can be seen, the results for s and d waves differ little for these two cases.

Amplitudes	Joint analysis	Only π^0 data
M_s^P	$(55.3 \pm 0.4) - (14.7 \pm 0.1)i$	$(55.3 \pm 0.4) - (14.6 \pm 0.1)i$
M_d^P	$-(26.6 \pm 1.1) - (8.6 \pm 0.4)i$	$-(26.8 \pm 1.2) - (8.7 \pm 0.4)i$
M_d^F	5.3 ± 2.3	(6.0 ± 2.4)
M_p^S	$-(32.4 \pm 2.2) + (17.3 \pm 2.7)i$	
M_p^D	$-(109.6 \pm 9.6) + (140.7 \pm 4.0)i$	

Table 4.4: The results of the partial-wave analysis of the $pp \to \{pp\}_s\pi^0$ and $pn \to \{pp\}_s\pi^-$ processes in units of $\sqrt{\text{nb/sr}}$. The second column shows the results of the joint two processes analysis, the third one cites the $pp \to \{pp\}_s\pi^0$ analysis data [80].

This solution has $\chi^2/NDF = 89/82$, which means that the used limited decompositions can lead to a very good description of the data. The contribution of the ${}^3F_2 \to {}^1S_0 d$ transition is clearly small, and if one completely eliminate M_d^F, this will only lead to a slightly less accurate description of the data with $\chi^2/NDF = 94/82$. It should also be noted that while the phases M_s^P, M_d^P and M_d^F were preset, the M_p^S and M_p^D phases were extracted from the data.

The quality of this parameterization can also be judged by comparing the curves in Fig. 4.1 and 4.2 with the data. The remaining slight discrepancy in the analyzing power description may arise due to neglect of the smaller terms. However, it should also be borne in mind that the main systematic uncertainty, namely the relative normalizations between the data sets for the $pp \to \{pp\}_s\pi^0$ and $pn \to \{pp\}_s\pi^-$, was not taken into account in the determination of the parameters. On the other hand, adjusting the normalizations by a few percent does not lead to any qualitative changes in the solution 4.4.

Another way to estimate the quality of the parametrization made is to compare the parameters obtained by the direct fit of the individual distributions for the observables and a common fit, which parametrizes all data at the same time. The way the parameters vary depending on the fittings procedure, can be seen in Table 4.5. In the resulting parameters, after the direct and common fit, no difference was found at all for the $pp \to \{pp\}_s\pi^0$ reaction. In the case of the $pn \to \{pp\}_s\pi^-$ reaction, only the parameter $a_3(pn)$ differs by more than three error values.

The conclusion following from the results 4.4 is that, in spite of the significance of the d-wave in the pion production, it arises almost exclusively from the ${}^3P_2$ state, since the ${}^3F_2 \to {}^1S_0 d$ transition contributes very little. In the case of the $pp \to \{pp\}_s\pi^0$ reaction, the transition amplitude ${}^3D_1 \to {}^1S_0 p$ dominated.

It should be noted that the first attempt of the partial-wave analysis of the $pn \to \{pp\}_s\pi^-$ reaction near the threshold was undertaken in [9] using the TRIUMF data on the differential cross section and A_y^p for this process [9, 10]. At that time, there was no data on the π^0 production in the process $pp \to \{pp\}_s\,\pi^0$, which limited the contribution of the s- and d-waves, and the authors were forced to rely on the Watson

Observable	Direct fit	PWA
$a_0(pp)$	4.05 ± 0.08	4.05 ± 0.08
$a_2(pp)$	-2.31 ± 0.14	-2.34 ± 0.14
$b_2(pp)$	1.82 ± 0.10	1.80 ± 0.10
$a_0(pn)$	2.69 ± 0.18	2.47 ± 0.08
$a_1(pn)$	-8.24 ± 0.51	-7.83 ± 0.45
$a_2(pn)$	9.11 ± 0.70	10.12 ± 0.41
$a_3(pn)$	2.89 ± 0.90	1.38 ± 0.27
$b_1(pn)$	1.77 ± 0.14	1.82 ± 0.13
$b_2(pn)$	-1.95 ± 0.50	-1.75 ± 0.36
$b_3(pn)$	-4.43 ± 0.70	-4.83 ± 0.27

Table 4.5: Expansion parameters in units of $\mu b/sr$ obtained by the direct fit of the experimental data for the reactions $pp \to \{pp\}_s \pi^0$ [80] and $pn \to \{pp\}_s \pi^-$ [12] (this paper) by the relations 4.9 and 4.10 (the second column), and from the results of the joint partial wave analysis based on the relations 4.11 (the third column). The errors are purely statistical. For the case of π^- meson production there are systematic uncertainties of 6% in the cross section and 9% in the analyzing power.

theorem applicability even for strongly coupled ${}^3S_1$ and ${}^3D_1$ waves. In addition, their data were obtained only in the central angular region, so it is not surprising that the results of the TRIUMF analysis are significantly different from the ANKE results reported in this section. Thus, in [9] the conclusion about negligibility of the d-waves was made and the dominant role of the transition ${}^3D_1 \to {}^1S_0 p$ was specified.

4.4 Results of the experiment with double polarization for the $\vec{n}\,\vec{p} \to \{pp\}_s \pi^-$

4.4.1 Cross-section and analyzing powers A_y^p and A_y^n

The determination of the differential cross section and the analyzing power for the $\vec{n}\vec{p} \to \{pp\}_s \pi^-$ reaction in dp kinematics opens the possibility of checking the correct-

ness of the double polarization experiment, which is more complicated for the analysis. A different registration procedure of the reaction products in detectors also makes it possible to verify the correctness of the systematic estimation in the previous experiment. It is much more difficult to estimate the exact value of absolute luminosity for the data obtained with a long cell than for those with a point interaction vertex. Therefore, in Fig. 4.4a only an arbitrarily normalized cross section, obtained from the experiment with the cell, is shown to compare the shape of that with the result presented in Sec. 4.2 and with the TRIUMF data [10]. Both cross sections obtained at the ANKE are in good agreement with each other at all angles, including in the front region, where the TRIUMF cross section begins to deviate from them.

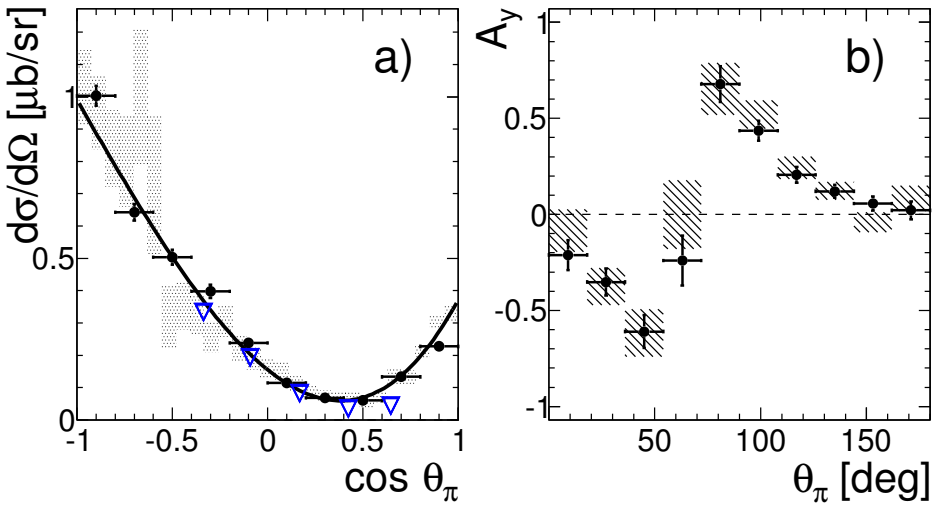

Figure 4.4: Observables obtained for the $pn \to \{pp\}_s\pi^-$ reaction at 353 MeV with a cut on the diproton excitation energy $E_{pp} < 3$ MeV. (a) Unpolarized differential cross section. The results obtained in the single-polarization experiment [12] are shown by the shaded area, the curve shows the direct cubic fit of this data. The black dots denote the results with statistical errors obtained in the double polarized experiment [13]. Since the absolute normalization was not achieved, the cross section values were normalized to an arbitrary common factor. The TRIUMF data [10] are denoted by triangles. (b) Proton analyzing power A_y^p (points), neutron analyzing power A_y^n (shaded areas) obtained at the same time from the experiment with double polarization [13].

Central value θ_π^{cm} in the bin, [grad]	Bin width, [grad]	A_y^p	A_y^n
9.0	18	-0.21 ± 0.08	-0.08 ± 0.11
27.0	18	-0.35 ± 0.07	-0.38 ± 0.10
45.0	18	-0.61 ± 0.09	-0.62 ± 0.12
63.0	18	-0.24 ± 0.13	-0.00 ± 0.18
81.0	18	0.68 ± 0.09	0.65 ± 0.14
99.0	18	0.44 ± 0.05	0.52 ± 0.07
117.0	18	0.21 ± 0.04	0.24 ± 0.06
135.0	18	0.12 ± 0.03	0.12 ± 0.05
153.0	18	0.06 ± 0.04	-0.04 ± 0.05
171.0	18	0.02 ± 0.05	0.08 ± 0.07

Table 4.6: Proton A_y^p and neutron A_y^n analyzing powers obtained for the reaction $\vec{p}\vec{n} \to \{pp\}_s\pi^-$ at 353 MeV with a cut on the diproton excitation energy $E_{pp} < 3$ MeV [13] (are denoted by dots and shaded areas, respectively in Fig. 4.4b).

The proton and neutron analyzing powers were obtained from the data with double polarization by averaging over the polarization states of the beam and target, respectively. The value of the neutron polarization from beam deuterons is smaller than for the proton target, so the error for the neutron analyzing power is greater than for the proton one. But, in general, the results for the A_y^p and A_y^n are fully compatible with each other (Fig. 4.4b, the values are given in Table 4.6), which confirms the correctness of the experiment and its analysis. The obtained results fully coincide to the previous results for the differential cross section and analyzing power (from the experiment with single polarization) and therefore can be used in a combined analysis.

4.4.2 Spin correlation coefficients $A_{x,x}$, $A_{y,y}$

It follows from the relation 4.2 that the experimental asymmetry in the double polarized experiment can be written as follows:

$$\xi = \frac{\Sigma_1 - \Sigma_2}{\Sigma_1 + \Sigma_2} = PQ(A_{x,x} \sin^2 \phi_\pi + A_{y,y} \cos^2 \phi_\pi) \,, \tag{4.12}$$

where $\Sigma_1 = N_{\uparrow\uparrow} + N_{\downarrow\downarrow}$, $\Sigma_2 = N_{\uparrow\downarrow} + N_{\downarrow\uparrow}$. Here, N denotes the number of events registered with the beam and target polarization directions, shown by arrows, normalized to the corresponding relative luminosity R, and PQ is the product of the beam and target polarizations.

The background from the cell was subtracted separately for the combinations $\Sigma_1 - \Sigma_2$ and $\Sigma_1 + \Sigma_2$. Since the background contribution has sensibly no polarization dependence, for histograms of the differences of the event numbers the background turned out to be very small.

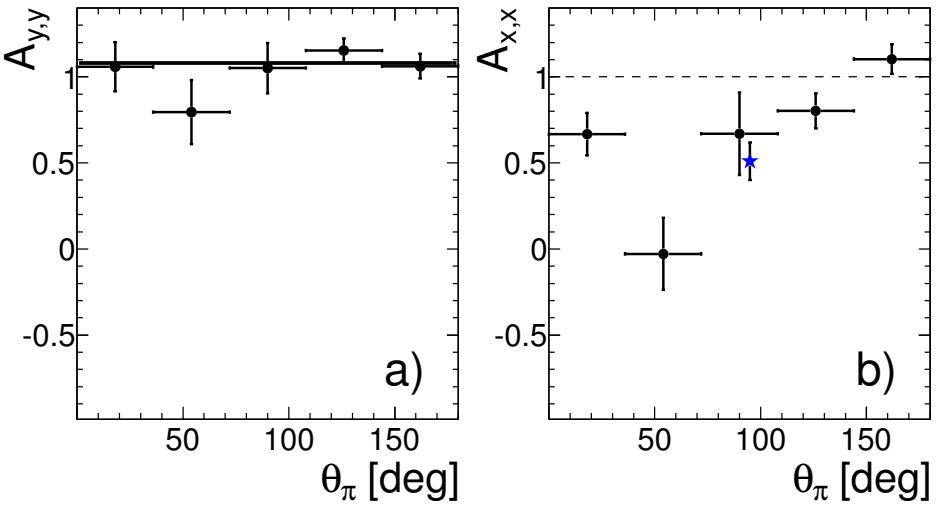

Figure 4.5: Spin correlation coefficients for the reaction $\vec{n}\vec{p} \to \{pp\}_s\pi^-$ at 353 MeV with statistical errors, as a functions of pion emission angle [13]. (a) $A_{y,y}$. The horizontal line shows a fit with a constant. (b) Values of $A_{x,x}$ were obtained after imposing the requirement $A_{y,y} = 1$ for all angles of the pion emission. The systematic uncertainties for the point 90° (the blue star, shifted slightly in angle to be distinguishable), obtained with the help of the relation 4.7, are much greater than purely statistical errors shown.

The experimental data were distributed over five bins over the pion exit angle θ_π and the value of ξ/PQ was fitted with a linear function of $\cos^2\phi_\pi$ in each bin. The detector acceptance was significantly higher for the events with large $\cos^2\phi_\pi$ values, so the coefficient $A_{y,y}$ was determined more accurately than $A_{x,x}$. The results for the spin-correlation parameters as a function of θ_π are shown in Fig. 4.5, and the values are given in Table 4.7.

As can be seen from the expression 4.12, the values of the $A_{x,x}$ and $A_{y,y}$ depend only on the product of the beam and target polarizations PQ, which in turn can be determined if, in accordance with expressions 4.4, require for the average over all the pion emission angles to be $A_{y,y} = 1$. This gives us a powerful tool for the study of the systematic uncertainties. If one takes into account the uncertainty of 0.11, which arises from the errors of the polarizations product PQ determination, the value $A_{y,y} = 1.08 \pm 0.04$, obtained during the fit, is compatible with 1. Setting $A_{y,y} = 1$, one can refine the measured value of the product $PQ = 0.373 \pm 0.015$, which can be used to determine $A_{x,x}$.

In order to reduce the uncertainties in the results for the spin-correlation coefficient $A_{x,x}$, $A_{y,y} \equiv 1$ was fixed for all the angles θ_π, after which the linear fit over the $\cos^2\phi_\pi$ was repeated. This procedure yielded the result shown in Fig. 4.5b. Statistical uncertainty dominates in the value of $A_{x,x}$ (see also Appendix A). Systematic uncertainties, in turn, arise from the error in the product of the polarization determination (0.04), the possible difference in polarizations for the opposite spin directions (0.01), the uncertainty of the relative normalization (0.023), and the effect of the longitudinal spin component appearance due to the Fermi motion in the deuteron (up to 0.07).

Fig. 4.5b also shows the value of $A_{x,x} = 0.51 \pm 0.11$ at 90^o. It is obtained with the relation 4.7, using the results of direct fit of the π^0 and π^- production cross sections. However, the error shown for this point is purely statistical and does not include systematic effects from the relative normalization uncertainty.

Central value θ_π^{cm} in the bin, [grad]	Bin width, [grad]	$A_{x,x}$	$A_{y,y}$
18.0	36	0.67 ± 0.12	1.06 ± 0.14
54.0	36	-0.03 ± 0.21	0.80 ± 0.19
90.0	36	0.67 ± 0.24	1.05 ± 0.15
126.0	36	0.80 ± 0.10	1.15 ± 0.07
162.0	36	1.10 ± 0.09	1.06 ± 0.07

Table 4.7: Values of the spin correlation coefficients $A_{x,x}$ and $A_{y,y}$ for the reaction $\vec{n}\vec{p} \to \{pp\}_s\pi^-$ at 353 MeV with statistical errors [13] (are shown by black dots in Fig. 4.5).

4.5 Partial wave analysis of the complete data set

The fit with the partial waves described in Sec. 4.3 was repeated with the new data including the reanalyzed result for A_y^p from the single polarization experiment (see Sec. 4.2.1), the A_y^p estimation from the experimental data obtained on the hydrogen cell, and the result for $A_{x,x}$. Also, the analysis took into account the significantly reduced uncertainty of the proton beam polarization as a result of the performed reanalysis (see Sec. 3.4.4). The previously obtained in the single polarized experiment values of the unpolarized cross section $(d\sigma/d\Omega)_0$ for the π^- production (Sec. 4.2), as well as the cross section and A_y^p for the $pp \to \{pp\}_s\pi^0$ reaction [80] were used in the analysis.

In contrast to the previously described analysis, the square of the d-wave amplitudes was included in the fit procedure. In addition, the uncertainty effects in the data normalization were included by constructing a complete nondiagonal covariant matrix $\mathcal{M}$ for the measured points, and by minimizing the overall shape of $\chi^2 = \delta_i \mathcal{M}_{ij}^{-1} \delta_j$, where δ_i is the measured deviation of the i-th point.

The search of a global minimum of χ^2 was first performed on a grid in the space of the magnitudes and phases of the p-wave amplitudes, and the s- and d-wave amplitudes were fixed by the fit to the π^0 production data. As a result, three minimums with very close values of χ^2 were found, after which five amplitudes were fitted nearby each minimum. It should be noted that in the first analysis (4.3) the search for a global minimum on

the grid was not performed and the result of the fit was obtained in accordance with arbitrarily chosen initial parameters. The result of the previous analysis corresponds to the first solution from this analysis and it does not correlate well with the theory expectations. The properties of the three solutions are shown in Table 4.8. As can be seen, the solutions differ from each other mainly in the parameters of p-wave amplitudes, and the s- and d-waves stay essentially unchanged.

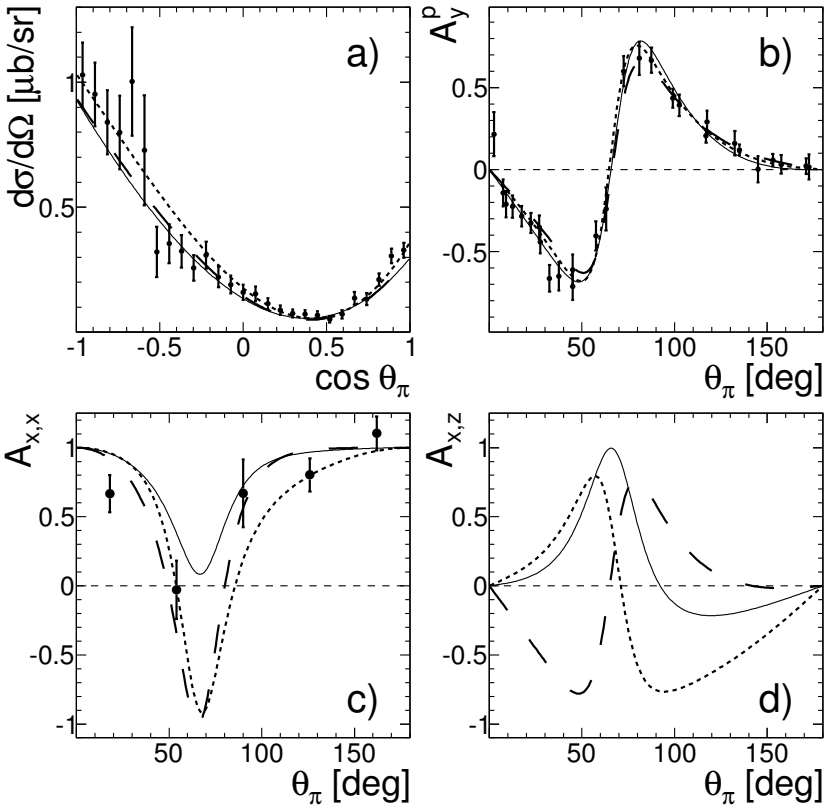

Figure 4.6: The partial-wave analysis predictions for the reaction $pn \to \{pp\}_s\pi^-$ at 353 MeV, $E_{pp} <$ 3 MeV; the solid, llong-dashed, and short-dashed lines correspond to the solutions 1, 2 and 3 from Table 4.8. Experimental results are also presented. (a) Differential cross section; (b) Analyzing power A_y^p obtained in the double-polarized experiment; (c) $A_{x,x}$; (d) $A_{x,z}$, for which there are yet no experimental data.

The predictions for the reaction $np \to \{pp\}_s\pi^-$ observables for each of the three solutions in comparison with the ANKE data are shown in Fig. 4.6. The data for the differential cross section and analyzing power A_y^p are described equally well by all three solutions. Meanwhile, the predictions for the spin-correlation coefficient $A_{x,x}$ and,

especially, for the $A_{x,z}$, differ significantly from each other. The data for the $A_{x,x}$ obtained in this paper does not contradict in general with any of the three predictions. The second and third solutions are somewhat more preferable, but given the statistical uncertainties, one can not make the final choice in favor of one of the solutions. Considering the radical differences in the predictions for the $A_{x,z}$, a measurement of this coefficient becomes especially important for the resolving the ambiguities in the analysis and determining which of the three possible solutions is physical one.

Are there any theoretical indications as to which of the three solutions of Table 4.8 is to be preferred? Because of the strong coupling between the ${}^3S_1$ and ${}^3D_1$ partial waves, the Watson theorem can not be used to deduce the phases of M_p^S and M_p^D amplitudes. Nevertheless, one can propose a cautious assumption that the phases of the solutions found should not differ drastically from the corresponding phases of elastic nucleon-nucleon scattering. It is interesting to note that the phases of the p-wave production amplitudes evaluated within χPT remain fairly close to the elastic phases, in spite of the coupled-channel dynamics [53]. It is important to note that, although according to the Watson theorem, the real production amplitude should acquire the elastic phase, one does not know whether the "bare" amplitude is positive or negative. Therefore, there is an ambiguity over the rotation by 180°, or in other words, only the tangent of the phase is relevant.

One can see from Table 4.8 that for the three solutions

$$(Im(M_p^S)/Re(M_p^S), Im(M_p^D)/Re(M_p^D)) = (-0.44,\ 1.32),\ (0.02,\ -0.48) \text{ and } (0.29,\ -0.53).$$

These are to be compared with the values from the nucleon-nucleon phase-shift analysis values of $(\tan\delta_{^3S_1}, \tan\delta_{^3D_1}) = (0.03,\ -0.46)$ [82], and with the values obtained from the theoretical analysis within χPT of (0.04, -0.61) [53]. Although this theoretical calculation does not coincide exactly with the elastic phases, nevertheless, it is much closer to the second solution than to the third one. Specifically, the difference of 0.13 in $\tan\delta_{^3D_1}$ between the theory and the second solution corresponds to a phase difference of only 5°, whereas the difference obtained for the third solution is already 14°. There is therefore a distinct preference against solution 1 and possibly in favor of solution 2. However, it is difficult to quantify up to what extent these theoretical reasoning can

isolate one of the solutions, and to clarify the situation, a direct measurement of the $A_{x,z}$ is required.

Amplitude	Real	Imaginary	Im/Re
Solution 1: $\chi^2/\text{ndf} = 101/82$			
M_s^P	53.4 ± 1.0	-14.1 ± 0.3	
M_d^P	-25.9 ± 1.4	-8.4 ± 0.4	
M_d^F	-1.5 ± 2.3	0.0 ± 0.0	
M_p^S	-37.5 ± 1.7	16.5 ± 1.9	-0.44 ± 0.06
M_p^D	-93.1 ± 6.5	122.7 ± 4.4	-1.32 ± 0.11
Solution 2: $\chi^2/\text{ndf} = 103/82$			
M_s^P	52.7 ± 1.0	-13.9 ± 0.3	
M_d^P	-28.9 ± 1.6	-9.4 ± 0.5	
M_d^F	3.4 ± 2.6	0.0 ± 0.0	
M_p^S	-63.7 ± 2.5	-1.3 ± 1.6	0.02 ± 0.03
M_p^D	-109.9 ± 4.2	52.9 ± 3.2	-0.48 ± 0.03
Solution 3: $\chi^2/\text{ndf} = 106/82$			
M_s^P	50.9 ± 1.1	-13.4 ± 0.3	
M_d^P	-26.3 ± 1.5	-8.5 ± 0.5	
M_d^F	2.0 ± 2.5	0.0 ± 0.0	
M_p^S	-25.4 ± 1.9	-7.3 ± 1.5	0.20 ± 0.07
M_p^D	-172.2 ± 5.6	92.0 ± 6.2	-0.53 ± 0.04

Table 4.8: Real and imaginary amplitudes values for the five lowest partial waves, determined from the fit of the $pp \to \{pp\}_s\pi^0$ and $np \to \{pp\}_s\pi^-$ [13]. The ratios of imaginary to real parts of the amplitudes that were freely fitted are also shown. The other three relations unspecified were fixed by the Watson theorem.

4.6 Spin correlation coefficients $A_{x,x}$, $A_{y,y}$ of the reaction $\vec{n}\,\vec{p} \to d\pi^0$

In addition to the main task of the experiment with the polarized beam and target, the spin observables for the process $\vec{n}\,\vec{p} \to \{pp\}_s\pi^-$determination, the same data allowed to extract the spin-correlation coefficients $A_{x,x}$, $A_{y,y}$ of the reaction $\vec{n}\,\vec{p} \to d\pi^0$ [14].

It follows from isospin invariance that the cross section for the process $np \to d\pi^0$ should be half of that for $pp \to d\pi^+$ but all the spin observables should be identical for the two reactions. The $pp \to d\pi^+$ reaction has been intensively studied, and a vast set of data on the cross section, analyzing powers, spin correlations and spin transfers in both the direct and reverse channels has been accumulated. These data were used in the SAID phase analysis for the proton beam energies up to 1.3 GeV [76]. In contrast, there are relatively few measurements of the cross section for the reaction $np \to d\pi^0$ [85, 86], and even less is known about the spin dependence of the process. The following analysis aimed to fill this gap and compare the results of the pn-interaction with the available data for the $pp \to d\pi^+$ and with the phase analysis predictions.

In order to solve this problem, methods of the background subtraction and the reconstruction of the interaction vertex when measured with a target with an long storage cell, described in Sec. 3.5.2 and 3.5.3, were used. The beam and target polarization values and the relative normalizations, determined in the data analysis of the reaction $\vec{n}\,\vec{p} \to \{pp\}_s\pi^-$, were also applied in this analysis. The identification of secondary particles and the events selection of the quasi-free reaction $\vec{n}\,\vec{p} \to d\pi^0$ are described in Sec. 3.5.1. The systematic uncertainty sources and their estimation are also similar to the case of $\vec{n}\,\vec{p} \to \{pp\}_s\pi^-$. Only events with the effective neutron energy within a limited interval $333 < T_{\text{free}} < 373$ MeV were used in the analysis. The average energy was varied over angle from 351 MeV to 357 MeV, being the smallest at $\theta \approx 90°$.

The procedure of the spin correlations values obtain is similar to that used to estimate $A_{x,x}$ and $A_{y,y}$ for the quasi-free reaction $\vec{n}\,\vec{p} \to \{pp\}_s\pi^-$. The ϕ_π-dependence of the observed asymmetry ξ/PQ was fitted in bins over θ_π^{cm} to determine the spin-correlation

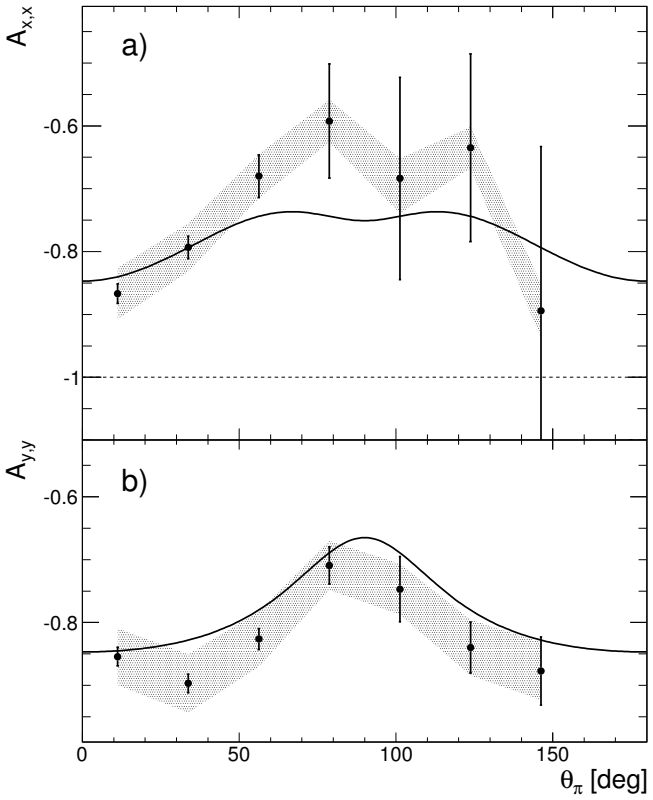

Figure 4.7: Spin-correlation coefficients (a) $A_{x,x}$ and (b) $A_{y,y}$ obtained for the reaction $\vec{n}\,\vec{p} \to d\pi^0$, depending on the pion emission angle θ_π in the center of mass system [14]. The points are shown with statistical errors. The values of the systematic errors are denoted by the shaded area. Previously published data [87] are not shown because of too large error bars. The results are compared with the SAID predictions [76] denoted by a solid line.

coefficients. The result is shown in Fig. 4.7 and is given in Table 4.9, both coefficients are well described by the SAID solutions [76]. The SAID data were averaged over the $T_{\rm free}$ range used with weights corresponding to the experimental $T_{\rm free}$ distribution. Let's note that the existing at 350 MeV data for the $A_{x,x}$ and $A_{y,y}$ of the $\vec{p}\vec{p} \to d\pi^+$ process [87] have error bars comparable with the signal value, and therefore not shown in Fig. 4.7, weakly refine the partial-wave analysis.

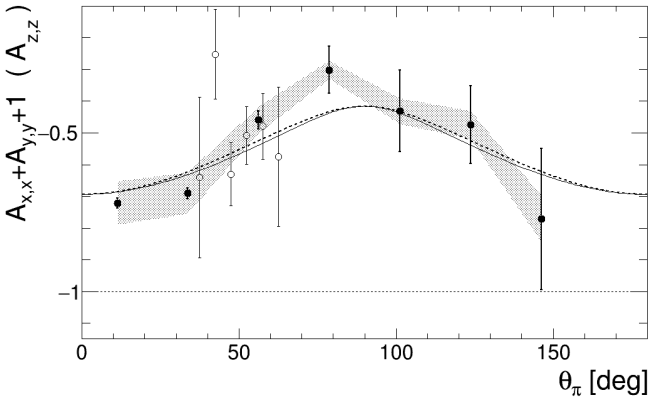

Figure 4.8: The combination $1 + A_{x,x} + A_{y,y}$, measured for the reaction $\vec{n}\,\vec{p} \to d\pi^0$, as a function of the pion emission angle θ_π [14], is compared with the SAID prediction for $pp \to d\pi^+$ (dashed line) [76]. Statistical uncertainties are shown with error bars. Systematic uncertainties are indicated by the shaded area. The open circles denote the data of the $A_{z,z}$ in the reaction $\vec{p}\vec{p} \to d\pi^+$ obtained in the IUCF experiment at 350 MeV [87]. The SAID prediction for the $A_{z,z}$ is shown by the solid line.

The longitudinal spin correlation $A_{z,z}$ of the reaction $\vec{p}\vec{p} \to d\pi^+$ at 350 MeV is more accurately determined [87], and this result is shown in Fig. 4.8 in comparison with the values obtained for the value $1+A_{x,x}+A_{y,y}$ of the reaction $\vec{n}\vec{p} \to d\pi^0$ at 353 MeV. These two quantities coincide exactly at $\theta_\pi = 0^o$ and 90^o. And if the pion d-wave is neglected, which should be a good approximation for such low energies, $A_{z,z} = 1+A_{x,x}+A_{y,y}$ over the full angular range. As can be seen, the result for $1 + A_{x,x} + A_{y,y}$ really agrees well with both the data [87] and the predictions of the SAID partial-wave analysis [76]. It can be noted that there are no signs of any isospin invariance breaking, although the accuracy of the data does not allow to consider this result as a significant verification of the symmetry.

Central value θ_π^{cm} in the bin, [grad]	Bin width, [grad]	$A_{x,x} \pm \text{stat} \pm \text{sys}$	$A_{y,y} \pm \text{stat} \pm \text{sys}$
11.25	22.5	$-0.87 \pm 0.02 \pm 0.04$	$-0.85 \pm 0.02 \pm 0.05$
33.75	22.5	$-0.79 \pm 0.02 \pm 0.04$	$-0.90 \pm 0.02 \pm 0.05$
56.25	22.5	$-0.68 \pm 0.03 \pm 0.04$	$-0.83 \pm 0.02 \pm 0.04$
78.75	22.5	$-0.59 \pm 0.09 \pm 0.03$	$-0.71 \pm 0.03 \pm 0.04$
101.25	22.5	$-0.68 \pm 0.16 \pm 0.06$	$-0.75 \pm 0.05 \pm 0.04$
123.75	22.5	$-0.63 \pm 0.15 \pm 0.03$	$-0.84 \pm 0.04 \pm 0.04$
146.25	22.5	$-0.89 \pm 0.26 \pm 0.04$	$-0.88 \pm 0.05 \pm 0.05$

Table 4.9: Spin correlation coefficients $A_{x,x}$ and $A_{y,y}$ values for the reaction $\vec{n}\,\vec{p} \to d\pi^0$ at 353 MeV with statistical and systematic errors [14].

Epilogue

The measurements of the differential cross section and spin observables for the reaction $pn \to \{pp\}_s\pi^-$ performed at the beam energy of 353 MeV and under the same kinematic conditions with data for the $pp \to \{pp\}_s\pi^0$ process [80] allow to determine with the discrete ambiguity both spin amplitudes of the isoscalar reaction channel $pn \to \{pp\}_s\pi^-$ and to carry out a partial-wave analysis of these amplitudes taking into account the contribution of the s-, p- and d-waves of the π meson. The practical and scientific significance of the result obtained is that the isolation of the transition amplitude ${}^3S_1 \to {}^1S_0p$, which contains the chiral LEC d, gives the necessary grounds for this parameter extracting from the obtained data. At the same time, the results of the analysis show that in order to eliminate the discrete ambiguity in the solutions obtained for the partial waves, it is necessary to measure the spin correlation coefficient $A_{x,z}$, which is the most sensitive to the form of solutions found. The proposal for the corresponding experiment was made on ANKE-COSY [65] and approved by the COSY program committee. Another use of the obtained results of partial wave analysis and elimination of its ambiguity will be the use of the detected amplitudes of the processes $pn \to \{pp\}_s\pi^-$ and $pp \to \{pp\}_s\pi^0$ to describe the data on the deuteron breakup $pd \to \{pp\}_sn$ at the same 350 MeV energy under kinematics of elastic backward pd scattering [88]. As shown in [89], the mechanism of the triangular diagram with the subprocess $pN \to \{pp\}_s\pi$ is the most likely mechanism of this process for the energy under consideration. The corresponding data on the deuteron breakup were obtained on ANKE-COSY and are currently in the analyzing stage. There is reason to expect that the description of the $pd \to \{pp\}_sn$ reaction data will allow us to choose

the most optimal of the three solutions found for the partial amplitudes of the process $pn \to \{pp\}_s\pi^-$.

From the theory point of view for the process under consideration, $pn \to \{pp\}_s\pi^-$, the procedure of extraction of the parameter d from the available data requires the implementation of complex theoretical calculations within χPT, which are currently carried out both at the level of modification of the NN-potential in the 5-th perturbation theory order [90], and of construction of the axial current operator in the 4-th order [91].

The methodological result of this work was the development of the procedures for the analysis of the data obtained with a target with a long storage cell in an experiment with a polarized beam and target. This technique was used in the analysis of a number of processes in measurements with double polarization on ANKE [92–94] and can be used in other experiments with a storage cell.

Outlook

The work is devoted to the measurement of the spin observables for the quasi-free reactions $pn \to \{pp\}_s\pi^-$ and $pn \to d\pi^0$near 353 MeV per nucleon. The experiment was carried out at the ANKE spectrometer (COSY-Jülich).

The main results of the thesis are:

1. The differential cross section $d\sigma/d\Omega$ and the proton analyzing power A_y^p for the process $\vec{p}n \to \{pp\}_s\pi^-$ at the proton beam energy $T_p = 353$ MeV over the whole angular interval and at the excitation energy of the diproton $E_{pp} < 3$ MeV were measured for the first time. The results obtained are basically consistent with the TRIUMF data at the same energy and $E_{pp} < 1.5$ MeV, available in a limited central interval of angles.

2. Using the time information from the vertex ANKE detector, the proton analyzing power A_y^p was obtained with a $E_{pp} < 1.5$ MeV cut, which allowed comparison with the TRIUMF results under the same conditions. The ANKE data in both cases are well matched, while the observed discrepancy with the TRIUMF data is preserved.

3. The process $\vec{n}\,\vec{p} \to \{pp\}_s\pi^-$ was investigated for the first time with the use of a vector-polarized deuteron beam and a polarized proton target. Polarimetry techniques, the background accounting and the vertex coordinate reconstructing when measured with a storage cell were developed for the double-polarized experiment.

4. The differential cross section $d\sigma/d\Omega$, the proton A_y^p and neutron A_y^n analyzing powers were determined for the process $\vec{n}\,\vec{p} \to \{pp\}_s\pi^-$ from the data with double

polarization. The results show good agreement with the differential cross section and the analyzing power A_y^p obtained in the single-polarized experiment, which indicates the correct consideration of systematic effects.

5. The first measurements of the spin correlation coefficients in $A_{x,x}$ and $A_{y,y}$ for the reaction $\vec{n}\,\vec{p} \to \{pp\}_s\pi^-$ at $T_n = 353$ MeV were carried out. The results agree with the theoretical expectation $A_{y,y} = 1$ in the full range of angles, while the value $A_{x,x}$ shows a deep minimum in the region of $\theta_\pi^{cm} = 60^o$.

6. The combination of all the obtained spin observables and cross section made it possible to carry out a joint partial-wave analysis for the processes $pp \to \{pp\}_s\,\pi^0$ and $pn \to \{pp\}_s\pi^-$ at 353 MeV. Three possible solutions to the analysis were found, equally satisfying the experimental data. It was shown that the best way to resolve ambiguity is to measure the mixed spin-correlation parameter $A_{x,z}$. The results of the analysis are necessary for the further determination of the contact $(NN)^2\pi$ interaction constant in χPT.

7. The spin correlation coefficients $A_{x,x}$ and $A_{y,y}$ were measured for the first time for the reaction $\vec{n}\,\vec{p} \to d\pi^0$. The results demonstrate a good agreement with the partial-wave SAID analysis for the reaction $\vec{p}\,\vec{p} \to d\pi^+$, as well as with the available data for $A_{z,z}$ for this reaction. There were no signs of isospin invariance violation.

Acknowledgments

In this short but important chapter, I would like to express my gratitude to all, without whom this work would not have become possible.

I would like to thank my research supervisor, Dr. S. Dymov for guidance, assistance and explanation of the principles and details of the ANKE data analysis and for his invaluable contribution to the preparation of the thesis. I would like to thank as well as scientific adviser, Dr. Yu. Usikov for theoretical discussions, advices and instructions, and help in preparing the work. I'm very grateful to the director of the IKP FZ-Jülich Institute, Prof. Dr. Hans Ströher, for giving me the opportunity to do this work. I would like to thank Dr. A. Kulikov for a huge number of valuable comments on the course of writing the work. I would like to express my gratitude to Prof. Dr. Colin Wilkin for the many discussions and explanations. I would like to thank Dr. A. Kacharava for his constant attention, support and advices during my work. Separately, I want to thank Dr. V. Baru, who took part in the preparation of the experiment, in the analysis and in the discussion of the results.

I'm very grateful to all the colleagues from the ANKE collaboration who helped me with advice and deed, and were always ready to give me friendly support!

Appendix A

Systematic errors of the normalization

A.1 Impact of the inaccuracy in the polarization determination

In order to verify the validity of use of the equal polarization values for states with polarization vectors directed up and down, both for the beam and for the target, one can investigate the polarization uncertainties influence on the result.

Let us write the beam polarization values for different polarization vector directions as follows: $P\uparrow = P - \delta p + \eta$, $P\downarrow = P + \delta p + \eta$, $Q\uparrow = Q - \delta q + \eta_q$, $Q\downarrow = Q + \delta q + \eta_q$, where P and Q are the averaged beam and target polarizations, respectively, $2\delta p$ and $2\delta q$ are the differences between the polarization values for opposite polarization vector directions, η is the deviation of the measured values of P and Q from the real ones. The polarization estimates obtained experimentally yield values of δp, δq and η within 5%.

Then, the ratio $\frac{\xi}{PQ}$, from the angular dependence of which the spin correlation coefficients are determined, can be written as

$$\frac{\xi}{PQ} = \frac{C(1 + \frac{\eta}{P} + \frac{\eta_q}{Q} + \frac{\eta\eta_q}{PQ})}{1 - A(\delta p + \delta q) + C\delta p\delta q}\,, \tag{A.1.1}$$

where $\xi = \frac{\Sigma_1 - \Sigma_2}{\Sigma_1 + \Sigma_2}$, Σ_1 и Σ_2 are rates with the same and opposite beam and target polarizations directions, respectively, $A = A_y \cdot \cos\phi$, $C = A_{x,x}\sin^2\phi + A_{y,y}\cos^2\phi$.

In this case, the variation of the ratio $\frac{\xi}{PQ}$ can be written as follows:

$$\delta\frac{\xi}{PQ} = \left(\left(\frac{(A-C\delta q)C(1+\frac{\eta}{P}+\frac{\eta_q}{Q}+\frac{\eta\eta_q}{PQ})}{(1-A(\delta p+\delta q)+C\delta p\delta q)^2}\delta p\right)^2 + \left(\frac{C(\frac{1}{Q}+\frac{\eta}{PQ})}{(1-A(\delta p+\delta q)+C\delta p\delta q)}\delta\eta\right)^2 + \left(\frac{(A-C\delta p)C(1+\frac{\eta}{P}+\frac{\eta_q}{Q}+\frac{\eta\eta_q}{PQ})}{(1-A(\delta p+\delta q)+C\delta p\delta q)^2}\delta q\right)^2 + \left(\frac{C(\frac{1}{P}+\frac{\eta_q}{PQ})}{(1-A(\delta p+\delta q)+C\delta p\delta q)}\delta\eta\right)^2\right)^{1/2} \tag{A.1.2}$$

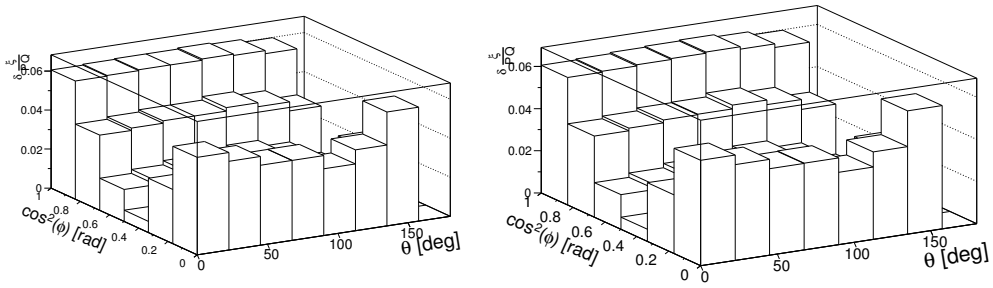

Figure A.1: The angular dependence of the $\delta\frac{\xi}{PQ}$ uncertainties for the polarization P and Q variation, on the left $\delta p = \delta q = 0\%$, on the right $\delta p = \delta q = 5\%$.

Fig. A.1 shows the obtained distribution of the deviations $\delta\frac{\xi}{PQ}$ with varying polarizations for different bins over $\cos^2\phi$ and θ. The main contribution to the systematic error in the polarization determination is made by the shift of average for the polarizations $P\uparrow$, $P\downarrow$. It is fixed with an accuracy of 4% by the definition of the polarization product PQ with use of the relation $A_{y,y} = 1$ for the process $pn \to \{pp\}_s\pi^-$. As can be seen from the comparison of two histograms in Fig. A.1, the difference between $P\uparrow$ and $P\downarrow$ is negligible and the value 0.01 is used as a conservative estimate.

A.2 Relative luminosity determination error

In order to evaluate the influence of inaccuracy in the luminosity determination, one can write the relative luminosity as follows:

$$R\uparrow\downarrow = \frac{L\uparrow\downarrow}{L} = 0.97 \pm 0.02\,, \tag{A.2.3}$$

$$R\downarrow\uparrow = \frac{L\downarrow\uparrow}{L} = 0.95 \pm 0.02 \tag{A.2.4}$$

$$R\downarrow\downarrow = \frac{L\downarrow\downarrow}{L} = 1.07 \pm 0.02\,, \tag{A.2.5}$$

where $L = L\uparrow\uparrow$.

Then the number of particles registered at different directions of the beam and target polarizations is expressed as follows:

$$N\uparrow\uparrow = L\cdot\sigma_0(1 + A\cdot(P+Q) + C\cdot PQ)\,, \tag{A.2.6}$$

$$N\uparrow\downarrow = R\uparrow\downarrow\, L\cdot\sigma_0(1 + A\cdot(P-Q) - C\cdot PQ)\,, \tag{A.2.7}$$

$$N\downarrow\uparrow = R\downarrow\uparrow\, L\cdot\sigma_0(1 - A\cdot(P-Q) - C\cdot PQ)\,, \tag{A.2.8}$$

$$N\downarrow\downarrow = R\downarrow\downarrow\, L\cdot\sigma_0(1 - A\cdot(P+Q) + C\cdot PQ)\,. \tag{A.2.9}$$

Having made the following designations: $D_1 = 1 - R\uparrow\downarrow - R\downarrow\uparrow + R\downarrow\downarrow$, $D_2 = 1 - R\uparrow\downarrow + R\downarrow\uparrow - R\downarrow\downarrow$, $D_3 = 1 + R\uparrow\downarrow - R\downarrow\uparrow - R\downarrow\downarrow$, $D_4 = 1 + R\uparrow\downarrow + R\downarrow\uparrow + R\downarrow\downarrow$, one can obtain an expression for the ratio $\frac{\xi}{PQ}$ as an angular function:

$$\frac{\xi}{PQ} = \frac{\frac{D_1}{PQ} + \frac{D_2\cdot A}{Q} + \frac{D_3\cdot A}{P} + D_4\cdot C}{D_4 + D_3\cdot AP + D_2\cdot AQ + D_1\cdot CPQ}\,. \tag{A.2.10}$$

After that, by varying the relative luminosities

$$\frac{\partial\xi/PQ}{\partial\delta R\uparrow\downarrow} = \frac{PQ\Big((-\frac{1}{PQ} - \frac{A}{Q} - \frac{A}{P} + C)(D_4 + \frac{AD_3}{Q} + \frac{AD_2}{P} + CD_1\Big)}{(D_4 + APD_3 + AQD_2 + CPQD_1)^2} - \frac{\Big(\frac{D_1}{PQ} + \frac{AD_2}{Q} + \frac{AD_3}{P} + CD_4)(\frac{1}{PQ} + \frac{A}{Q} - \frac{A}{P} - C)\Big)}{(D_4 + APD_3 + AQD_2 + CPQD_1)^2}\,,$$

$$\frac{\partial\xi/PQ}{\partial\delta R\downarrow\uparrow} = \frac{PQ\Big((-\frac{1}{PQ} + \frac{A}{Q} - \frac{A}{P} + C)(D_4 + \frac{AD_3}{Q} + \frac{AD_2}{P} + CD_1\Big)}{(D_4 + APD_3 + AQD_2 + CPQD_1)^2} - \frac{\Big(\frac{D_1}{PQ} + \frac{AD_2}{Q} + \frac{AD_3}{P} + CD_4)(\frac{1}{PQ} - \frac{A}{Q} + \frac{A}{P} - C)\Big)}{(D_4 + APD_3 + AQD_2 + CPQD_1)^2}\,,$$

$$\frac{\partial \xi/PQ}{\partial \delta R \downarrow\downarrow} = \frac{PQ\Big((\frac{1}{PQ} - \frac{A}{Q} - \frac{A}{P} + C)(D_4 + \frac{AD_3}{Q} + \frac{AD_2}{P} + CD_1\Big)}{(D_4 + APD_3 + AQD_2 + CPQD_1)^2} - \frac{\Big(\frac{D_1}{PQ} + \frac{AD_2}{Q} + \frac{AD_3}{P} + CD_4)(\frac{1}{PQ} - \frac{A}{Q} - \frac{A}{P} + C)\Big)}{(D_4 + APD_3 + AQD_2 + CPQD_1)^2},$$

one obtains the required expression for the variations of the $\delta\frac{\xi}{PQ}$ determination under the experimental uncertainty for the relative luminosities:

$$\delta\frac{\xi}{PQ} = \sqrt{\Big(\frac{\partial \xi/PQ}{\partial \delta R \uparrow\downarrow}\Big)^2 (\delta R \uparrow\downarrow)^2 + \Big(\frac{\partial \xi/PQ}{\partial \delta R \downarrow\uparrow}\Big)^2 (\delta R \downarrow\uparrow)^2 + \Big(\frac{\partial \xi/PQ}{\partial \delta R \downarrow\downarrow}\Big)^2 (\delta R \downarrow\downarrow)^2}.$$

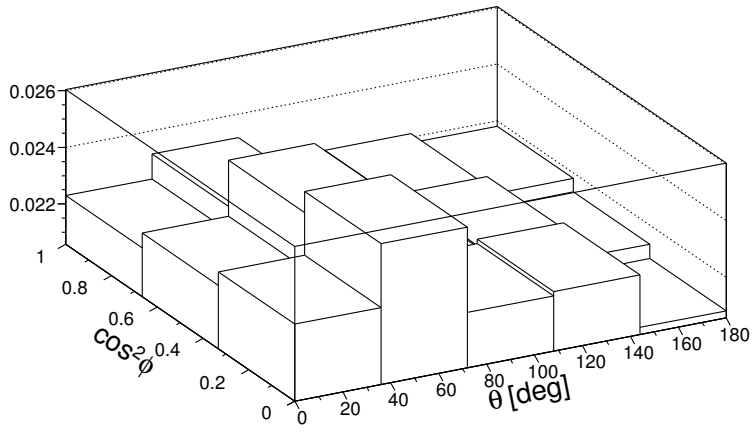

Figure A.2: Uncertainty $\delta\frac{\xi}{PQ}$ for the varying relative luminosities, depending on the bin over $\cos^2\phi$ and θ.

Fig. A.2 shows the obtained distribution of the deviations $\delta\frac{\xi}{PQ}$ with the varying relative luminosities for different bins over $\cos^2\phi$ and θ. The systematic error averaged over the angels is 0.023.

Appendix B

Kinematic variables determination

B.1 Kinematics of quasi-free collision

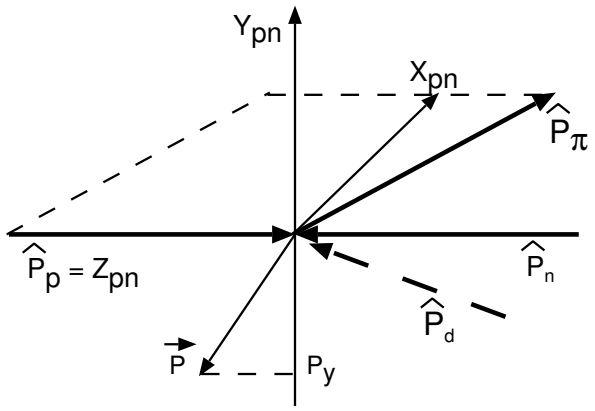

Figure B.1: Kinematics of quasi-free *pn* interaction.

When studying the quasi-free processes in *pd* collisions, the initial state of the *pn* system is defined as $(\breve{pn}) = \breve{p} + \breve{d} - \breve{p}_{\mathrm{spec}}$, where the upper symbol of $\breve{}$ means 4-vector, and p_{spec} is the spectator proton in the deuteron, affecting only the kinematics of the process. In the measurements described in this work it was agreed to count the scattering angle with respect to the momentum of the initial free proton P_p, regardless of whether a proton beam or target was used. The spectator's momentum was known either from direct measurement, or as missing 4-momentum of the reaction.

The kinematics of the $pd \to X\pi + p_{\rm spec}$ reaction in the (pn) rest frame is illustrated in Fig. B.1, where the hat symbols $\hat{P}_\pi, \hat{P}_p$, etc. the 3-momenta of particles in the (pn) rest frame are marked. In this system the Z-axis is determined by the initial proton, the Y-axis is the unit vector $\hat{P}_p \times \hat{P}_\pi$, and the X-axis forms the right-hand coordinate system with them. Note that the Z-axis here does not coincide with the beam direction in the laboratory system.

The beam or target polarization vector $\vec{P}$ in Fig. B.1, which is directed vertically in the described experiments, also does not lie in the $(X,Y)_{\rm pn}$ plane, which leads to the appearance of a small component P_z. This effect was taken into account in the systematic measurement errors evaluation.

In order to compare the results with the available data on free pn and pp scattering, the energy in the (pn) system was expressed as "free" energy $T_{\rm free}$ of the beam, obtained in free collision at the same s value:

$$T_{\rm free} = [s - (m_p + m_n)^2]/2m_p,$$

where $\sqrt{s}$ is the total energy in the (np) center of mass system, and m_p and m_n are the proton and neutron masses.

B.2 Process $pN \to \{pp\}_s\,\pi$ variables

Knowing the particle masses and 3-momenta in the initial state, the kinematics of the process event is determined by the 9 components of the 3-momenta of the final particles. Taking into account the four laws of energy and momentum conservation reduces the number of independent variables to 5. The $pN \to \{pp\}_s\,\pi$ can be considered as a reaction with two particles in the final state, considering the subsystem $\{pp\}_s$ as one particle. Then, the setting the process kinematics is divided into the description of the reaction $2 \to 2$ in the center of mass system and variables of the $\{pp\}_s$ system.

In this paper, the following set of kinematic variables is used: $(\theta_\pi^{cm}, \phi_\pi, \theta_k, \phi_k, E_{pp})$. Here θ_π^{cm} and ϕ_π are the polar and azimuthal angles of π^- in the center of mass system (see Figure B.2a). The polar and azimuth angles of the diproton are defined as $\theta_{pp}^{cm} = 180^o - \theta_\pi^{cm}$ and $\phi_{pp} = \phi_\pi + 180^o$, respectively.

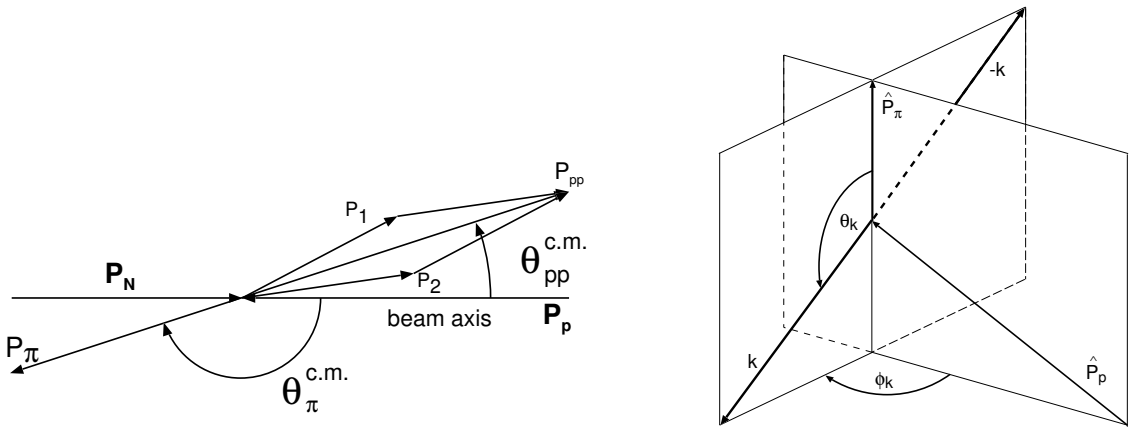

(a) Variables in the pN center of mass system.

(b) Variables in the diproton center of mass system.

Figure B.2: Reaction $pN \to \{pp\}_s X$ kinematics.

The polar and azimuth angles θ_k and ϕ_k in the rest frame of the proton pair are defined in Fig. B.2b. In this case, θ_k is reckoned from the P_π direction in the center of mass system of the reaction, and ϕ_k is measured from the plane formed by the beam particle P_p and the pion momentum P_π in the center of mass system.

The diproton excitation energy, equal to the kinetic energy in the rest frame of the proton pair, is defined as $E_{pp} = 2(m_p^2 + k^2)^{1/2} - 2m_p$, where k is the proton momentum in the diproton center of mass system, and m_p is the proton mass.

Bibliography

1. R. Machleidt, K. Holinde, Ch. Elster, Phys. Rep. 149, 1 (1987).
2. Machleidt, R., Adv. Nucl. Phys. 19, 189 (1989).
3. Stoks, V.G.J. et al. Phys. Rev. C 49, 2950 (1994).
4. R. Machleidt, Phys. Rev. C 63, 024001-1 (2001).
5. F. Gross, A. Stadler, Phys. Rev. C 78, 014005-1 (2008).
6. S. Weinberg, Physica A 96, 327 (1979).
7. S. Weinberg, Phys. Lett. B 251, 288 (1990).
8. S. Weinberg, Nucl. Phys. B 363, 3 (1991).
9. H. Hahn et al., Phys. Rev. Lett. 82, 2258 (1999).
10. F. Duncan et al., Phys. Rev. Lett. 80, 4390 (1998).
11. M. Daum et al., Eur. Phys. J. C. 25, 55 (2002).
12. S. Dymov et al., Phys. Lett. B 712, 375 (2012).
13. S. Dymov, V. Shmakova et al., Phys. Rev. C 88, 014001 (2013).
14. V. Shmakova et al., Phys. Let. B 726, 4–5, 549 (2013).
15. V. Shmakova, EPJ Web of Conferences 37, 01020 (2012).
16. V. Shmakova, Physics of Elementary Particles and Atomic Nuclei 45, 117 (2014).

17. Yu.N. Uzikov. Three nucleon forces and some aspects of nuclear astrophysics - In: Book "The Universe Evolution, nuclear astrophysics", Nova Science Publisher, Inc., New York, Eds. Igor Strokovsky and Leonid Blokhintsev, ISBN: 978-1-62808-547-7, 269 (2013).

18. B.L. Ioffe, V.S. Fadin, L.N. Lipatov, Quantum Chromodynamics. Perturbative and Nonperturbative Aspects. CUP, NY (2010).

19. J. Goldstone, Nuovo Cimento 19, 154 (1961).

20. Y. Nambu, Phys. Rev. Lett.4, 380 (1960).

21. A.I. Vainshtein, V.I. Zakharov, UFN 100 225 (1970).

22. R. Machleidt and D. R. Entem, Phys. Rept. 503, 1 (2011).

23. P. Boucaud, et al., Phys. Lett. B, vol. 650, 304 (2007), S.R. Beane, et al. Phys. Rev. Lett. 97, 012001-1 (2006).

24. E. Epelbaum, Ulf-G. Meissner, Annu. Rev. Nucl. Part. Sci. 62, 159 (2012).

25. J.-I. Fujita, H Miyazawa, Prog. Theor. Phys. 17, 360 (1957).

26. G. Witala, et al., Phys. Rev. Lett. 81, 1183 (1998).

27. W.N. Polyzou, W. Glöckle, Few-Body Syst. 9, 97 (1990).

28. M.L. Goldberger, S.B. Treiman, Phys. Rev. 110, 1178 (1958).

29. V. Baru, C. Hanhart, F. Myhrer, International Journal of Modern Physics E 23, No. 4, 1430004 (2014).

30. A. Gardestig, D.R. Phillips, Phys. Rev. Lett. 96, 232301-1 (2006).

31. C. Hanhart, U. van Kolck, and G. A. Miller, Phys. Rev. Lett. 85, 2905 (2000).

32. E. Epelbaum, et al., Phys. Rev. C 66, 064001-1 (2002).

33. A. Nogga, Phys. Rev. C 73, 064002-1 (2006).

34. P. Navratil, Phys. Rev. Lett. 99, 042501-1 (2007).

35. T.-S. Park, et al., Phys. Rev. C 67, 055206-1 (2003).

36. D. Gazit, S. Quaglioni, P. Navratil, Phys. Rev. Lett. 103, 102502-1 (2009).

37. L.E. Marcucci, Phys. Rev. Lett. 108, 052502-1 (2012).

38. R.D. Entem, R.M. Machleidt, Phys. Rev. C 68, 0441001(R)-1 (2003).

39. A. Gardestig, D.R. Phillips, Phys. Rev. C 73, 014002-1 (2006).

40. E. Adelberger, et al., Rev. Mod. Phys. 83, 195 (2011).

41. H. A. Bethe, C.L. Critchfield, Phys. Rev. 54, 248 (1938).

42. E.E. Salpeter, Phys. Rev. 88, 547 (1952).

43. J.N. Bahcall, R.M. May Astrophys. J. 155, 501 (1969). M. Kamionkowski, J.N. Bahcall, Astrophys. J.420, 884 (1994).

44. R. Schiavilla, et al. Phys. Rev. C 58, 1263 (1998).

45. L.E. Marcucci, R. Schiavilla, M. Viviani, arXiv:1303.3124 [nucl-th].

46. C.R. Howell, et al. Phys. Lett. B 444, 252 (1998).

47. W.R. Gibbs, B.F. Gibbson, G.J. Stephenson Jr., Phys. Rev. C 11, 90 (1975); 1977, 16, 327 (1977).

48. J. Adam, Jr., Phys. Lett. B 709, 93 (2012).

49. V.A. Andreev, et al (MuSun Collabortaion) (2008), available from http://www.npl.uiuc.edu/exp/musun.

50. X.Luo, EPJ Web Conf. 95 04037, (2015).

51. A. Kacharava, F. Rathmann, and C. Wilkin, Spin Physics from COSY to FAIR, COSY proposal 152 (2005), arXiv:nucl-ex/0511028.

52. S.X. Nakamura, Phys. Rev. C 77, 054001-1 (2008).

53. V. Baru et al., Phys. Rev. C 80, 044003 (2009).

54. J. Haidenbauer, K. Holinde, and M. B. Johnson, Phys. Rev. C 48, 2190 (1993).

55. O. Imambekov, Yu.N. Uzikov, Yad. Fiz. 52, 1361 (1990).

56. V.I. Komarov et al., Phys. Lett. B 553, 179 (2003).

57. S. Dymov et al., Phys. Rev. C 81, 014001, (2010).

58. D. Chiladze, et al. Eur. Phys. J. A 40, 23 (2009).

59. S. Dymov et al., Phys. Lett. B 635, 270 (2006).

60. S. Dymov, et al. Phys. Rev. Lett. 102, 192301-1 (2009).

61. V. Komarov, et al. Phys. Rev. Lett. 101, 102501-1 (2008).

62. D. Hüber, Few-Body Syst. 30, 95 (2001).

63. R. Bilger et al., Nucl. Phys. A 663 633 (2001).

64. A. Abdel-Bary et al., Eur. Phys. J. A 36, 7 (2008)

65. S. Dymov and A. Kacharava, COSY proposal 213 (2013). `http://collaborations.fz-juelich.de/ikp/anke/proposal/COSY_Proposal_213.pdf`

66. S. Barsov et al., Nuclear Instruments and Methods A, 462, 364 (2001).

67. R. Maier, et al., Nuclear Instruments and Methods A, 390, 1 (1997).

68. R. Weidmann et al., Rev. of Scientific Instruments, 67, 1357, (1996).

69. O. Felden et al. Proc. 9th Int. Workshop on Polarized Sources and Targets, Nashville, 2001, eds. V.P. Derenchuk and B. von Przewoski, Nashville, USA, p.200 (2001), (World Scientific, Singapore, 2002).

70. A. Khoukaz et al., European Physical Journal D 5, 275, (1999).

71. M. Mikirtychyants et al., Nuclear Instruments and Methods A, 721, 83 (2013).

72. B. Chiladze et al., Part. and Nuclei Letters No.4 113, 95 (2002).

73. S. Dymov, et al., Part. and Nuclei Letters No.2 119, 40 (2004).

74. S.N. Dymov et al., Trigger electronics for the forward and backward hodoscopes of ANKE, E10-2002-19, Communication of the JINR. Dubna (2002).

75. P. Fedorets et al., Efficiency of the second scintillator plane of the ANKE forward detector, IKP FZ-Jülich Annual report (2001).

76. R. A. Arndt, I. I. Strakovsky, R. L. Workman, D. V. Bugg, Phys. Rev. C 48,1926 (1993); http://gwdac.phys.gwu.edu.

77. I. Fröhlich et al., Proc. XI Int. Workshop Advanced Computing and Analysis Techniques in Physics Research, PoS(ACAT) 076 (2007); arXiv:0708.2382 [nucl-ex].

78. Gerald G. Ohlsen, Rep. Prog. Phys. 35, 717 (1972).

79. C. Hanhart, Phys. Rept. 397, 155 (2004).

80. D. Tsirkov et al., Phys. Lett. B 712, 370 (2012).

81. K. M. Watson, Phys. Rev. 88, 1163 (1952); A. B. Migdal, Sov. Phys. JETP 1, 2 (1955).

82. R. A. Arndt, I. I. Strakovsky, and R. L. Workman, Phys. Rev. C 62, 034005 (2000).

83. V. Baru, E. Epelbaum, J. Haidenbauer, C. Hanhart, and V. Lensky (unpublished).

84. H. Hahn et al., Phys. Rev. C, 53, 1074 (1996).

85. D. A. Hutcheon, et. al., Phys. Rev. Lett. 64, 176 (1990).

86. A. K. Opper, et. al., Phys. Rev. Lett. 91, 212302 (2003).

87. B. v. Przewoski, et al., Phys. Rev. C 61, 064604 (2000).

88. Yu.N. Uzikov, ANKE Collaboration Annual Reports (2015); http://collaborations.fz-juelich.de/ikp/anke/annual/Annual_Report_15.shtml

89. Yu.N. Uzikov, J.Haidenbauer, C. Wilkin, Phys. Rev. C 77, 014008 (2007).

90. E.Epelbaum, H.Krebs, U.-G. Meissner, PRL 115, 122301 (2015).

91. H.Krebs,E.Epelbaum, U.-G. Meissner, arxiv:1610.03569 [nucl-th].

92. S.Dymov et al., Phys. Lett. B 744, 391 (2015).

93. S. Dymov et al., Phys. Lett. B 762, 102 (2016).

94. B. Gou et al., Phys. Lett. B 741, 305 (2015).